

Todo list

check patent citation	18
redraw	22
read reference	23
was that first, get	24
redraw	30
modified ?	30
read more of this	30
slightly ?	31
ref	34
get this right: should be $\sqrt{2}$	50
wrong	110

¹ **Abstract**

² Photobleaching and phototoxicity pose a problem in live cell imaging. Fluorescence imaging induces reactive oxygen species in observed organisms which
³ can alter the behaviour of the sample, and so minimising light exposure is an
⁴ important goal.

⁶ We augment a widefield epifluorescence microscope with two spatial light
⁷ modulators. By controlling the spatial illumination pattern and the angle at
⁸ which illumination occurs, we achieve control of the illumination pattern in
⁹ three dimensions.

¹⁰ Our custom software is used to obtain an initial image stack of the specimen.
¹¹ Subsequent image sections are exposed with excitation patterns that take
¹² into account the previous image stack. Depending on the distribution of
¹³ fluorophores this adaptive exposure can considerably reduce photobleaching
¹⁴ and phototoxicity.

Contents

15	1. Introduction	8
16	1.1. Fundamentals of fluorescence	9
17	1.1.1. Photobleaching and phototoxicity	13
18	1.2. Conventional microscopes	14
19	1.2.1. Widefield epifluorescence microscope	16
20	1.2.2. Confocal microscope	17
21	1.2.3. Phototoxicity in conventional microscopes	18
22	1.2.4. Two photon laser scanning fluorescence microscopy	18
23	1.3. Image detectors in widefield microscopy	18
24		
25	2. Other approaches of light control	20
26	2.1. Light sheet fluorescence microscopy	20
27	2.1.1. Light sheet generation with cylindrical lens	20
28	2.1.2. Light sheet generation using the detection objective	22
29	2.2. Scanning techniques for improving light utilization	23
30	2.2.1. Controlled light exposure microscopy (CLEM)	23
31	2.2.2. Acousto-optic deflectors for fast beam steering	24
32	2.3. Non-scanning	25
33	2.3.1. Direct illumination	25
34	2.3.2. Intensity modulation	26
35	2.3.3. Temporal focusing	29
36	2.3.4. Phase modulation	29
37		
37	3. A prototype for spatio-angular illumination	32
38	3.1. Overview	32
39	3.2. Detailed explanation of the optical components	34
40	3.3. Electronics for synchronization	37
41	3.4. Alignment of the displays	39
42	3.5. Ray-based illumination optimization	40
43	3.5.1. Index matched sphere model	40

44	3.5.2. Tracing in illumination direction	41
45	3.5.3. Tracing in detection direction	42
46	3.5.4. Coping with index mismatch of the embedding medium	43
47	4. Description of experiments	46
48	4.1. Measure acceptance angle	46
49	4.2. Spatio-angular illumination of beads	46
50	A. Read noise characterization of cameras	48
51	A.1. Introduction	48
52	A.2. Calibration of an Andor IXon3 camera	49
53	A.2.1. Andor Basic code listing for automatic image acquisition	50
54	A.2.2. Python code listing for the read noise evaluation	53
55	A.3. Comparison with other cameras	56
56	B. Raytracing for spatio-angular microscopy	57
57	B.1. Refraction at plane surface	57
58	B.2. Intersection of a ray and a plane	59
59	B.3. Intersection of a ray and a sphere	60
60	B.3.1. Solving the quadratic equation	60
61	B.4. Refraction on paraxial thin lens	60
62	B.5. Refraction through oil objective (illumination)	61
63	B.6. Reverse path through oil objective (detection)	63
64	B.6.1. Easy case: back focal plane positions only	63
65	B.6.2. Full raytrace	63
66	B.6.3. Treatment of aberration (detection)	65
67	B.7. Sphere projection	65
68	C. Transforming camera coordinates into LCoS coordinates	68
69	D. Implementation of a robust structured illumination reconstruction technique	75
70	D.1. Simulated image acquisition	75
71	D.2. Fundamentals of structured illumination	78
72	D.2.1. Apotome	78
73	D.2.2. HiLo	79
74	D.3. Alternative method (subtraction method)	84
75	E. Wave optical simulation of the spatio-angular microscope	89

76	F. MEMI optical system	93
77	G. Experiments with DVI LCoS	95
78	G.1. Description of the setup (fast MMA)	95
79	G.1.1. On using OGP1 as graphics hardware	96
80	G.2. Description of the trigger generation (slow MMA)	97
81	G.3. Verification of the synchronization	100
82	G.4. Conclusion	102
83	H. Shearing interferometer-based intensity modulation with a MEMS mirror device	104
84	H.1. Introduction	104
85	H.2. Description of the setup	105
86	H.3. Displaying arbitrary gray values using the DIC approach	106
87	H.4. Experimental results	112
88	H.4.1. Procedure to measure the split angle of a Nomarski prism .	112
89	H.4.2. Imaging the MMA with the DIC method	113
90	H.4.3. Effects of limited crystal size on DIC image	116
91	H.5. Discussion	118
92	I. Holographic approach to spatio-angular illumination	121
93	I.1. Introduction	121
94	I.2. Description of the holographic method	121
95	I.2.1. Description of the experimental setup	122
96	I.2.2. Description of the sample	122
97	I.3. Characterization of the phase-only spatial light modulator	122
98	I.3.1. Numerical simulation	124
99	I.3.2. Measurement	125
100	I.4. Conclusion	126
101	J. Equidistant spiral sampling	127
102	J.1. Archimedes Spiral	127
103	J.2. Equidistance sampling	127
104	J.3. Filling the back focal plane	128
105	J.4. Improvement for sampling with disks	129
106	J.5. Discussion	130

Nomenclature

¹⁰⁷

- ¹⁰⁸ ADU analog-to-digital unit
- ¹⁰⁹ AOD Acousto-optic deflector
- ¹¹⁰ AOM Acousto-optic modulator
- ¹¹¹ BFP Back focal plane
- ¹¹² CCD charge-coupled devices
- ¹¹³ CLEM Controlled light exposure microscopy
- ¹¹⁴ DIC differential interference contrast
- ¹¹⁵ DMD Digital micro mirror device
- ¹¹⁶ DPSS Diode-pumped solid-state (laser)
- ¹¹⁷ EGFP Enhanced green fluorescent protein
- ¹¹⁸ EM-CCD Electron multiplying charge-coupled devices (p. 18, 48)
- ¹¹⁹ GFP Green fluorescent protein
- ¹²⁰ HILO Highly inclined and laminated optical sheet microscopy
- ¹²¹ IFTA Iterative Fourier transform algorithm
- ¹²² LCoS Liquid crystal on silicon (display)
- ¹²³ LED Light-emitting diode
- ¹²⁴ MEMI Micro-mirror enhanced micro-imaging. EU FP7 project reference 215597.
- ¹²⁵ MLE-PAM Minimized light exposure programmable array microscope
- ¹²⁶ MMA micro-mirror array
- ¹²⁷ NA numerical aperture

Contents

- ¹²⁸ OPM Oblique plane microscopy
- ¹²⁹ OTF optical transfer function
- ¹³⁰ PAM Programmable array microscopy
- ¹³¹ PCF Phase contrast filter
- ¹³² PSF point spread function
- ¹³³ SPIM Selective plane illumination microscopy
- ¹³⁴ VCSEL Vertical-cavity surface-emitting laser
- ¹³⁵ YFP Yellow fluorescent protein

¹³⁶ 1. Introduction

¹³⁷ Fluorescence microscopy is an old technique that has been established in live sciences
¹³⁸ for a long time. Being able to see things happening at the micrometre scale is the
¹³⁹ fundamental path to understand life and disease.

¹⁴⁰ Innovation continuously improves microscopy and occasionally new fields of re-
¹⁴¹ search are opened up: The discovery and development of fluorescent proteins initi-
¹⁴² ated a revolution in how microscopy can be applied in living specimen. Optical high
¹⁴³ resolution techniques allow to observe biological processes at the scale of individual
¹⁴⁴ molecules (tens of nm).

¹⁴⁵ Labels that report membrane potentials or viscosity within cells, compounds that
¹⁴⁶ locally release (uncage) chemicals when illuminated by light or even ion pumps that
¹⁴⁷ can be switched by light promise novel interesting research.

¹⁴⁸ All these techniques have in common, that excitation light has to reach a fo-
¹⁴⁹ cal point, line or plane within the sample which consists of a more or less dense
¹⁵⁰ fluorophore distribution.

¹⁵¹ With few exceptions (2 photon, SPIM, CLEM) microscopes are generally not too
¹⁵² intelligent about what other fluorophores are excited, apart from the ones in focus.

¹⁵³ Here we build a spatio-angular microscope. It contains two programmable masks
¹⁵⁴ and can control which parts of the sample (spatial) are illuminated by what angles.
¹⁵⁵ Its applications will mostly cover imaging of living organisms experiments in them.
¹⁵⁶ There the effects of phototoxicity are strongest and our microscope has an advantage
¹⁵⁷ over conventional techniques.

158 1.1. Fundamentals of fluorescence

159 Here we give a short overview of the field of fluorescence of molecules in order
 160 to introduce the terms Stokes shift, triplet state and photobleaching.

161 First we consider a really simple molecule: We move the nuclei of two hydrogen
 162 atoms and move them slowly together. When the nuclei have a big distance, the
 163 atoms exist as two separate entities without influence on each other. In the other
 164 extreme case the two nuclei are at the same position and the electrons have the
 165 orbitals of a helium atom.

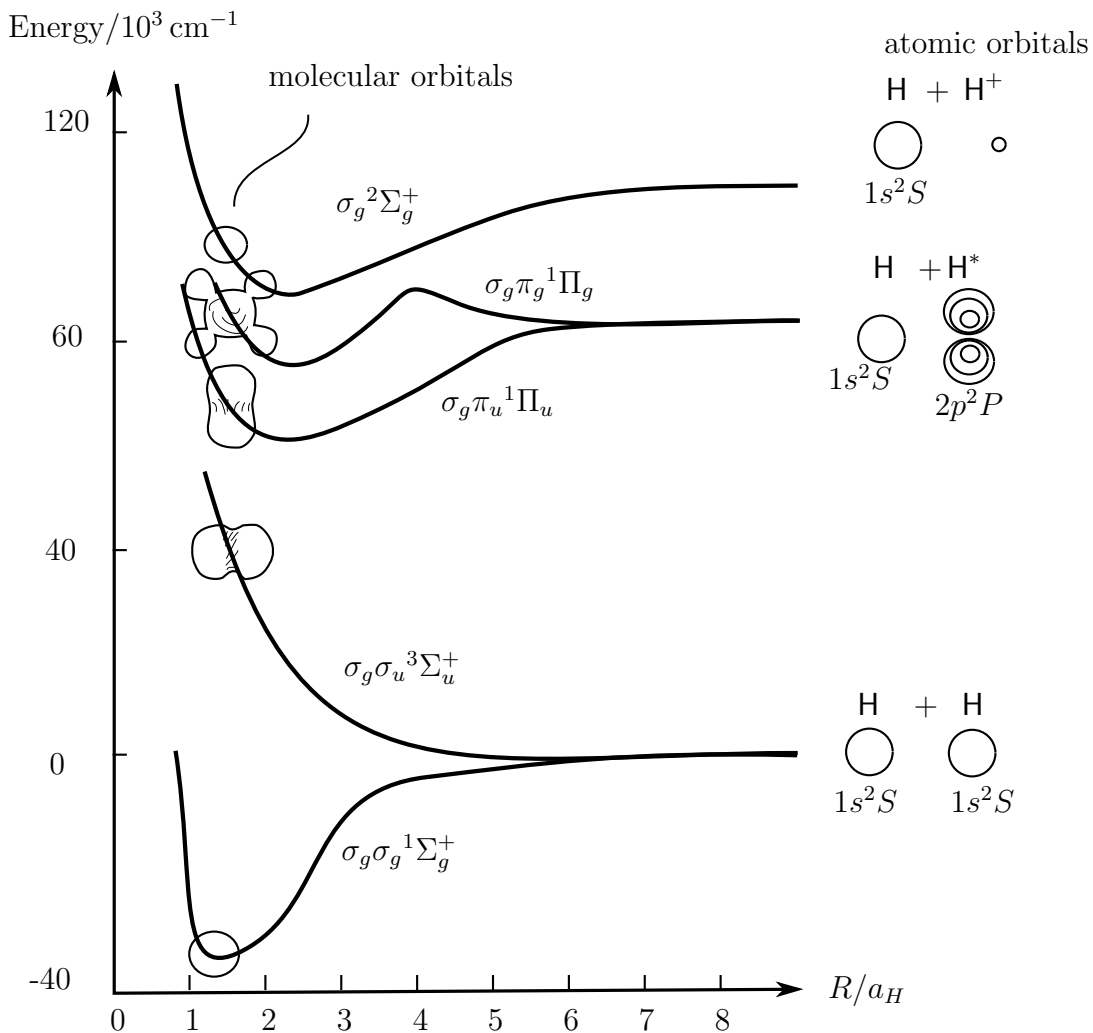


Figure 1.1.: Schematic electron density maps and potential curves for ground state H_2 and excited state H_2^* of dihydrogen and the dihydrogen ion H_2^+ (after Haken and Wolf (2006) p. 258).

`fig:flu-potential_my`

166 As a good approximation we can express molecular orbitals as a linear combi-
 167 nation of atomic orbitals and calculate their potential energy in dependence of the

1. Introduction

168 distance between the nuclei (see Figure 1.1). The curve for $\sigma_g\sigma_g^1\Sigma_g^+$ has minimum
169 at a core distance R of approximately 1.3 Bohr radii ($a_H = 0.529 \cdot 10^{-8}$ cm). The
170 compound of two protons and two electrons is particularly stable for this radius.
171 We call it the hydrogen molecule H_2 .

172 In the same way we can combine a ground state hydrogen atom H and an excited
173 hydrogen atom H^* . Again the potential $\sigma_g\pi_u^1\Pi_u$ has a minimum. That distance
174 of equilibrium is bigger because the strength of the chemical bond in the excited
175 hydrogen molecule is decreased.

176 The distance between the two nuclei is not rigid. The nuclei can oscillate around
177 their position of equilibrium at quantized frequencies. These vibration frequencies
178 depend on the strength of the bond which in turn depends on the excitation state
179 of the molecule. Figure 1.2 shows potential curves for the ground state and the
180 first excited state of two different molecules. The left graph shows potential curves
181 of a (theoretical) molecule where the strength of the bond doesn't change in the
182 excited state. There, the minima of both curves are exactly on top of each other.
183 If a ground state molecule absorbs a photon its electron would be excited but the
184 vibrational state of the core does not change.

185 The right graph displays the more realistic case of a molecule with a weaker
186 chemical bond in the excited state. When a photon is absorbed, the electronic state
187 of the molecule switches essentially instantaneous compared to the movement of
188 the nuclei. After the electronic transition the nuclei will start moving because their
189 equilibrium position changed. In the diagram the absorption event can be depicted
190 as a vertical line. The same rule applies for emission.

191 It is useful to summarize information about the energy levels of a molecule in a
192 Jablonski diagram as in Figure 1.3. If a molecule is in the ground state S_0 one of its
193 outer electron(s) can be excited by a photon to either the first excited singlet state
194 S_1 or, if the photon has an even higher energy, the electron will go into the second
195 excited state S_2 . The absorption of one photon can not put the electron into the
196 triplet state T_1 as angular momentum must be conserved.

197 The electronic absorption event is very rapid (in femtoseconds). Due to the
198 Franck-Condon principle the electronic excitation also excites vibrational and rota-
199 tional modes of the molecule. When the fluorescent molecule is immersed in a liquid
200 this vibro-rotational excitation will be transferred to neighbouring molecules in a
201 matter of picoseconds. This process is called *internal conversion*. The interaction of
202 the molecule with its surroundings is completely statistical and the excited electron
203 will loose its phase relationship with electrons of other fluorescent molecules. A S_2
204 electron will decay radiationless into S_1 due to internal conversion.

On construction of term symbols

The symmetric linear combination of the $1s$ -orbitals of two atoms A and B is

$$\sigma_g 1s = \frac{1}{\sqrt{2}}(\sigma 1s_A + \sigma 1s_B).$$

σ_u is constructed as the difference of the two atomic orbitals. In general the symmetric molecular orbital σ_g is more stable as the electrons have a higher probability to be between the nuclei. The following quantum numbers describe the molecular wave function:

Λ .. Defined by $\mathbf{L}_z = \Lambda \hbar = |\sum \lambda_i | \hbar$ with projection λ_i of the orbital angular momentum \mathbf{l}_i of electron i onto the nuclear axis. Λ can take the values $0, 1, 2, \dots$ and one writes the term symbols $\Sigma, \Pi, \Delta, \dots$

S .. Spin of all electrons $S = \sum \mathbf{m}_{si}$ in the molecular orbital.

Ω .. Electronic angular momentum in direction of the nuclear axis.

These numbers are combined into the term symbol like this: $^{2S+1}\Lambda_\Omega$. Additionally one writes e.g. Σ^+ if the molecular function is symmetric when mirrored at a plane through the nuclei. Furthermore one writes Σ_g if the sign of wave function stays the same when the molecule is inverted at the point of symmetry. Here is an example of the molecular wave functions we are interested in:

$$\begin{aligned} \sigma_g \sigma_g^1 \Sigma_g^+ &: \lambda_1 = 1, \lambda_2 = -1, s_1 = +, s_2 = - \\ \Lambda &= |\lambda_1 + \lambda_2| = |1 - 1| = 0, S = s_1 + s_2 = 0 \\ \sigma_g \pi_u^1 \Pi_u &: \lambda_1 = 1, \lambda_2 = -2, s_1 = +, s_2 = - \\ \Lambda &= |1 - 2| = 1, S = 0 \end{aligned}$$

205 A S_1 electron can relax into the ground state S_0 by emitting a photon. For this
 206 transition the Frank-Condon principle applies again. A vibro-rotational mode of
 207 the ground state will be excited. Due to internal conversion at two steps during
 208 the whole process the energy of the emitted fluorescence photon is lower than the
 209 energy of the excitation photon (Stokes shift). The fluorescence lifetime – the time
 210 the molecule stays in state S_1 – is in the range of nanoseconds.

211 There is a small probability that the electron doesn't relax and instead flips its

1. Introduction

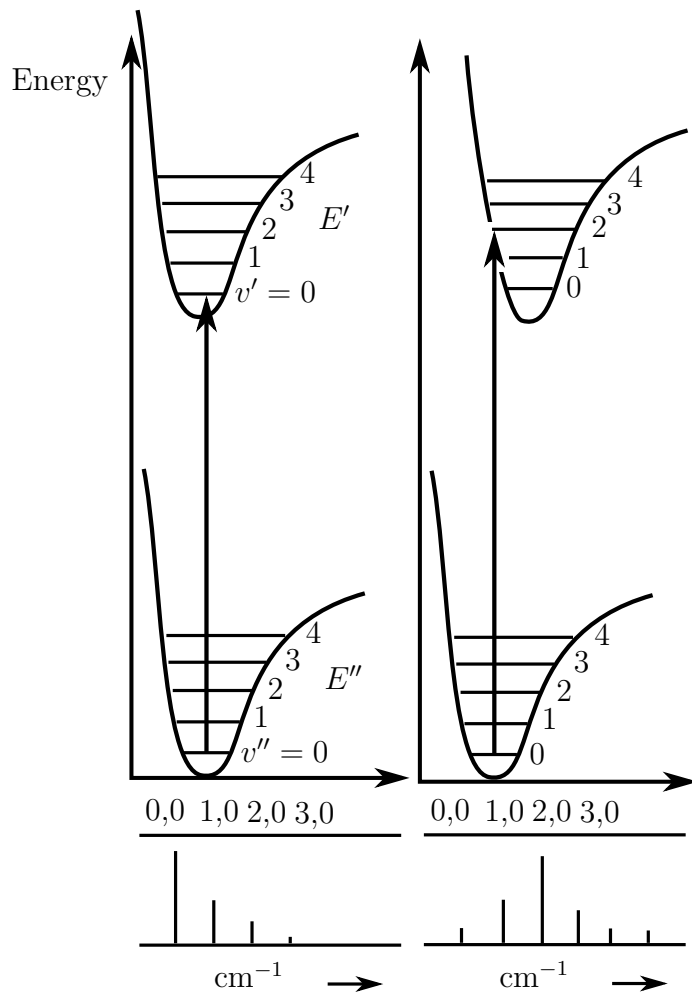


Figure 1.2.: Illustration of the Franck-Condon principle. Potential curves for either the same equilibrium core distance in the excited state or a bigger core distance in the excited state (after Haken and Wolf (2006) p. 276).

`(fig:flu-condon)`

212 spin (due to spin-orbit coupling¹). This process is called *intersystem crossing*. This
 213 mechanism populates the first triplet state T_1 . A transition into the ground state
 214 S_0 would need another spin-flip of the electron and is quite improbable. Therefore
 215 the triplet state has a long lifetime (several seconds). The radiative decay is called
 216 phosphorescence.

217 The *fluorescence quantum yield* η of a fluorophore is defined as the quotient of
 218 the number of emitted (fluorescence) photons and the number of absorbed photons.
 219 In dyes like rhodamine 6G (in ethanol $\eta = 0.94$ Fischer and Georges (1996)) or
 220 anthracene (9,10-diphenyl anthracene in cyclohexane $\eta = 0.90$ Hamai and Hirayama
 221 (1983)) its value can be nearly 1 for an appropriate solvent.

¹The probability of a spin flip is increased if heavier atoms (e.g. bromide) are part of the molecule.

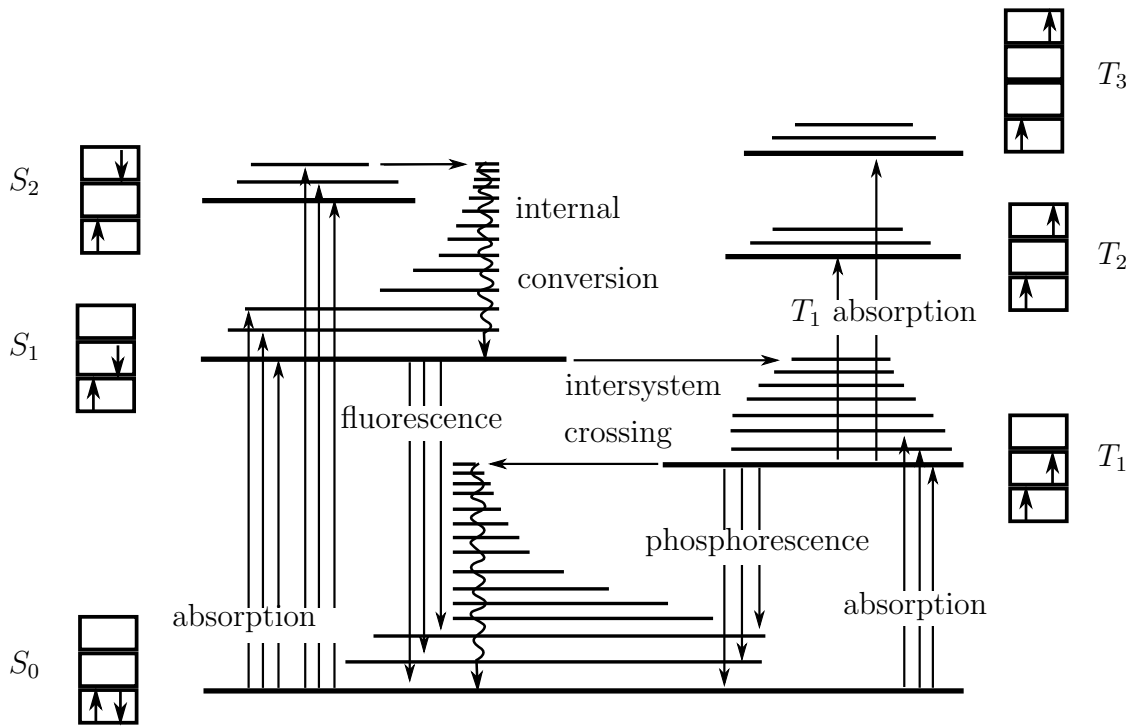


Figure 1.3.: A typical energy level diagram. The boxes with up and down arrows symbolize the spin of the outer electrons (after Haken and Wolf (2006)).

`(fig:flu-level)`

222 1.1.1. Photobleaching and phototoxicity

If a fluorophore molecule enters the T_1 state it cedes to emit photons for a long time. The excited molecule could also change its structure into some non-fluorescent form or react with a neighbour. All these things result first of all in a decreasing fluorescence signal – which is called *photobleaching*. Another effect is that the excited fluorophores impair living cells. It is a curious quirk of nature that the ground state of the oxygen molecule is a triplet state ${}^3\text{O}_2$. If an oxygen molecule hits a T_1 fluorophore, e.g. ${}^3\text{Chlorophyll}^*$, the energy of the dye can be transferred to the oxygen (Haken and Wolf (2006) p.438):



The resulting singlet oxygen is very reactive and quite hazardous inside living creatures. Plants have developed several protection mechanisms, if they are exposed to too much light. Within the cells they reorient and shift their chloroplasts in order to expose them to less light. However, they even have a molecular protection mechanism: They transfer the energy of the chlorophyll onto carotenoid molecules

1. Introduction

236 and can prevent the hazardous *phototoxicity* effects of singlet oxygen.

237 Nowadays many methods are known to reduce photobleaching. Supplant oxygen
238 with noble gases or remove it enzymatically. Depopulate the triplet state by adding
239 reducing as well as oxidizing agents to the solvent (Vogelsang et al. 2008). For fixed
240 samples it helps to use different solvents than water.

241 All these techniques work after the hazardous chemicals have been produced. In
242 order to reduce phototoxicity even more it makes sense to think about the light
243 management in the microscope.

244 1.2. Conventional microscopes

245 Microscopes that are in common use today do not optimally excite fluo-
246 rophores within the specimen. In this section we outline how these micro-
247 scopes work. We explain how out-of-focus blur severely limits the performance
248 of the widefield microscope. Then we discuss how confocal microscopy im-
249 proves the sectioning capability at the cost of increasing the phototoxic load
250 on the specimen.

251 The basic building block of microscopes are lenses. A lens is a piece of glass with
252 two polished spherical (a shape of lower symmetry is much harder to manufacture)
253 surfaces. Light is slower in glass than in air. The shape of a lens redirects photons
254 and the thickness of the material can delay them. A lens focuses a parallel beam of
255 light into a spot on its focal plane. The distance between focal plane and the region
256 where the rays start to converge is called focal length.

257 The yellow beam in Figure 1.4 a) represents rays that start from the intersection
258 O of the optical axis and the front focal plane of the objective. The objective collects
259 the rays and collimates them into a beam that is parallel to the optical axis. After
260 traversing the tube length $f + f_{\text{TL}}$ the detection tube lens TL1 focuses the rays on
261 the intersection O' of its focal plane (the intermediate image plane) and the optical
262 axis.

The blue beam corresponds to rays that start from an off-axis point P in the front
focal plane of the objective. Behind the objective the blue beam is a parallel beam.
However, the beam isn't parallel to the optical axis. The tube lens TL1 focuses the
blue beam into a spot at P' on its focal plane. Using the theorem of intercepting
lines one obtains for the magnification M :

$$M = \frac{\overline{O'P'}}{\overline{OP}} = \frac{f_{\text{TL}}}{f}. \quad (1.2) \{?\}$$

1. Introduction

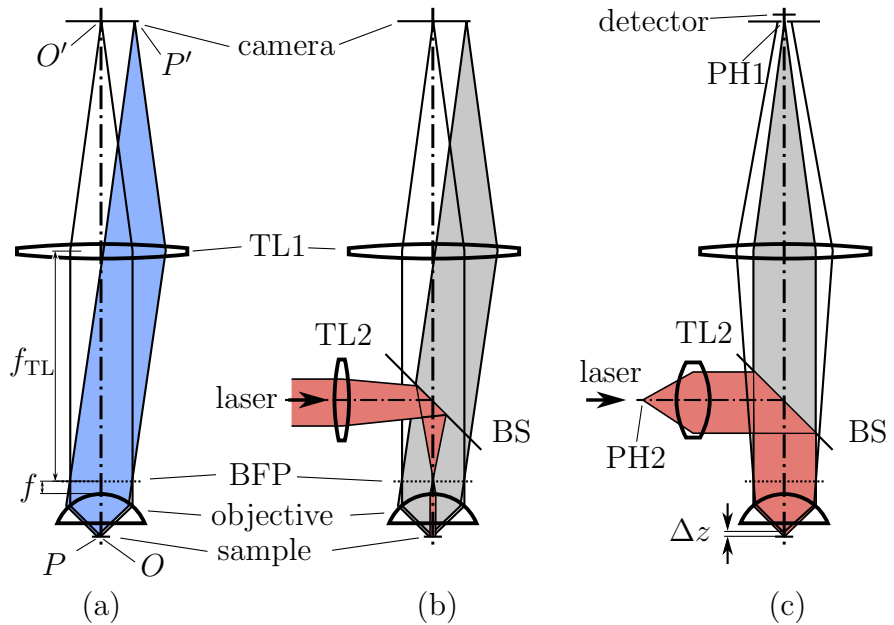


Figure 1.4.: **a)** Schematic of a modern microscope. The sample is in the front focal plane of the objective. The detection tubelens TL1 forms a magnified image on the camera. **b)** Widefield epifluorescence excitation. The excitation tubelens focuses a laser into the back focal plane (BFP). The beam is reflected by a dichroitic beam splitter (BS) towards the objective. An extended area in the specimen is illuminated. Fluorescence light of lower wavelength returns through the objective, is transmitted through BS and forms an image on the camera. **c)** Confocal microscope. A pinhole PH2 is imaged as a diffraction limited spot into the specimen. Returning fluorescence light is only detected when it passes through an aligned pinhole PH1. This configuration rejects light that doesn't originate from the front focal plane (green) of the objective.

:widefield-microscope)

263 In our microscope we use an objective with magnification $M = 63$. The focal length
 264 of the tube lens is 164.5 mm for most Zeiss microscopes. Therefor the focal length
 265 of our objective is $f = 2.61$ mm.

266 Assuming we have a metal mirror with two small ($\phi < 120$ nm) holes in the
 267 reflective coating with $2 \mu\text{m}$ distance between them. We put this object into the
 268 front focal plane of the objective and position a camera on O' . When illuminating
 269 the mirror from the side opposite to the objective, the camera will show two spots
 270 with $126 \mu\text{m}$ distance.

271 Note that Figure 1.4 depicts a thin-lens model of a high numerical aperture ob-
 272 jective that fulfils Abbe's sine condition. A real objective contains in the order of
 273 ten coated lenses of different glass and crystalline materials. Their curvatures, po-
 274 sitions and materials were all carefully chosen, taking into account manufacturing

1. Introduction

tolerances and wavelengths, so that the microscope behaves exactly as the thin-lens model predicts. Diffraction at the periphery of the pupil in the back focal plane dictates the resolution, one can achieve inside of the sample.

It is quite possible that heating to 37 °C will ruin such a high-precision instrument. A related source of aberrations (departure of design performance) is the refractive index inside of the specimen. In Appendix B.6.3 we describe a more complicated model that can predict the effect of embedding the sample in water (instead of immersion oil with the same refractive index as the glass).

1.2.1. Widefield epifluorescence microscope

Fluorescence photons are emitted in all directions, independent of the original illumination direction. Therefor it is convenient to use the objective for excitation as well as detection. This mode of microscopy is called epifluorescence (Greek: επι; on, above). One advantage is that even (the frontal side of) opaque specimen can be imaged. Furthermore it is beneficial that the illumination needs to be aligned only once.

The red beam in Figure 1.4 b) is a parallel laser. The excitation tube lens TL2 focuses the beam into the back focal plane (BFP) of the objective. The beam is reflected at a dichroitic beam splitter (BS). This is a glass plate that has been coated with dielectric layers. The refractive index, thickness and sequence of the layers are designed so that the excitation light is reflected towards the objective but lower energy fluorescence light returning from the objective is transmitted towards the camera. Behind the objective the beam is parallel and illuminates the specimen.

Non-uniformity due to coherent interference

Note that tiny dirt particles and coherent interference in laser beams can produce unwanted non-uniformities in the illumination. As a remedy sometimes the spatial coherence of the laser is reduced. Often incoherent light emitting diodes, mercury or xenon arc lamps are used instead of lasers. In the latter case the dichroitic beam splitter is preceded by a band pass filter that selects the useful part of the lamp's spectrum.

However, independent of the choice of the light source, the widefield microscope in epifluorescence configuration exposes many layers of the sample. This leads to fluorescence of out-of-focus fluorophores (molecules that are not in the front focal plane). The objective collects their light and forms a blurred image on the camera.

308 **Deconvolution**

309 When a stack of several slices of an object is obtained, it is possible to suppress
 310 the blurred part of each image in all the others. These algorithms (deconvolution)
 311 can improve the perceived quality of images in some stacks. However, there are two
 312 fundamental problems:

313 First the “missing cone problem” prevents focusing on a homogeneous fluorescent
 314 plane. Physics dictates that there always is a gap in the transfer function of the
 315 objective when the fluorescence process is linear and the objective collects only
 316 photons from one half space.

317 Second: Even with ideal detectors there is photon shot noise in the image. In
 318 deconvolution algorithms the image of one slice is improved by subtracting blurred
 319 versions of the other slices. When the blurred intensity is large, its shot noise is
 320 high as well. The noise isn’t reduced by subtraction and a faint in-focus image can
 321 be severely deteriorated by the noise of the out-of-focus light.

322 **1.2.2. Confocal microscope**

323 One way of addressing both problems of the widefield microscope is depicted in
 324 Figure 1.4 c). In the confocal microscope the field of view isn’t illuminated instan-
 325 taneously. The excitation tube lens TL2 collimates the light coming from a pinhole
 326 PH2 and illuminates the full back focal plane of the objective. In the front focal
 327 plane of the objective the red beam then converges to illuminate the smallest pos-
 328 sible (by diffraction) single spot. However, out-of-focus fluorophores are still being
 329 excited by the hour-glass shaped illumination.

330 The eponymous idea of the confocal microscope is to replace the camera with
 331 a pinhole PH1. This pinhole doesn’t affect the light detected from in-focus fluo-
 332 rophores. However, an out-of-focus fluorophore that is defocused by Δz towards the
 333 objective will lead to a diverging beam (green) at the tube lens and will be imaged
 334 into a point behind the focal plane of the tube lens. The pin hole only transmits a
 335 part of the circle of confusion. Hence defocused fluorophores contribute less to the
 336 sensor signal.

337 An image of the in-focus fluorophores is obtained by scanning the pinholes over
 338 the field of view and measuring intensity at each position individually. The optical
 339 removal of out-of-focus light prevents degradation of the signal by its shot noise
 340 and improves the point-spread function of the objective (fixing the “missing cone”
 341 problem). Note however, that some information is lost which would be obtained in
 342 a widefield microscope with deconvolution.

343 The confocal microscope was invented in 1955 ([Minsky 1961, 1988](#)) to reduce the
 344 influence of scattering effects in neuron samples stained by Golgi's method. This
 345 invention preceded the laser and was unfortunately not put into practical use until
 346 three decades later (Amos et al. 1987).

347 **1.2.3. Phototoxicity in conventional microscopes**

348 When imaging living specimen we should distinguish between useful and unneces-
 349 sary excitation. Taking into account the detection capabilities of objective lenses
 350 we should maximize the ratio of in-focus to out-of-focus fluorescence. The epifu-
 351 orescent widefield and confocal microscope surely do not represent an optimum in
 352 this regard.

353 The following chapter will introduce other microscopy techniques that are more
 354 considerate of where to deposit excitation power within the specimen.

355 **1.2.4. Two photon laser scanning fluorescence microscopy**

356 If an intense subpicosecond pulse of infrared light is focused into a spot in the
 357 sample, non-linear two photon absorption can occur (Denk et al. 1990). Infrared
 358 light is scattered less than light of half the wavelength. The phototoxicity in the
 359 focus is higher than in a single-photon microscope with comparable excitation rate.
 360 However there is no excitation in the out-of-focus region. Therefor a detection pin
 361 hole is not required.

362 This technique has greatly improved depth of penetration and sensitivity of in
 363 situ imaging.

364 **1.3. Image detectors in widefield microscopy**

`{sec:ccd-intro}` 365 Here we describe CCD sensors and their characteristics.

366 Charge-coupled devices are semiconductor devices that contain a 2D grid of capac-
 367 itors, formed by at least three groups of electrodes (phases). Cycling the voltage
 368 on these electrodes allows to push charges, which has been accumulated under the
 369 capacitors (registers) into their neighbours. They turned out to be the ideal tool to
 370 move charges, produced by photon absorption in light sensitive diodes, across the
 371 substrate into read out logic.

372 Forty years of development lead to imaging devices with remarkable charge trans-
 373 fer efficiency, high quantum efficiency (up to 95% with back illumination) and very

1. Introduction

374 low dark currents. Until ten years ago the performance of CCD imagers in the low
375 light regime was limited by the noise of the read out amplifier (a few electrons per
376 pixel rms).

377 Now we have electron multiplying CCD (EM-CCD) technology, which allows com-
378 parably good performance at low photon numbers (Mackay et al. 2001; Robbins et al.
379 2003) and moderate read out speeds (tens of MHz). EM-CCDs contain a row of
380 additional registers in front of the read out circuit. There one of the three phases
381 is clocked with a much higher voltage (up to 40 V) than is needed purely for charge
382 transfer (~ 6 V). The large electric fields cause charge carriers to be accelerated to
383 sufficiently high velocities that additional carriers are generated by impact ioniza-
384 tion. The charge multiplication per transfer is small ($\sim 1\%$) but by using several
385 hundred registers a substantial gain in the number of charges can be achieved. In
386 microscopy we usually work with gains of up to 300. Higher gains are possible but
387 limit the dynamic range.

388 The charge amplification helps to push the read noise from ~ 40 electrons rms
389 to significantly below 1 electron rms — in effect creating a sensor limited only by
390 the photon noise. However the the multiplicative nature of the gain leads to a
391 perceived reduction in the quantum efficiency of the sensor (excess noise factor),
392 i.e. an image with 100 photons/pixel without gain will look like the same image at
393 only 50 photons/pixel with EM-gain (see Appendix A).

2. Other approaches of light control

This chapter gives an overview of current microscopy techniques that reduce unnecessary fluorescence excitation and reduce phototoxicity. In *light sheet microscopy* an oblique sheet of light illuminates the sample without exposing too many out-of-focus fluorophores. *Controlled light exposure microscopy* (CLEM) takes into account the in-focus fluorophore distribution and iteratively improves the signal to noise ratio of the measurement. Finally *light field microscopy* allows instantaneous and complete control of all parameters of the incoherent light exposure.

2.1. Light sheet fluorescence microscopy

Light sheets can be directly created with separate optics to illuminate the sample from an orthogonal direction. Another promising method to create a sheet is to use a high numerical aperture objective near the total internal reflection angle. Diffraction couples the minimum width of the sheet and the extent of the area, where the sheet's width is constant. There is a trade-off between sheet width and field of view.

The idea of illuminating a sample from the side dates back quite far into the history of microscopy. Already one hundred years ago an objective perpendicular to the detection objective was used for illumination of the focal plane in the specimen. This dark field technique was used to characterize gold nano particles in gold ruby glass (Siedentopf and Zsigmondy 1903).

Eventually this technique was applied to fluorescence microscopy. First to analyze cochlea specimen (Voie et al. 1993) and more recently for the development of embryos (Huisken et al. 2004). Results in the latter paper have sparked interest in the technique at many labs (Santi 2011).

2.1.1. Light sheet generation with cylindrical lens

Figure 2.1 shows how the light sheet can be focused into the specimen using a cylindrical lens. Huisken et al. (2004) employ a water dipping objective with long

2. Other approaches of light control

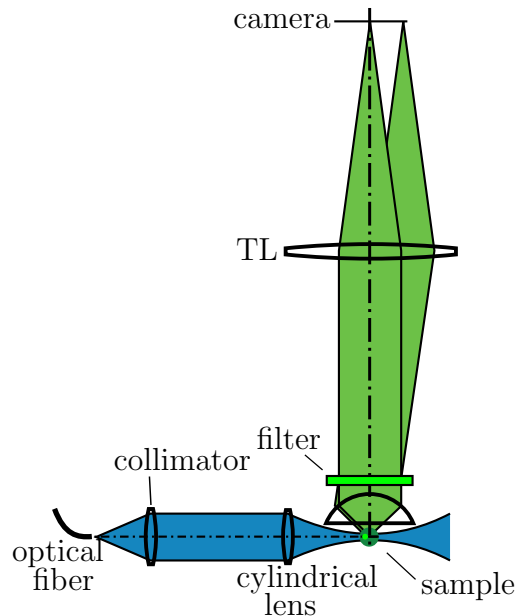


Figure 2.1.: Schematic of SPIM (selective plane illumination microscopy). A cylindrical lens illuminates the specimen with a thin sheet of light along the focal plane of the objective. Rotating the sample and/or moving it along the axis allows to reconstruct a sectioned 3D volume of the fluorophore concentration with improved light utilization compared to conventional microscopes.

`{fig:spim}`

422 working distance (1...2 mm) and comparatively low NA for detection. A $10\times$ ob-
423 jective with $660\ \mu\text{m}$ field of view diameter is used with a sheet that varies less than
424 42% in thickness ($6\ldots8\ \mu\text{m}$). The light sheet not only improves sectioning and
425 contrast but also improves the axial resolution from originally $14\ \mu\text{m}$ by nearly a
426 factor of two.

427 The axial resolution of detection objectives of higher numerical aperture isn't
428 improved so easily over an extended field of view. Shading effects, diffraction and
429 refraction can deteriorate the light sheet. As an improvement of the technique it
430 was suggested to rotate the specimen or illuminate with multiple sheets of light
431 from different directions.

432 Other improvements involve a Bessel beam that is scanned to illuminate a plane.
433 This intensity distribution is “self-reconstructing” and can compensate better for
434 obstacles in its path. It comes with the cost that the light sheet isn't as confined. Si-
435 multaneous structured illumination and 2 photon effects were suggested to improve
436 this.

2. Other approaches of light control

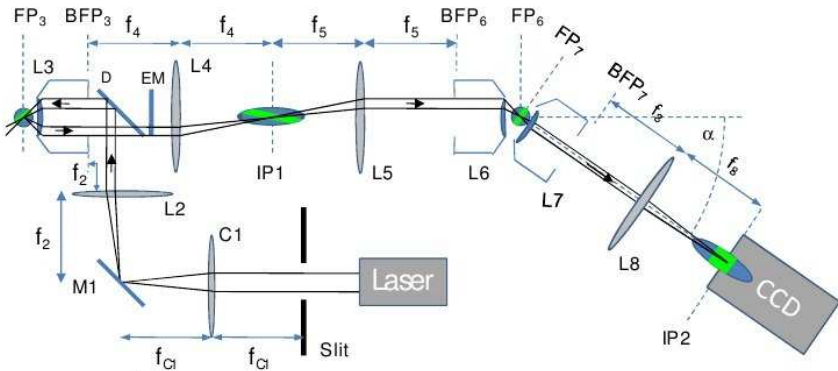


Figure 2.2.: Schematic of oblique plane microscopy (OPM). An index matched sample is excited using an oblique plane of light. As the illumination plane isn't lying in the focal plane, out-of-focus fluorophores on the periphery of the field of view are excited. Two additional objectives in the detection path are used to reconstruct an aberration free image of all the excited fluorophores (drawing from Dunsby (2008)).

`{fig:dunsby}`

437 2.1.2. Light sheet generation using the detection objective

?`{sec:hilo}`?
 438 Modern high numerical aperture objectives allow to illuminate an *index matched*
 439 sample with a half angle of up to 70° . This enables illumination of an oblique and
 440 thin sheet of light in the sample just as in selective plane illumination microscopy.
 441 However this technique (oblique plane microscopy, OPM) has the advantage, that
 442 only one objective is needed to be close to the sample and it will work with specimen
 443 in conventional microscope slides. One difficulty is that the excited fluorophores are
 444 severely defocused in the intermediate image plane. is that (see Figure 2.2). Dunsby
 445 (2008) describe how to rotate the observational plane optically in order to recover
 446 an aberration free image from the oblique illumination plane. They reimagine the
 447 sample through two additional objectives.

448 Biological specimen are often not index matched but have a lower index $n_e \approx 1.33$
 449 than the immersion oil $n = 1.52$. As indicated in Figure 2.3 the refraction at
 450 the interface between cover slip glass and embedding medium can be exploited to
 451 illuminate specimen with a light sheet that is nearly parallel to the focal plane. This
 452 technique is called highly inclined and laminated optical sheet microscopy (HILO)
 453 (Tokunaga et al. 2008; Konopka and Bednarek 2008).

454 Note that the index mismatch between embedding and immersion medium will
 455 introduce aberrations (mostly spherical) which will limit the imaging depth into the
 456 sample.

redraw

2. Other approaches of light control

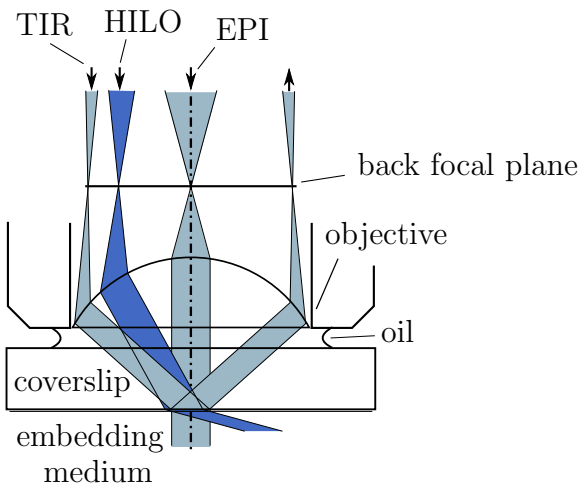


Figure 2.3.: Schematic of rays in HILO (highly inclined and laminated optical sheet) technique. The specimen is embedded in a medium of lower optical density than the cover slip. For a very high illumination angle (point on the periphery of the back focal plane) the light would be reflected at the cover slip-medium interface due to total internal reflection. For HILO a point on the back focal plane, that is closer to the optic axis is illuminated. The light enters the embedding medium in a highly inclined angle and only a thin sheet in the focal plane is illuminated (after Tokunaga et al. (2008)).

`<fig:hilo>`

457 2.2. Scanning techniques for improving light 458 utilization

459 2.2.1. Controlled light exposure microscopy (CLEM)

460 `<sec:CLEM>` The confocal microscope (see Figure 1.4 c) allows another adaptive illumination
461 technique. A slice of a specimen is partitioned into three different regions. Areas
462 with no fluorophores (A), high concentration of fluorophores (C) or a concentration
463 in between (B).

464 Ideally, areas A that don't contain fluorophores should only be exposed until
465 fluorophore content is ruled out. The other two classes B and C should be exposed
466 until the same number of fluorescence photons have been detected. This would
467 result in an image with constant signal to noise ratio. Unfortunately due to the
468 photon nature of light sometime a region of type B is incorrectly treated as A which
469 introduces dark pixel artifacts in the image (Hoebe et al. 2010).

470 In conventional microscopes areas of class C with high fluorophore concentration
471 are generally exposed too much. Their signal to noise ratio would be high but this
472 doesn't increase perceived image quality. Furthermore regions above and below the

read
reference

2. Other approaches of light control

was
that
first,
get

473 focal plane have been unnecessarily subjected to high exposure.

474 This technique was first presented in (Hoebe et al. 2007) followed by an inde-
475 pendent similar version with adaptive control of the laser power for two photon
476 microscopy (Chu et al. 2007).

477 2.2.2. Acousto-optic deflectors for fast beam steering

478 In a conventional confocal microscope the beam is steered by two galvanometer
479 mirrors. This technique offers very good light throughput and is sufficient to obtain
480 rectangular images. However the inertia of the mirrors severely limit the access rate
481 of spots in the focal plane.

482 Replacing the mechanical mirrors with an acoustic wave in a transparent material
483 (TeO_2) enables $4\ \mu\text{s}$ switching time (Otsu et al. 2008) and even allows focusing to
484 points outside of the focal plane (Reddy et al. 2008). These acousto-optic deflectors
485 have lower efficiency (70% for two AODs) and show chromatic aberrations.

486 However as descanning isn't necessary in two photon microscopy the lower effi-
487 ciency (in the excitation path) is hardly an issue. Therefor this technique for the
488 first time enables "random access" of 3D coordinates in the sample.

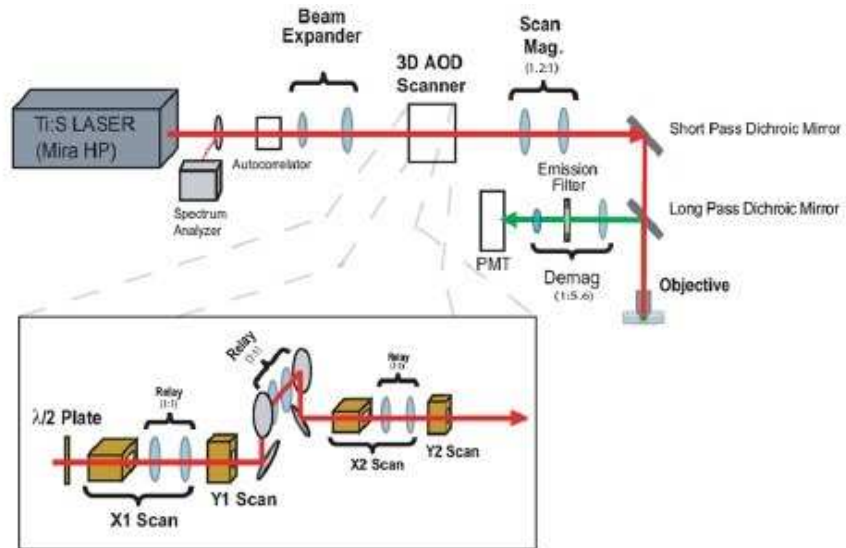


Figure 2.4.: Schematic of an acousto-optic deflector (AOD) illumination system with z focusing. Figure taken from (Reddy et al. 2008)

?<fig:aod>?

489 **2.3. Non-scanning**

490 **2.3.1. Direct illumination**

491 An obvious method for doing spatial control is to image a two-dimensional array
of high-power micro-LEDs into the specimen. However the problem is to achieve

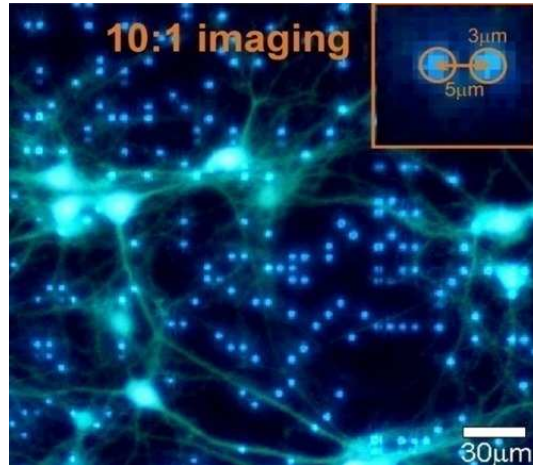


Figure 2.5.: Overlay combining widefield micro-LED illumination and fluorescence imaging YFP tag expressed in neurons, taken from (Grossman et al. 2010).

?<fig:led-array>?

492 sufficient *irradiance* (LEDs angular emission profile is often lambertian, i.e. the back
493 focal plane of the objective would be over-illuminated and a lot of light lost) and
494 *fill factor* (it is difficult to put a lot of LEDs close together). The technique has
495 been demonstrated using a 64×64 array of $20 \mu\text{m}$ micro-emitters with $50 \mu\text{m}$ pitch
496 (Grossman et al. 2010). The LEDs can be switched at millisecond speed and emit
497 at $(470 \pm 22) \text{ nm}$.

498 This technique enables interesting experiments where processes are influenced by
499 light (optogenetics) but the targets ideally have to be located in the focal plane.
500 Also it must be verified that the illumination cone of each LED image doesn't affect
501 the measurement, i.e. activate the specimen in out-of-focus regions.

502 Nevertheless once the LED (or VCSEL) arrays become available in interesting
503 spectral ranges we might see the direct illumination techniques more often.

505 2.3.2. Intensity modulation

506 Programmable array microscopy

507 A technique similar to controlled light exposure microscopy (CLEM, section 2.2.1)
 508 has been implemented in a programmable array microscope (PAM) (Caarls et al.
 509 2011) (minimized light exposure PAM, MLE-PAM). Like our microscope the PAM
 510 images a pattern into the sample using a spatial light modulator. In addition to
 511 our system the same SLM is used in the detection path to recover an image of only
 512 the in-focus fluorophores.

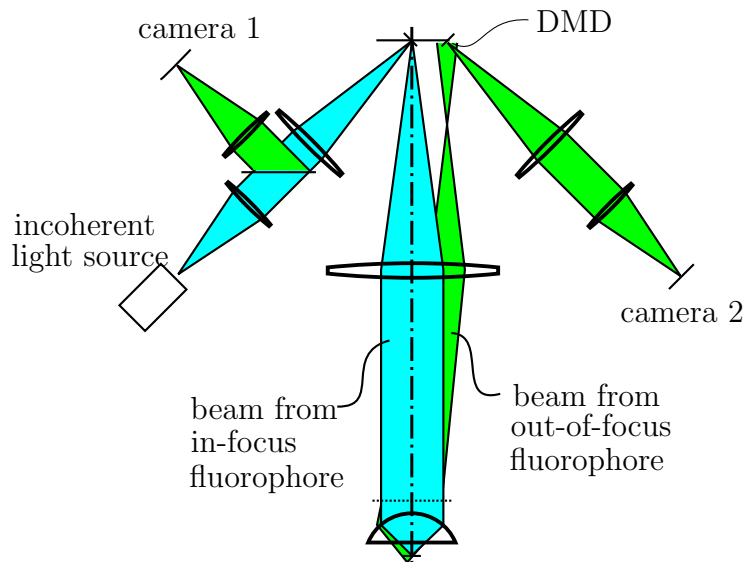


Figure 2.6.: Schematic of a programmable array microscope (PAM) (after Verveer et al. (1998)). A digital micro mirror device (DMD) containing an array of tilttable mirrors is imaged into the focal plane of the objective. Returning fluorescent light from out-of-focus fluorophores is distributed onto both cameras. In-focus fluorescence is only imaged onto camera 1.

?<fig:pam-sketch>

513 Light field microscopy

514 Interesting work on light fields originally started in the macroscopic domain of
 515 cameras (Lippmann 1908) and was eventually applied as a technique for microscopy
 516 (Levoy et al. 2006, 2009; Zhang and Levoy 2009). This approach is built on imaging
 517 through an array of microlenses.

518 A microlens array is placed behind the intermediate image plane (see Figure 2.7).
 519 The light that illuminates one microlens corresponds to one spot in the focal plane
 520 of the sample. The camera is positioned in the focal plane of the microlenses and

2. Other approaches of light control

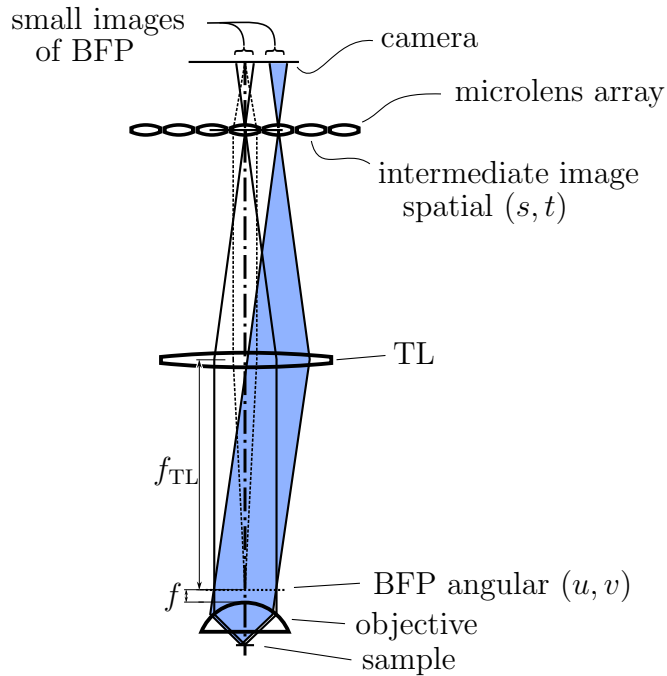


Figure 2.7.: Schematic of microlenses in intermediate image plane (after (Levoy et al. 2006))

captures an image of the back focal plane behind each microlens (see dashed ray bundle).

The camera captures the four dimensional light field leaving the specimen with spatial coordinates (s, t) and angular coordinates (u, v) . This data enables computational viewpoint shifting, refocusing, extended depth of field and aberration correction of the detected fluorescence emission.

Figure 2.8 shows bundles originating from an out-of-focus point. Each of the microlenses that are hit by the circle of confusion reimagine a fraction of the angular range of into their images. This process is crucial because here a lot of the original image information is lost. The intensities from the sub-images on the camera can't later be recombined in order to, e.g. recover a high resolution image of the defocused point (R. Heintzmann, personal communication, November 22, 2011).

The light field microscope doesn't utilize the full resolution of high-NA objectives. This will prevent the use of this technique in its current form for the detection path of microscopes.

However, the same ideas can be applied in the excitation path. For illumination purposes lower resolution will often suffice. The light field technique allows unique control of excitation light intensity and angles in each point of the sample plane.

2. Other approaches of light control

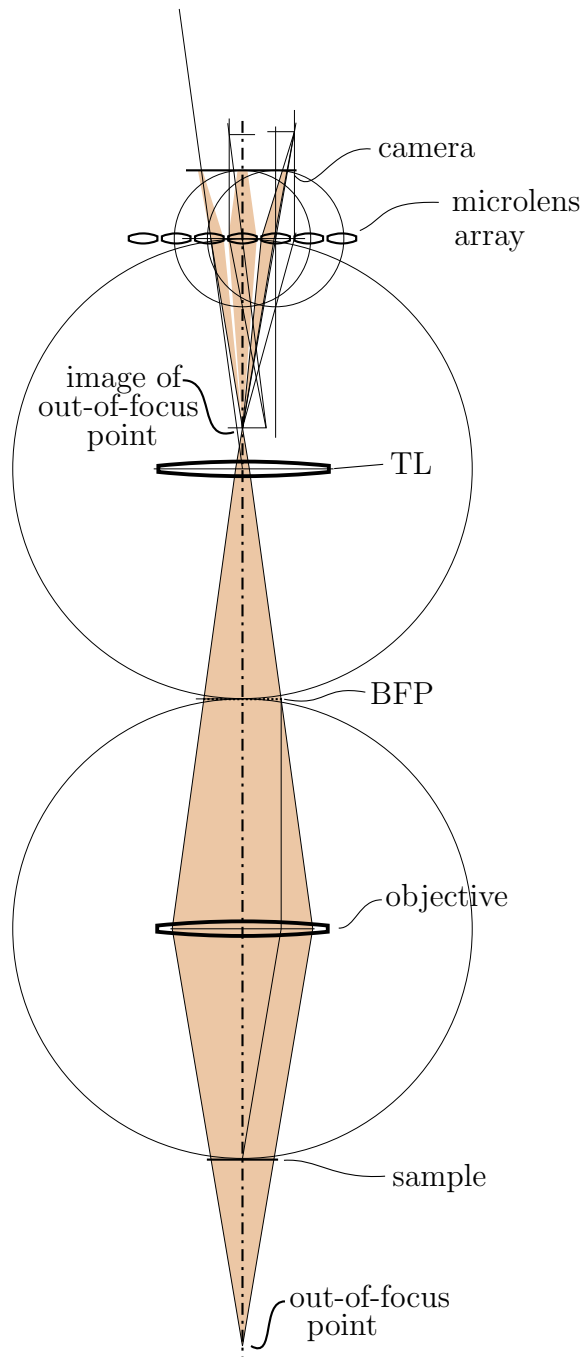


Figure 2.8.: Construction of an out-of-focus bundle through the light field microscope. In order to improve the readability of the drawing, the magnification in the microscope was set to 1 : 1 (focal lengths of tube lens and objective are equal). An on-axis sample point originating from below the focal plane of the objective is imaged into an on axis point between tubelens and microlens array. Three of the microlenses reimagine the point into three points behind the plane of the camera.

rolens-levoy-sketch_2

539 **2.3.3. Temporal focusing**

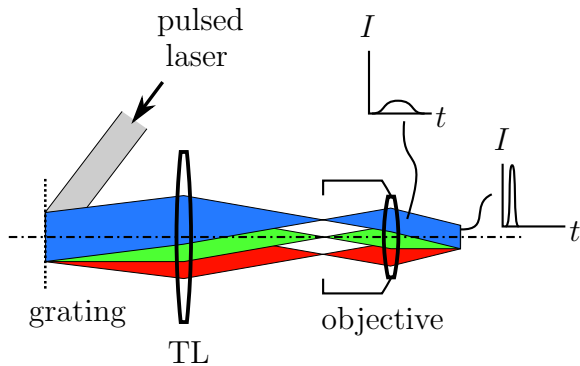


Figure 2.9.: Schematic of temporal focusing (after (Oron et al. 2005)). A grating in the intermediate image plane separates the pulse into its spectral components. Out-of-focus areas of the specimen are illuminated with a longer pulse. Only the in the focal plane all spectral components interfere coherently and form a short intensive pulse.

?<fig:oron)?

540 The axial extent of ultra-short laser pulses can be as thin as a few microns. A
 541 parallel beam can be split into different spectral components by a grating in the
 542 intermediate image plane (Oron et al. 2005). The tube lens focuses the diffraction
 543 pattern into a line in the back focal plane of the objective.

544 The objective, which has to be corrected for chromatic aberration and dispersion,
 545 then focuses all the beams into the focal plane. Different spectral components
 546 arrive in the focal plane at the same time. Out-of-focus points see an extended
 547 illumination. For a high NA objective a pulse duration of $\tau = 20\text{ fs}$ results in a slice
 548 of $z \approx \tau c/2 \approx 3\mu\text{m}$ thickness around the focus, where the beam has significant
 549 intensity.

550 Using this technique it is possible to build a widefield two photon microscope.
 551 That only excites fluorophores within the focal plane. The technique can be further
 552 improved by spatially modulating the beam in the intermediate image plane for
 553 CLEM like performance.

554 **2.3.4. Phase modulation**

555 **Digital holography**

556 Certain types of liquid crystal spatial light modulators can be used to modify the
 557 phase of light. When such a device is placed into the back focal plane of a lens,
 558 it is possible to control the light distribution in its front focal plane. An iterative
 559 algorithm (iterative Fourier transform algorithm, IFTA) can be used to establish a

2. Other approaches of light control

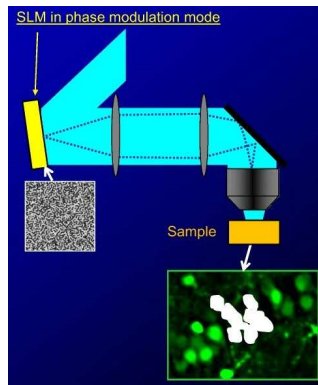


Figure 2.10.: Schematic of spatial illumination by phase holography

redraw

?<fig:phase-holo>?

560 phase image on the liquid crystal display that will result in an intensity distribution
561 in front of the lens.

562 This approach has been used to excite a two-dimensional pattern in the specimen
563 (Lutz et al. 2008; Zahid et al. 2010) and is advantageous especially for cases where
564 only small parts of the specimen ought to be illuminated. As opposed to conven-
565 tional intensity spatial light modulators the light can be redirected from dark areas
566 into the bright areas.

567 There is also a limited possibility to create three-dimensional patterns, e.g. several
568 points below, in and above the focal plane by displaying Fresnel zone planes. For
569 illumination usually a laser with non-zero interference length is employed. However,
570 this illumination contains an unwanted “speckle” pattern – noisy non-uniformities.
571 To a certain extent the contrast of the speckle pattern can be reduced by controlling
572 spatial and temporal coherence of the illumination (sweeping the frequency of the
573 laser or changing illumination direction while the detector is integrating).

574 Holographic control can be used with two photon excitation as well (Nikolenko et al.
575 2008) but this exacerbates the effect of speckles.

576 Generalized phase contrast (GPC)

577 A phase contrast microscope objective can be used to convert a phase image from
578 the intermediate image plane into an intensity image in the specimen (Rodrigo et al.
579 2008). Compared to digital holography hardly any computation is necessary. Yet
580 the phase spatial light modulator allows concentrating a lot of light even into a
581 small region of the specimen as opposed to other techniques which involve intensity
582 modulation and loose the light of dark areas.

modified
?
read
more
of
this

2. Other approaches of light control

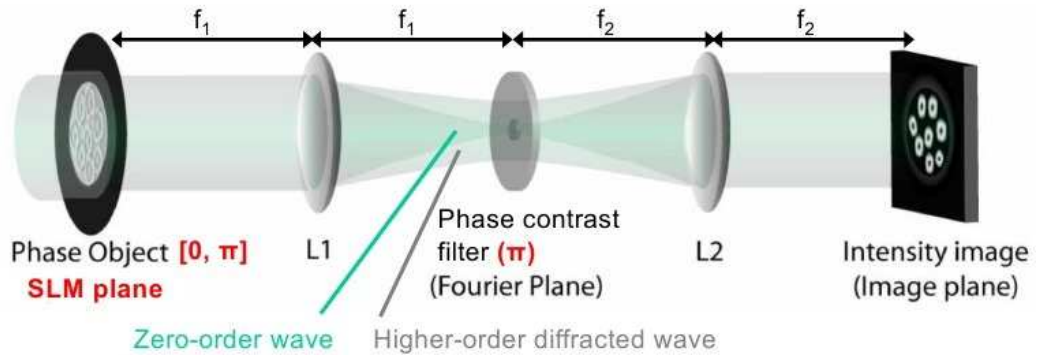


Figure 2.11.: schematic of generalized phase contrast (Rodrigo et al. 2008)

?<fig:phase>?

583 The generalized phase contrast method is suitable even with spatially incoherent
 584 illumination.

slightly
 ?

585 Generalized phase contrast and temporal focusing (TF-GPC)

586 The combination of generalized phase contrast and temporal focusing allows selec-
 587 tive uniform illumination of in-focus areas (Papagiakoumou et al. 2010). Usage of
 588 a phase spatial light modulator results in high light efficiency compared to intensity
 589 modulation. Splitting and recombination of the spectral components of the pulse
 reduce speckle noise considerably.

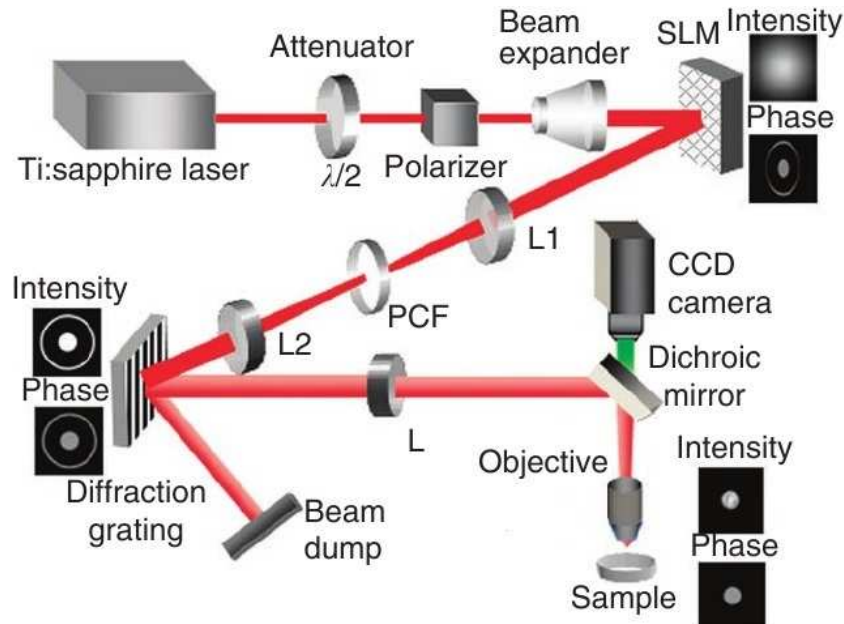


Figure 2.12.: Schematic of phase contrast with temporal focusing (TF-GPC) from (Papagiakoumou et al. 2010), PCF is a phase contrast filter

?<fig:tf-gpc>
 590

591 3. A prototype for spatio-angular 592 illumination

593 We give a general overview of the system, followed by more detailed expla-
594 nation of some if its components. Then we introduce a model that allows to
595 construct optimized masks for spatio-angular illumination.

596 3.1. Overview

597 Figure 3.1 shows a simplified schematic of our optical system. The uniform light
598 distribution from the end of a light mixing tunnel is imaged into the specimen. Two
599 spatial light modulators allow to modify the light intensity and angular distribution
600 of the light within the sample.

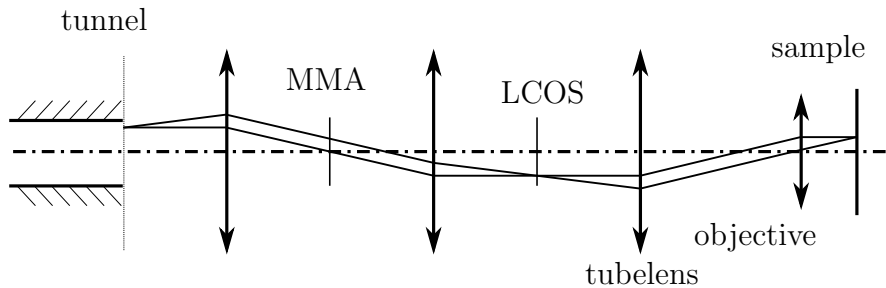


Figure 3.1.: Simplified schematic of the MEMI system. Light coming from the source is homogenized in an integrating tunnel. The light then traverses two spatial light modulators. The first of which (MMA) is imaged into the back focal plane of the objective and the second (LCoS) into the sample.

`(fig:memi-simple)`

601 Figure 3.2 visualizes how our optical system improves sample illumination. If the
602 LCoS illuminates one in-focus bead¹, the MMA can be used to prevent exposure of

¹Note that the LCoS acts as a Fourier filter on the information coming from the MMA. Therefor if all but a single pixel of the LCoS block the light, no angular control is possible (see also Appendix E).

3. A prototype for spatio-angular illumination

603 the out of focus bead in Figure 3.2 (a). Not exciting the out-of-focus bead has two
604 advantages:

605 1. There is less background light in the camera image, leading to a clearer image
606 of the in-focus information. It would be possible to computationally distin-
607 guish and subtract out-of-focus light by structured illumination methods but
608 these methods will not remove the poisson distributed photon noise of the
609 out-of-focus light.

610 2. Not exciting the out-of-focus areas is especially important for biological spec-
611 imen in order to reduce the phototoxicity of the imaging.

612 If an extended in-focus area should be imaged (Figure 3.2 (d)). Then multiple ex-
613 posures, each with different patterns on LCoS and MMA, can be combined into
614 an image of the in-focus information with minimal exposure of out-of-focus fluo-
615 rophores.

616 This technique requires prior knowledge about the fluorophore distribution in the
617 sample. In 3D time lapse imaging of developing embryos a good estimate is available
618 when the stacks are acquired with high enough temporal resolution. Opto-genetics
619 experiments can be designed such, that the 3D distribution of neurons is known
620 before single neurons are triggered by light without exposing its neighbours.

621 For some sample types an estimation and maintanance of the full 3D fluorophore
622 concentration within the sample is unpractical and might be unneccessary. Instead,
623 we believe we can project grating images with the LCoS and still vary the illumina-
624 tion direction with the mask on the MMA. The two camera images with structured
625 illumination could then be used to recover a sectioned image of the in-focus fluo-
626 rophore distribution (Lim et al. 2008; Bozinovic et al. 2008; Santos et al. 2009).
627 Acquisition of several such images with different MMA masks would allow to find
628 the angle with least out of focus contributions. Note that for this technique to work,

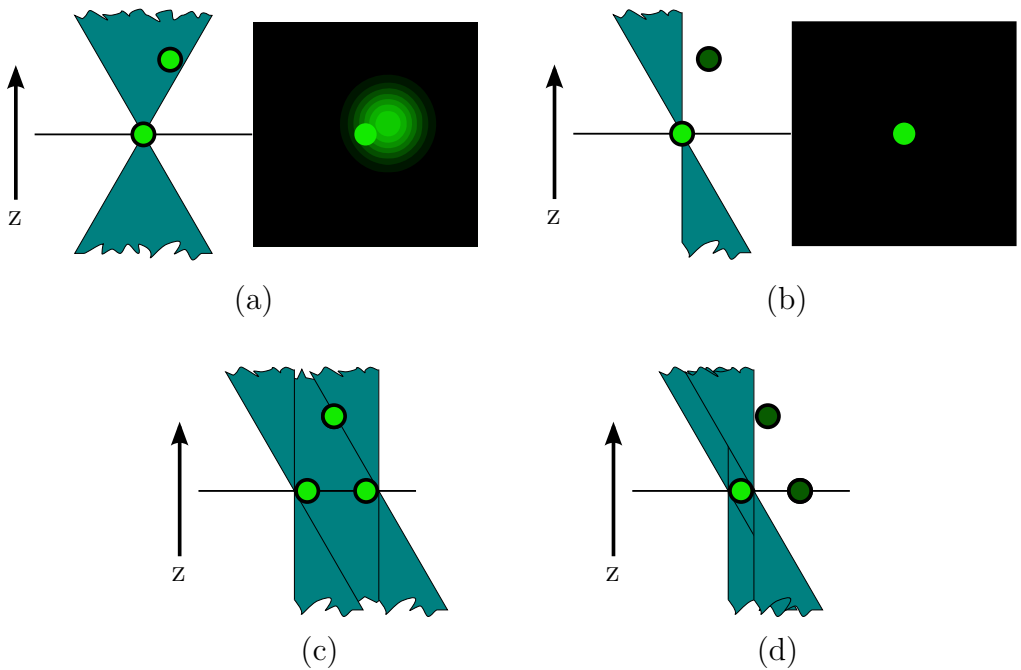


Figure 3.2.: (a) Two fluorescent beads are illuminated by all angles that an objective can deliver. The sharp image of the in-focus bead is deteriorated by blurry fluorescence of the out of focus bead. (b) Angular control allows selective illumination of the in-focus bead and results in a better image on the camera. (c) Angular control is insufficient, when an extended in focus area is illuminated. (d) However, simultaneous spatial and angular control allows sequential excitation of the in-focus beads while excluding the out of focus bead.

`<fig:hourglass-all>`

629 3.2. Detailed explanation of the optical components

630 In the real system the spatial light modulators are reflective. Also both displays are
 631 not direct intensity modulators. Figure 3.3 shows a schematic of the light path in
 632 the combined angular and spatial control system.

633 A laser light source is scrambled by a rotating microlens array and mixed in an
 634 integrating tunnel with a quadratic cross section.

635 The distance between the exit of the integration tunnel and the lens L_1 is equal
 636 to the focal distance of L_1 . The MMA is positioned in the other focal plane of L_1 .
 637 The micro mirror array (Berndt et al.)

638 ref

639 consists of 256×256 mirrors with a pitch of $16 \mu\text{m}$ (see Figure 3.5 and Figure 3.6).
 640 Each mirror hangs on two thin hinges and can be tilted by up to 2° by electrostatic
 641 fields. CMOS circuits below each mirror allow to maintain a constant tilt for hun-
 642 dreds of milliseconds. A dedicated control board can set new analogue voltages with

3. A prototype for spatio-angular illumination

643 10 bit resolution for each mirror in $850\ \mu\text{s}$. This enables framerates of up to 1 kHz
644 at duty cycles up to 50 %.

645 When all mirrors of the MMA are flat, an image of the tunnel exit F''' is formed
646 in the plane of the aperture B_1 . The size of the aperture is chosen to transmit just
647 this image. When mirrors of the MMA are tilted, they will slightly deflect the light,
648 so that it no longer passes through the aperture B_1 . B_1 acts as a Fourier filter (or
649 Schlieren optics).

650 If the mirrors of half of the device are deflected to fulfill the blaze conditions²
651 then the corresponding area in the Fourier filtered image in P' will be dark.

652 The lenses L_2 and L_3 relay the image of the tunnel exit F''' from F'' into the plane
653 F' with the LCoS (ForthDD SXGA, pixel pitch $13.62\ \mu\text{m}$). The polarizing beam
654 splitter (45° wire grid polarizing beam splitter, Moxtek) reflects linearly polarized
655 light towards the LCoS³. The electric field vibrates perpendicular to the paper
656 plane. Depending on the LCoS pixel state (on or off) an LCoS pixel can rotate the
657 polarization of the returning light, so that it is transmitted⁴ into the illumination
658 tube lens TL_{ill} by the PBS (see Figure 3.8 for a photograph showing tube lens, PBS
659 and LCoS).

660 The LCoS is ferroelectric (see Saleh and Teich (1991) and Goodman (1996) p. 192).
661 Its liquid crystals can swap very fast between two stable orientations. In order to
662 prevent a net current, which would eventually destroy the device, its driver always
663 displays an inverted image after the wanted one. Therefor it is necessary to shutter
664 the light source accordingly.

665 The lenses L_3 and TL_{ill} relay the Fourier filtered MMA image from P' into the
666 pupil P of the objective. In order to accommodate objectives with various back
667 focal plane diameters, the illumination tube lens is built out of three lens groups.
668 Its focal length can be varied from 222.8 mm up to 445.4 mm (see Figure F.1 for a
669 drawing with the focal length of the other lenses). The lens groups move such, that
670 the image of the LCoS behind TL_{ill} stays in infinity and the the MMA (plane P'') is
671 imaged into the pupil P , which is 250 mm behind behind the tubelens. Figure 3.7
672 shows the pupil plane P for two different settings of the focal length of the tube
673 lens.

674 Fluorescent light returns from the objective and is reflected by the dichroitic beam
675 splitter (DBS) through the detection tube lens TL_{det} and is imaged on the camera.

²This is limited by the maximum tilt angle and possible for wavelengths up to 800 nm

³In order to prevent spurious reflections at the PBS surface without wire grid and to improve contrast, the incoming light should already be polarized

⁴As it is used in transmission a curvature of the PBS doesn't affect the quality of the LCoS image in the sample F as if the PBS was used in reflection.

3. A prototype for spatio-angular illumination

676 Note that the detection works with full efficiency.

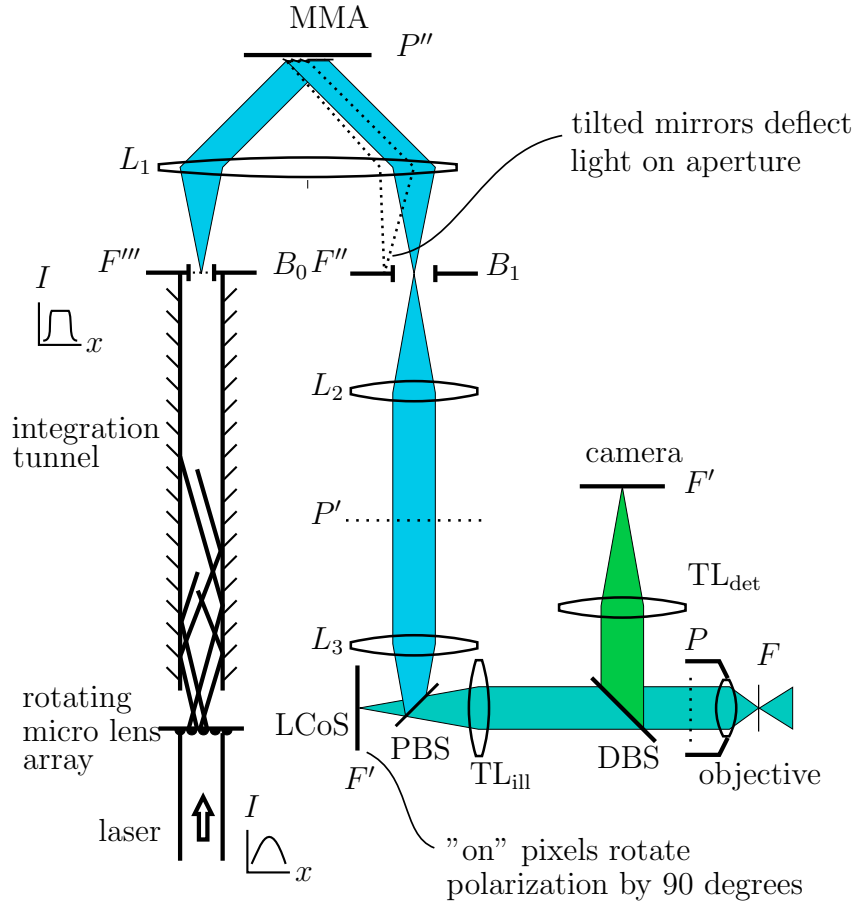


Figure 3.3.: Schematic of the light path through our microscope. Laser light enters from the lower left, is scrambled and homogenized to illuminate the full MMA and LCoS. F is the field plane in the sample and its primed versions are conjugated planes. P is the pupil of the objective. B_0 and B_1 are adjustable circular apertures. PBS is a polarizing beam splitter. DBS is a dichroitic beam splitter.

{fig:memi-real}

3. A prototype for spatio-angular illumination

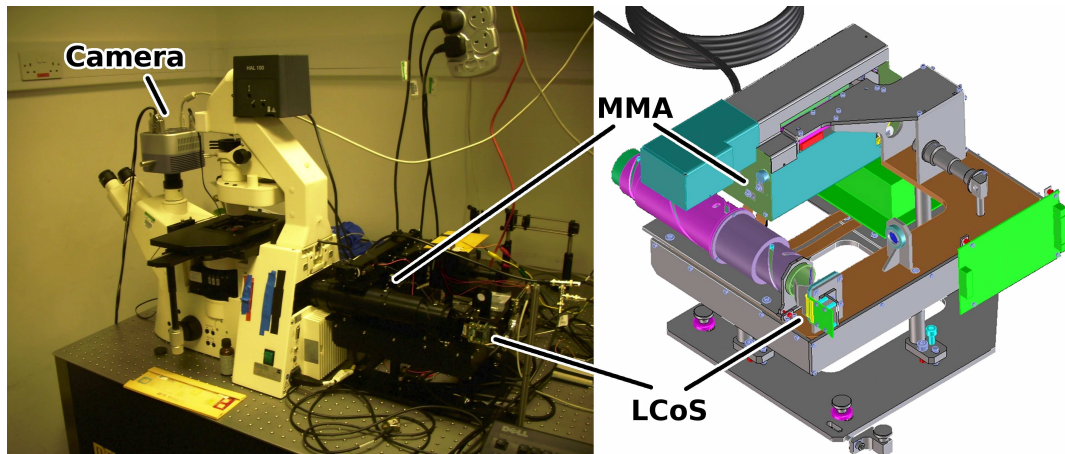


Figure 3.4.: The widefield epi-fluorescent microscope with attached illumination head. The positions of the two spatial light modulators (Micro mirror array (MMA) and liquid crystal on silicon display (LCoS)) are indicated. Drawing by Josef Wenisch (In-Vision, Austria).

setup-photo-blueprint)?

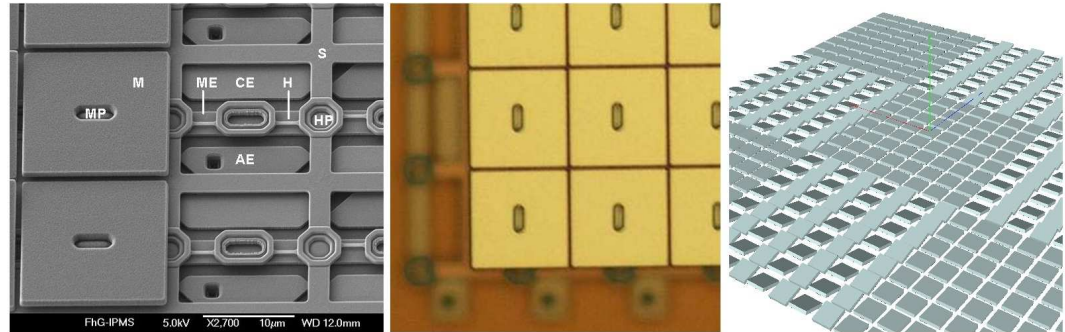


Figure 3.5.: **left:** Scanning electron microscope image of the micro-mirror array (MMA). The pixel pitch of the device is 0.016 mm. The hinges for the tilt movement and the electrodes are clearly visible. **middle:** Optical reflective microscope image of the MMA. **right:** exaggerated rendering of how a 8x8 checker board pattern would be displayed on the device. Electron and optical micrograph by Fraunhofer IPMS Dresden (Germany)

(fig:mmma)

677 3.3. Electronics for synchronization

678 Both spatial light modulators can run at most with 50% duty cycle. Therefor it
 679 is necessary to synchronize the displays. Their controllers allow to upload several
 680 hundred frames of image data before an experiment and keep them in local storage.
 681 Images can then be selected by fast function calls over USB (LCoS) or ethernet
 682 (MMA).

683 The camera (Andor Clara) as the slowest device is chosen as the master. The

3. A prototype for spatio-angular illumination

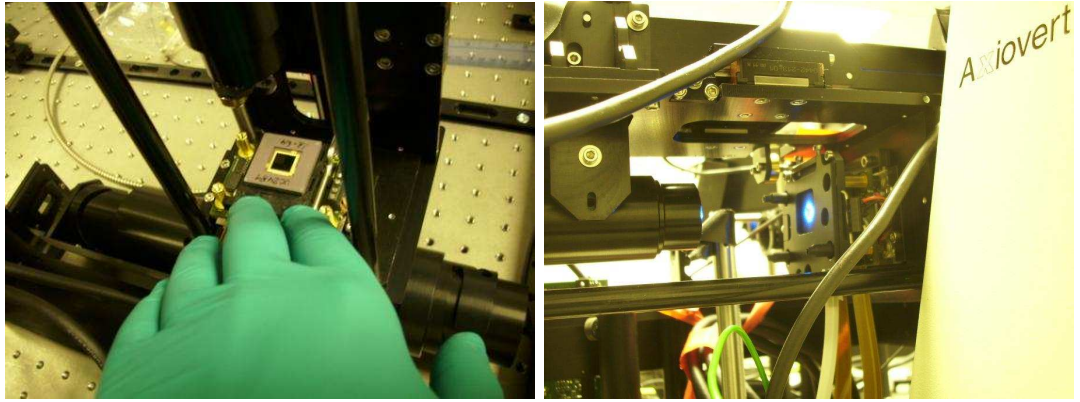


Figure 3.6.: **left:** Micro mirror array chip during installation of the optics. **right:** Illuminated micro mirror array in the aligned system.

`(fig:mma-closeup)`



Figure 3.7.: Images of the micro mirror array in the back focal plane with different settings of the variable tube lens. The micro mirror array displays the same image (a disk) in both cases.

`(fig:tubelens-bfp)`

684 camera provides two TTL outputs. The output “fire” is high while the camera is
 685 integrating. The output “shutter” goes high 1 ms before “fire” and provides enough
 686 time ($> 850 \mu\text{s}$) for the MMA controller to tilt and let the mirrors settle.

687 The LCoS controller can only be programmed to a limited number of discrete
 688 image times (20 ms, 10 ms, 5 ms, 200 μs) and it is not straight forward to change
 689 this via USB interface. Therefor we always work with a fixed integration time of
 690 20 ms. The “fire” output of the camera also switches the laser on using an acousto
 691 optic modulator (AOM).

692 When the z-stage is used, the camera is stopped until the stage has reached its
 693 target position.

3. A prototype for spatio-angular illumination



Figure 3.8.: The black cylinder on the left is the variable tube lens. Behind this is the polarizing beam splitter and the ferroelectric liquid crystal on silicon display.

`{fig:lcos}`

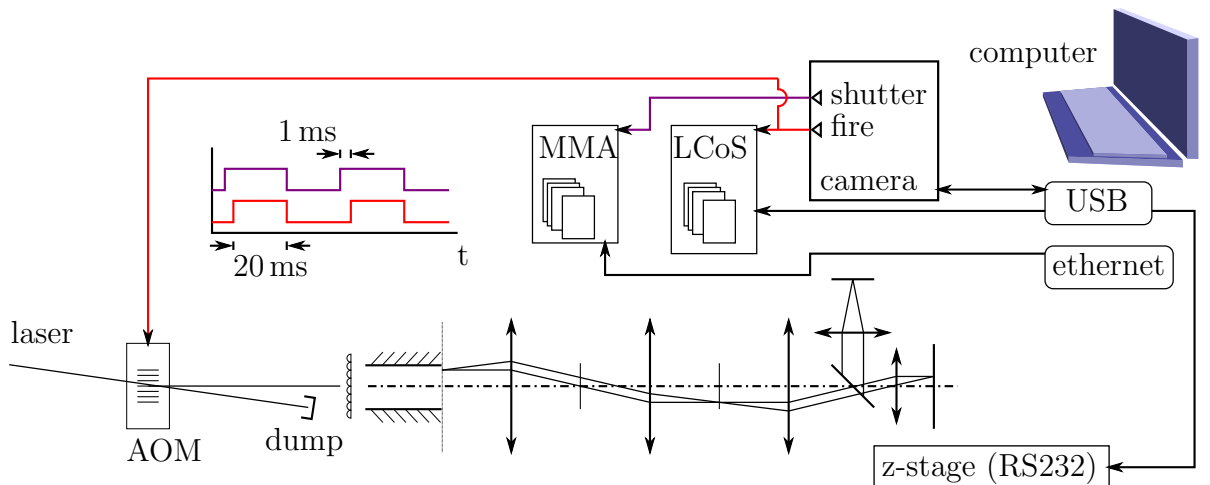


Figure 3.9.: The camera triggers both spatial light modulators with its TTL outputs. The acousto optic modulator sends light into the system during camera integration.

`fig:memi-electronics)?`

694 3.4. Alignment of the displays

695 In order to be able to predict which position on the camera will be illuminated by
 696 a particular pixel of the LCoS a calibration procedure is run. For this a fluorescent
 697 plane is selected as a specimen. Then single spots are scanned for a grid of 10×10
 698 positions over the LCoS. The resulting spots on the camera are located and four
 699 parameters defining the rigid transform between camera and LCoS are estimated
 700 (scale, rotation angle, translation in x and y, see Appendix C).

3. A prototype for spatio-angular illumination

701 Using these parameters one can then convert between camera and LCoS coordi-
702 nates (see Figure 3.10). Changing the focal length of the illumination tubelens or
703 a change on the camera position generally requires a new calibration.

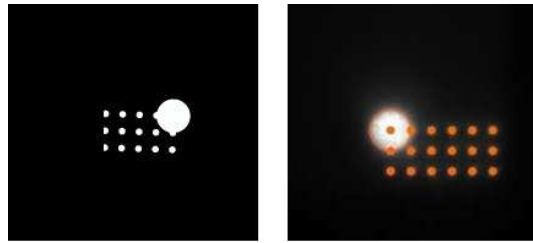


Figure 3.10.: **left:** Mask that is displayed on the LCoS. **right:** Camera image of fluorescent plane illuminated by mask. The orange lines indicate the borders of the original pattern.

fig:screen_lcos-calib)

704 The MMA is aligned by displaying an annular ring on the MMA and matching
705 it to the ring of a phase objective.

706 3.5. Ray-based illumination optimization

707 In order to make use of the spatio-angular illumination system it is necessary to
708 produce masks for the two spatial light modulators, that will reduce unnecessary
709 illumination in the sample.

710 3.5.1. Index matched sphere model

711 One useful simple model are spheres. They can model fluorescent beads or nuclei
712 in a *C. elegans* embryo. Figure 3.11 displays a model of a *C. elegans* embryo,
713 constructed from 3D data of a confocal microscope. The nuclei are relatively sparse.
714 In order to illuminate one or a few nuclei we might be able to find a path for the
715 excitation light that doesn't intersect out of focus nuclei – or at least avoids them.
716 In our spatio-angular microscope the illumination pattern is represented by two
717 masks. One for the LCoS and another one for the MMA. In the following we will
718 construct an algorithm to find such optimized illumination patterns. For example
719 the red rectangle (with $\sim 4 \mu\text{m}$ on the side) would be selected for illumination with
720 the LCoS. The red cylinder indicates the angle that would be least obscured by out
721 of focus nuclei.

3. A prototype for spatio-angular illumination

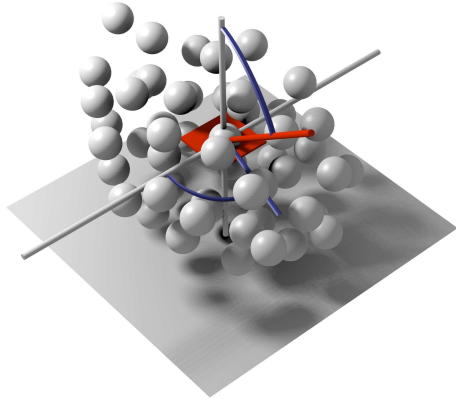


Figure 3.11.: Rendering of a sphere model, fitted to one time frame of a 3D confocal video of a developing *C. elegans* embryo (strain AZ212, data provided by Jean-Yves Tinevez (Institut Pasteur, Paris) by finding local maxima in the difference of gaussian filtered data (Santella et al. 2010).

`<fig:render>`

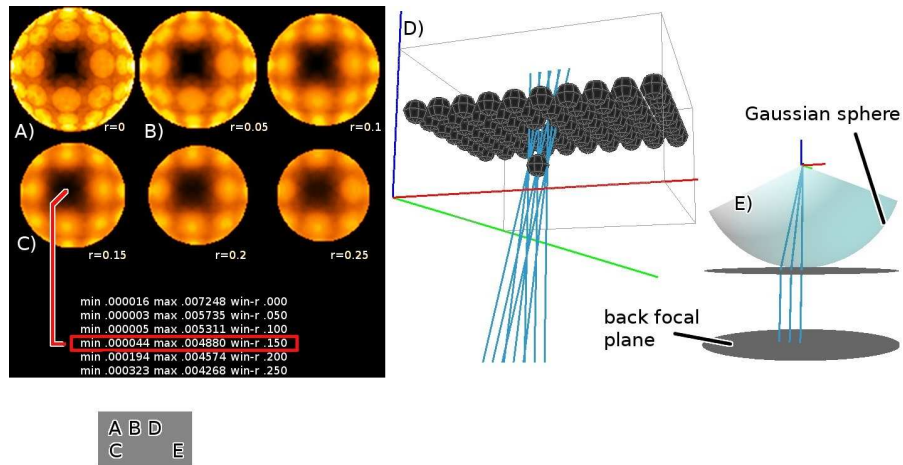


Figure 3.12.: Test case for spatio-angular illumination. A target sphere is moved out of a layer of spheres. **(a-c)** Rays from the back focal plane are traced through the target sphere and the total intersection length with out of focus spheres is plotted in the diagrams.

`_n100_3_7_5_big_label)`

722 3.5.2. Tracing in illumination direction

723 First we assume the beads are embedded in index matched medium. Then rays
 724 only refract at the gaussian sphere of the objective lens and it is insignificant how
 725 far the target bead is from the interface between coverslip and medium.

726 Initially we investigated a very simple optimization routine (see Figure 3.12). A
 727 circular window with radius r is placed into the back focal plane. Rays from the
 728 center and periphery of the window are traced through the target and into out of
 729 focus spheres. The intersection length of each ray with each sphere is summed and

3. A prototype for spatio-angular illumination

730 plotted into a diagram.

731 Figure 3.12 a) depicts the collected values for a point-like window. Figure 3.12 b)
 732 shows the same for a window with a diameter of 5% of the back focal plane. The
 733 left column in the table below the images lists the minimal values over the full
 734 back focal plane. For small windows, a few of the rays can hit the target without
 735 intersecting any other spheres. Increasing the window size blurs the features in the
 736 diagrams.

737 Here we would choose the window with $r = 0.15$ (Figure 3.12 c)). It still has a
 738 low minimum but the largest amount of light would reach the target.

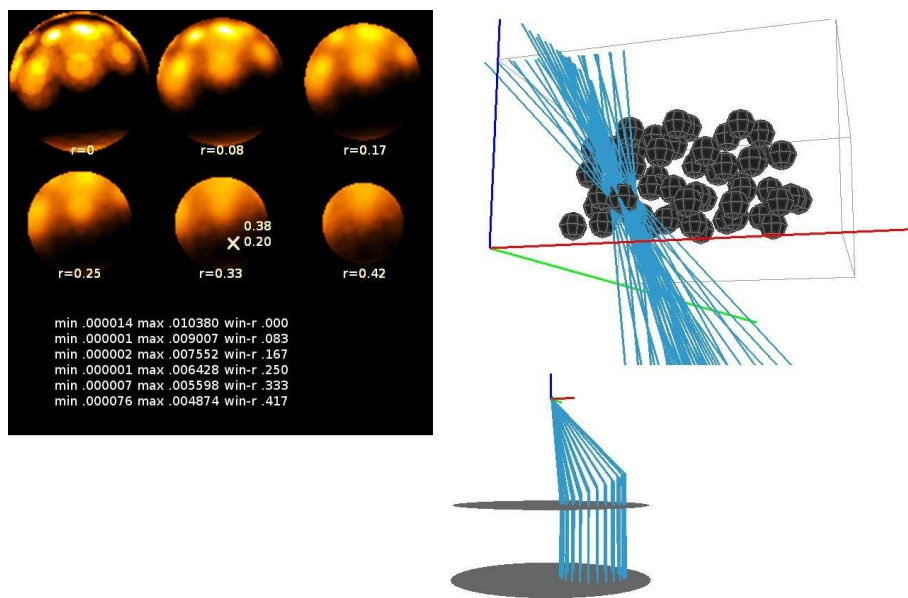


Figure 3.13.: Raytrace for circular window optimization in illumination direction.
 A window with 33% BFP diameter would be used to illuminate the target nucleus.

739 Figure 3.13 shows a similar raytrace for a sphere model of a *C. elegans* embryo
 740 and chooses a window size and position which in this sense is optimal.

741 However with the MMA we have a very versatile display and we don't have to
 742 limit ourselves to circular windows. Also the raytraced optimizations can look noisy
 743 when not enough rays are sent through the sample.

744 3.5.3. Tracing in detection direction

745 For this reason we decided to trace rays from out of focus nuclei through the target
 746 into the back focal plane.

747 Figure 3.14 C) depicts the results of tracing through a single target point and

3. A prototype for spatio-angular illumination

748 the out of focus spheres in B) in illumination direction. Note how each out of focus
749 spheres result in a deformed blob in the back focal plane.

750 It should be quite clear that the image in Figure 3.14 D) displays nearly the same
751 information but was obtained with much less computation. Here 16 rays were trace
752 (see Appendix B.7) from the periphery of each out of focus nucleus and one from
753 the center and the resulting triangle fan was rasterized into the image. We call this
754 image a shadow map.

755 In order for our spatio-angular system to work, neither the MMA, nor the LCoS
756 should displays masks with only a few white pixels. Ray based simulations are
757 not good models in this case (see Appendix E for a description of a wave optical
758 treatment) and illumination light would simply be impractically low.

759 For this reason the trace of Figure 3.14 D) is insufficient. Instead of one target
760 point a sufficiently big area in the model should be sampled. We sum each of
761 the corresponding shadow maps into a new one (see the two images on the left in
762 Figure 3.15. Then we threshold the accumulated shadow map, so that only the
763 angles with least out of focus targets are illuminated. Finally we blur the mask
764 with a gaussian filter in order to prevent ringing in sample space.

765 The diagram on the right of Figure 3.15 displays a sphere model of 3D beads
766 ($2\mu\text{m}$ diameter, yellow-green, in oil). We obtained this model with our microscope
767 by displaying several gratings on the LCoS at full angular illumination and doing a
768 structured illumination reconstruction (in each pixel the maximum of each pattern
769 minus minium of each pattern) of sectioned slices. A matching difference of gaussian
770 filter and local maximum search in the 3D volume gives the centers of the beads.

771 After constructing the model, the microscope continuously moves the z-stage onto
772 each bead and illuminates them with their optimized illumination angles. Bead 26
773 has been illuminated with very high angles in order to prevent exposure of the bunch
774 of beads further away from the objective. Bead 5 is far from any other beads and
775 therefor more angles can be used for its illumination.

776 **3.5.4. Coping with index mismatch of the embedding medium**

777 So far the described algorithms assumed ideal samples which have been embedded
778 in a medium with a refractive index, the objective was designed for.

779 Biological samples are often embedded in water. However, it might still be useful,
780 to image with an oil objective. Then the additional refraction at the glass–water
781 interface has to be taken into account for spatio-angular illumination.

782 This makes the task of predicting where to mask the MMA in order to protect

3. A prototype for spatio-angular illumination

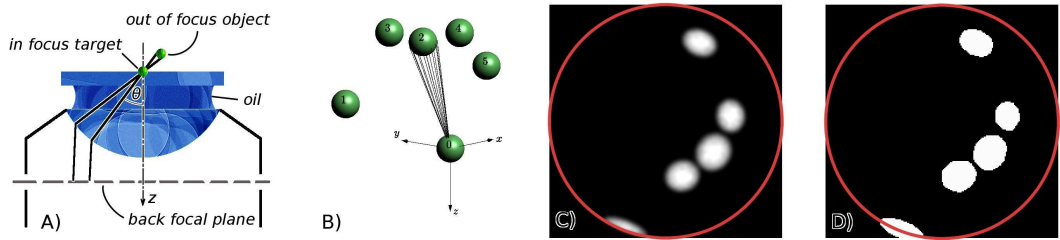


Figure 3.14.: **A)** Schematic of the rays between back focal plane and sample. **B)** Out of focus spheres and the target point define a double cone of rays that should not be illuminated. **C)** Tracing rays in illumination direction from the back focal plane through the sample is an expensive operation and results in unnecessarily exact results. **D)** Tracing in detection direction from the periphery of out of focus spheres through a target point into the back focal plane gives nearly identical results (shadow map) and is more computationally efficient.

`<fig:img2-montage_hor>`

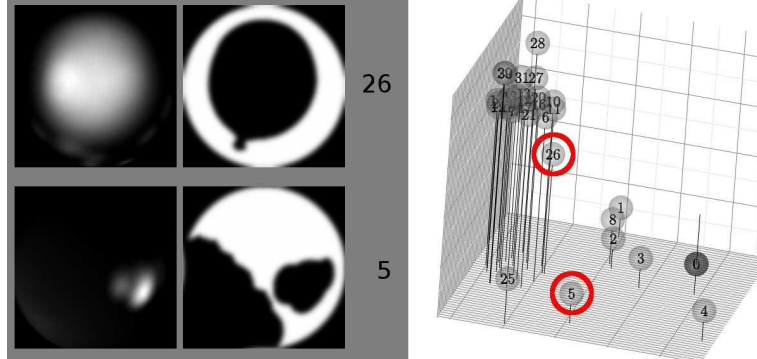


Figure 3.15.: **right:** Sphere model of a sample with 3D beads. **left:** Optimized MMA masks to illuminate bead 26 or bead 5.

783 out of focus beads more complicated. To circumvent the spherical aberrations, we
 784 have to limit the range of angles, that are simultaneously illuminating and shift
 785 the illumination spot on the LCoS to correct for the transversal focus shift (q in
 786 Figure 3.16 right). For this we must have a good estimate of the distance of the
 787 sample from the coverslip–water interface. See Appendix B for a description of the
 788 raytrace algorithm.

789 Using an oil immersion objective has the following advantage: By sending the
 790 illumination rays into the sample at a steep angle, close to the TIRF angle, we can
 791 generate a thin sheet of light (see Figure 2.3).

3. A prototype for spatio-angular illumination

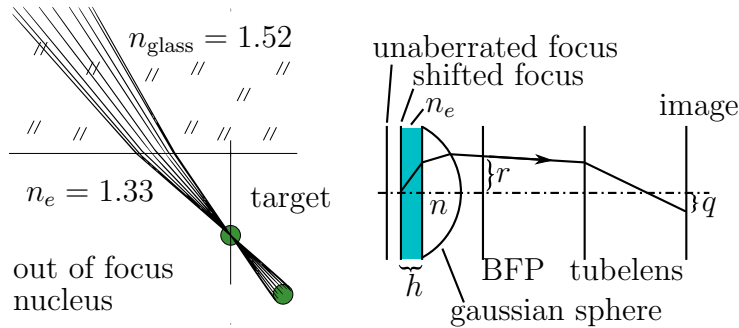


Figure 3.16.: **left:** Rays are starting from periphery of out-of-focus nucleus, hitting the target and refracted at the water–coverslip interface. **right:** Due to spherical aberrations, rays from an on-axis point are shifted to $q(r)$ on the camera (where r relates to the angle of the ray in the sample).

fig:aberration-sketch)

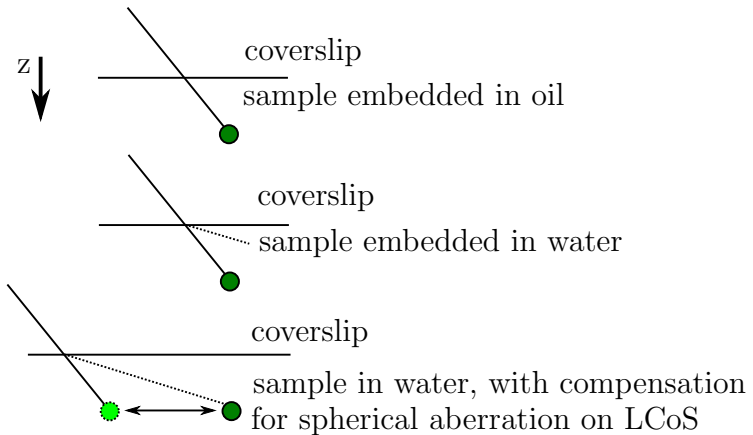


Figure 3.17.: **top:** A straight ray illuminates a bead embedded in oil. **middle:** Embedding the sample in water results in refraction of the ray. **bottom:** The refraction can be compensated by shifting the target area on the LCoS.

fig:shift-correction)?



Figure 3.18.: Raytracing through an objective followed by a tubelens. The focal length of the tubelens in this simulation is 16 mm (as opposed to the usual 160 mm) so that the plot fits into an unscaled image. The water depth is 10 μm . Rays that start in the sample with high angles do not reach the gaussian focus spot in the image.

scope-aberrate-front)?

4. Description of experiments

793 4.1. Measure acceptance angle

794 As a general verification of the system and a second verify the alignment of the
795 MMA on the back focal plane of the objective lens, we imaged three fluorescent
796 plane samples with various embedding indices.

797 The illumination in the sample is a disk of $30\text{ }\mu\text{m}$ diameter, spanning nearly the
798 full field. Then a window of 15×15 pixels was scanned over the MMA and for each
799 position, a camera image was captured. Figure 4.2 displays the integrated intensity
800 in each image for each of the positions on the back focal plane.

801 The left diagram shows an image of the pupil of the objective. Rays in the
802 edges of the MMA are absorbed by the pupil aperture in the objective and therefore
803 dark. The next two images show the reduced acceptance angle due to lower index
804 embedding medium. Rays on the border of the pupil traverse the objective but are
805 reflected at the coverslip–embedding interface.

806 4.2. Spatio-angular illumination of beads

807 Here we describe the experiment that generated the data in Figure 3.15. The system
808 configuration is described in Appendix G.2. The LCoS controller is connected to
809 the graphics card. The camera exposure is fixed to 16 ms. The MMA mirrors are
810 deflected during the integration time. Between image changes on LCoS and MMA
811 the system was given several frames in order to prevent exposures with the wrong
812 MMA or LCoS masks (see Figure G.5).

4. Description of experiments

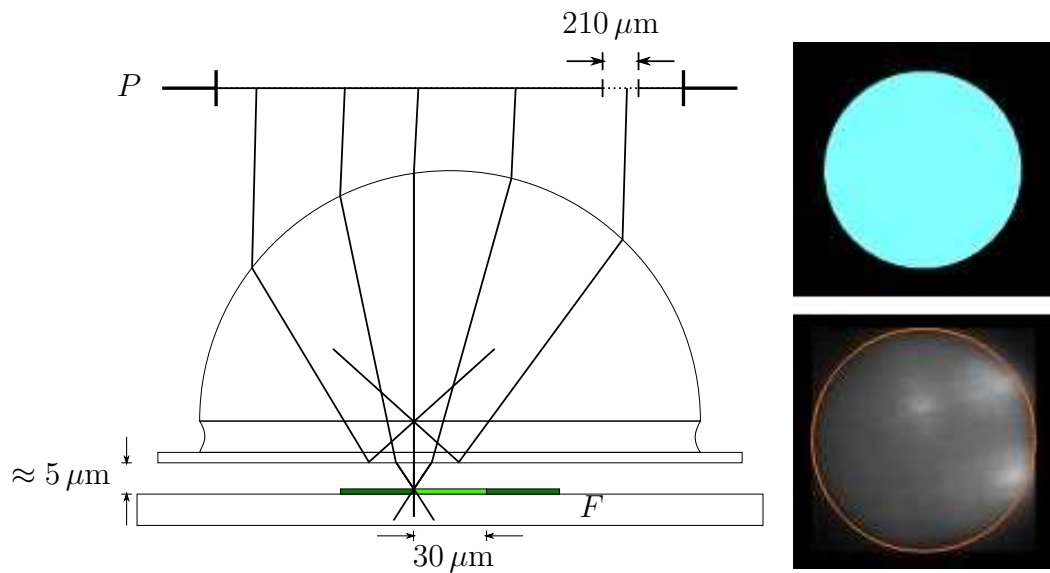


Figure 4.1.: A fluorescent plane on a slide is embedded in oil, water or air. The thickness of the embedding medium is approximately $5 \mu\text{m}$. The LCoS illuminates a disk with $30 \mu\text{m}$ diameter while a 15×15 window is scanned over the MMA. **right top:** LCoS mask. **right bottom:** Typical camera image.

?<fig:tirf-exp>

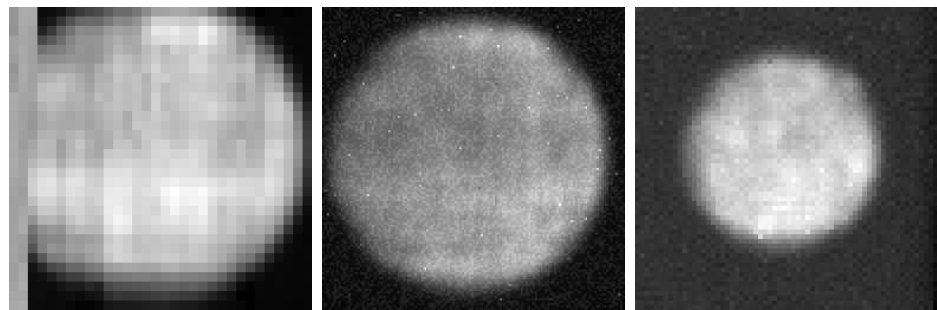


Figure 4.2.: Integrated image intensities for different illumination window positions in the back focal plane. Embedding media: **left:** Oil $n = 1.52$, **middle:** water $n = 1.33$, **right:** air $n = 1$.

?<fig:immersion-bfp-scan>

813 A. Read noise characterization of 814 cameras

815 ⟨sec:ccd-meas⟩ We describe a method to measure the read noise of a camera and compare
816 the performance of three EM-CCDs.

817 A.1. Introduction

818 In order to characterize a camera we captured sequences of images that contain a light pattern as in Figure A.1. The pattern is smooth and non-uniform. The

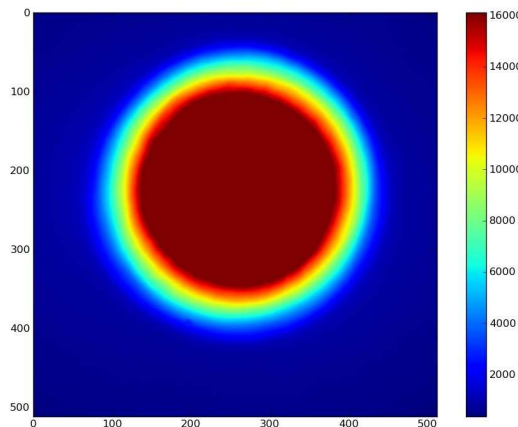


Figure A.1.: Image of a defocused area on a fluorescent plane sample. A couple of such images (> 20) are captured and variance in each pixel is plotted against the intensity to find the correspondence between reported ADU and detected photoelectrons.

819 ⟨fig:calib-pic⟩
820 images were produced in a fluorescence microscope. The light source is a DPSS
821 laser with 473 nm wavelength. It illuminates a circular area of the sample. The
822 sample is a fluorescent plane. A FITC filter cube and a 10× objective were used.
823 The sample was adjusted to be slightly out of focus in order to obtain a smooth
824 intensity gradient in the image.

A. Read noise characterization of cameras

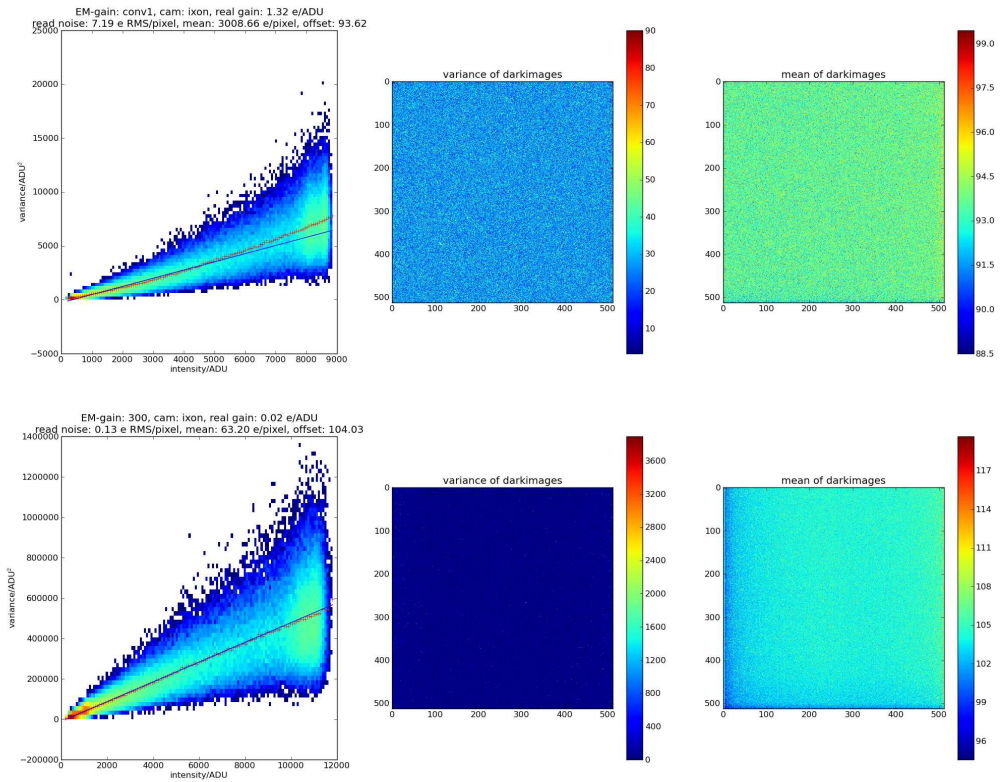


Figure A.2.: **top:** Conventional read out of an Andor IXon3 camera. **bottom:** Read out with an EM-gain setting of 300 on the same camera with identical sample. **left:** 2D histogram of per pixel variances against binned intensities. **middle:** variance of 20 dark images. **right:** mean of 20 dark images.

`(fig:ixon)`

825 The light source is stable and the relative standard deviation of the illumination
826 intensity is typically $< 0.2\%$ for the calibration time.

827 A sequence (20) of such images can be used to determine the mapping between
828 analog-to-digital units (ADU) and the number of detected photoelectrons. This
829 method is based on the known relation between the mean number of Poisson dis-
830 tributed photons and its variance.

831 For the calibration a 2D histogram of the per pixel variance image and the per
832 pixel mean of the image stack is plotted. Then the slope of the resulting point cloud
833 is determined.

834 A.2. Calibration of an Andor IXon3 camera

835 In the top left diagram of Figure A.2 contains such a 2D histogram. It was obtained
836 for conventional readout at 3 MHz in our Andor IXon3 camera (head: DU-897D-

A. Read noise characterization of cameras

837 CS0-#BV). The variances are collected in 64 intensity bins and their averages are
838 plotted as red crosses. The blue line is the result of a linear fit to the first 60%
839 of the red crosses. Its slope gives the real gain of the camera that can be used to
840 convert ADU into photoelectrons (here $1.32\text{ e}/\text{ADU}$).

841 The following figures show corresponding measurements using the EM readout
842 mode with varying EM gain. It is followed by one last measurement with conven-
843 tional readout to verify, that the fluorophores didn't bleach too much during the
844 experiment.

845 The camera was cooled to $-75\text{ }^{\circ}\text{C}$. In order to prevent overexposure of the sensor
846 an image with a short 10 ms integration time was acquired and the integration time
847 for the experiment was set such that a maximum of 10000 ADU would occur. An
848 internal shutter in the camera was closed to obtain the dark images. The process
849 was automated using an Andor Solis Basic program which is listed below.

850 The square root of the mean of the variance of the dark images was converted
851 into a read noise in electrons per pixel using the real gain.

852 The table in Figure A.3 summarizes the calibration results. The read noise in
853 conventional mode is approximately 8 electrons per pixel rms. The column **mean'**
854 contains the average number of photoelectrons per pixel in the illuminated image
855 normalized by the integration time. The rows **conv1** and **conv2** with conventional
856 read out (without EM-gain) contain approximately the same number. This proves
857 that no significant bleaching occurred during the experiment.

858 The EM gain process introduces multiplicative noise in the signal that has the
859 same effect on the photoelectron statistics as lowering the quantum efficiency of the
860 sensor. Dividing values of the column **mean'** from EM readouts by the same value
861 from the conventional readout gives the *excess noise factor*. Its value is smaller
862 than one and describes the apparent reduction of the quantum efficiency.

863 Due to a bug in the capturing process the images in the second row (for EM-
864 gain 40) was overexposed and the data shouldn't be used. Also the last experiment
865 **conv2** with conventional read out reports a larger gain of $1.6\text{ e}/\text{ADU}$ than the first
866 experiment **conv1** with gain $1.3\text{ e}/\text{ADU}$. Later we learned that one should allow
867 several seconds of settling time, when changing the EM-gain voltage. This might
868 explain the difference in gains, even though one would think that the conventional
869 read out should be decoupled.

870 **A.2.1. Andor Basic code listing for automatic image acquisition**

```
871 function ~GetSaturatingExposure()
```

get
this
right:
should
be
 $\sqrt{2}$

A. Read noise characterization of cameras

ixon3	gain	noise	mean	offset	exp time	mean'	excess	
	[e/ADU]	[e/px]	[e/px]	[ADU]	[s]	[e/(px s)]		15209
conv1	1.32	7.19	3008.66	93.62	0.20161	14923	0.98	
40	0.13	0.54	1018.25	102.95	0.35714	2851	0.19	
50	0.12	0.49	260.05	103.23	0.02891	8995	0.59	
60	0.10	0.41	225.46	103.26	0.02490	9054	0.60	
70	0.08	0.35	190.52	103.49	0.02121	8983	0.59	
80	0.07	0.31	165.24	103.17	0.01855	8907	0.59	
90	0.07	0.29	150.54	103.34	0.01607	9368	0.62	
100	0.06	0.26	128.47	103.35	0.01363	9427	0.62	
110	0.05	0.24	121.11	103.73	0.01287	9409	0.62	
120	0.05	0.23	113.71	103.50	0.01197	9498	0.62	
130	0.05	0.21	106.66	103.63	0.01118	9541	0.63	
140	0.04	0.20	96.95	103.77	0.01014	9564	0.63	
150	0.04	0.19	89.68	103.79	0.00927	9671	0.64	
160	0.04	0.18	87.24	103.87	0.00904	9656	0.63	
170	0.04	0.18	81.56	104.17	0.00837	9739	0.64	
180	0.03	0.17	79.80	104.00	0.00809	9863	0.65	
190	0.03	0.16	74.00	104.26	0.00755	9806	0.64	
200	0.03	0.16	72.57	104.03	0.00735	9878	0.65	
210	0.03	0.15	69.44	104.22	0.00698	9944	0.65	
220	0.03	0.15	67.69	104.08	0.00679	9971	0.66	
230	0.03	0.15	65.63	104.03	0.00653	10057	0.66	
240	0.03	0.19	63.90	104.05	0.00631	10131	0.67	
250	0.02	0.14	62.52	104.15	0.00624	10026	0.66	
260	0.02	0.14	62.86	104.18	0.00624	10078	0.66	
270	0.02	0.14	63.17	103.94	0.00624	10130	0.67	
280	0.02	0.13	63.64	104.21	0.00624	10204	0.67	
290	0.02	0.13	63.38	104.15	0.00624	10162	0.67	
300	0.02	0.13	63.20	104.03	0.00624	10133	0.67	
conv2	1.60	8.77	8198.86	93.30	0.52910	15496	1.02	

Figure A.3.: Comparison of read noise for different EM-gain settings (first column) of the Andor IXon3. The value **mean'** estimates the number of photo electrons the detector would have seen with 1s integration time and is used to calculate the excess noise factor in the last column. The images for the red row (EM-gain 40) were overexposed and the data are not correct. In EM-mode the fastest read out speed was used 10 MHz with vertical shift speed of 1.7 us.

{fig:ixon-table}

A. Read noise characterization of cameras

```
872     SetKineticNumber(1)
873     exp=.01
874     SetExposureTime(exp)
875     run()
876     m=maximum(#0,1,512)
877     GetSaturatingExposure=exp*10000/(m-100)
878     CloseWindow(#0)
879     return
880 name$ = "C:\Users\work\Desktop\martin\20111111\scan-em3\ixon_"
881 print("start")
882
883 SetOutputAmp(1)
884 print("conv_start")
885 exp= ~GetSaturatingExposure()
886 print(exp)
887 SetExposureTime(exp)
888 SetKineticNumber(20)
889 SetShutter(0,1)
890 run()
891 save(#0,name$ + "conv1_dark.sif")
892 ExportTiff(#0, name$ + "conv1_dark.tif", 1, 1, 0, 0)
893 CloseWindow(#0)
894 CloseWindow(#1)
895
896 SetShutter(1,1)
897 run()
898 save(#0,name$ + "conv1_bright.sif")
899 ExportTiff(#0, name$ + "conv1_bright.tif", 1, 1, 0, 0)
900 CloseWindow(#0)
901 CloseWindow(#1)
902
903 SetOutputAmp(0)
904 SetShutter(1,1)
905 for i = 40 to 300 step 10
906     SetGain(i)
907     exp=~GetSaturatingExposure()
908     print(exp)
909     SetExposureTime(exp)
910     SetKineticNumber(20)
```

A. Read noise characterization of cameras

```
911     SetShutter(0,1)
912     run()
913     save(#0,name$ + str$(i) + "_dark.sif")
914     ExportTiff(#0, name$ + str$(i) + "_dark.tif", 1, 1, 0, 0)
915     CloseWindow(#0)
916     CloseWindow(#1)
917     SetShutter(1,1)
918     run()
919     save(#0,name$ + str$(i) + "_bright.sif")
920     ExportTiff(#0, name$ + str$(i) + "_bright.tif", 1, 1, 0, 0)
921     CloseWindow(#0)
922     CloseWindow(#1)
923 next
924
925 SetOutputAmp(1)
926 print("conv_end")
927 exp= ~GetSaturatingExposure()
928 print(exp)
929 SetExposureTime(exp)
930 SetKineticNumber(20)
931 SetShutter(0,1)
932 run()
933 save(#0,name$ + "conv2_dark.sif")
934 ExportTiff(#0, name$ + "conv2_dark.tif", 1, 1, 0, 0)
935 CloseWindow(#0)
936 CloseWindow(#1)
937
938 SetShutter(1,1)
939 run()
940 save(#0,name$ + "conv2_bright.sif")
941 ExportTiff(#0, name$ + "conv2_bright.tif", 1, 1, 0, 0)
942 CloseWindow(#0)
943 CloseWindow(#1)
```

944 **A.2.2. Python code listing for the read noise evaluation**

```
945 #!/usr/bin/env python
946 # ./ti.py /media/backup/andor-ultra-ixon/martin/20111111/scan-em3/ ultra 2700
947 import sys
```

A. Read noise characterization of cameras

```
948 import os
949
950 import matplotlib
951 matplotlib.use('Agg')
952
953 from pylab import *
954 from libtiff import TIFFfile, TIFFimage
955 from scipy import stats
956
957 seterr(divide='ignore')
958
959 folder = sys.argv[1]
960 cam = sys.argv[2]
961 gain = sys.argv[3]
962
963 def readpics(gain, cam='ixon_', isdark=False):
964     print 'loading ', os.path.join(folder, cam) + '_' + gain + '_bright.tif'
965     fg=TIFFfile(os.path.join(folder, cam) + '_' + gain + '_bright.tif')
966     bright,bright_names=fg.get_samples()
967     bg=TIFFfile(os.path.join(folder, cam) + '_' + gain + '_dark.tif')
968     dark,dark_names=bg.get_samples()
969     return (bright[0],dark[0])
970
971 (f,b) = readpics(gain=gain, cam=cam)
972
973 bg=mean(b, axis=0)
974 v=var(f, axis=0)
975 i=mean(f, axis=0)
976
977 ny,nx=64,128
978 H,y,x=histogram2d(v.flatten(), i.flatten(), bins=[ny,nx],
979                      range=[[0,v.max()], [0,i.max()]]))
980 extent = [x[0], x[-1], y[0], y[-1]]
981 acc=zeros(x.shape, dtype=float64)
982 accn=zeros(x.shape, dtype=int64)
983 s=nx/i.max()
984 for ii, vv in nditer([i, v]):
985     p=round(ii*s)
986     acc[p]+=vv
```

A. Read noise characterization of cameras

```
987     accn[p] +=1
988
989 fig=figure(figsize=(24, 8),dpi=300)
990 hold(False)
991 title('bal')
992 subplot(1,3,1)
993 imshow(log(H), extent=extent,
994         aspect='auto', interpolation='none',origin='lower')
995 hold(True)
996 ax=x[nonzero(accn)]
997 ay=acc/accn
998 ay=ay[nonzero(accn)]
999 l=round(.6*len(ax))
1000 bx=ax[0:l]
1001 by=ay[0:l]
1002 plot(ax,ay,'r+')
1003 slope,intercept,rval,pval,stderr=stats.linregress(bx,by)
1004 plot(ax,polyval([slope,intercept],ax))
1005 xlabel('intensity/ADU')
1006 ylabel(r'variance/ADU$^2$')
1007 real_gain=1/slope # unit electrons/ADU
1008 read_noise=sqrt(var(b))*real_gain # electrons RMS per pixel
1009 mean_elecs=(mean(f)-mean(b))*real_gain # photoelectrons electrons per pixel
1010 print gain,cam,real_gain,read_noise,mean_elecs,mean(b),rval,pval,stderr
1011 tit='EM-gain: %s, cam: %s, real gain: %.2f e/ADU\n'
1012 read noise: %.2f e RMS/pixel, mean: %.2f e/pixel, offset: %.2f'
1013 % (gain,cam,real_gain,read_noise,mean_elecs,mean(b))
1014 title(tit)
1015 subplot(1,3,2)
1016 imshow(var(b,axis=0))
1017 title('variance of darkimages')
1018 colorbar()
1019 subplot(1,3,3)
1020 imshow(mean(b,axis=0))
1021 title('mean of darkimages')
1022 colorbar()
1023 show()
1024 fig.savefig(cam+'_'+gain+'.png')
```

A. Read noise characterization of cameras

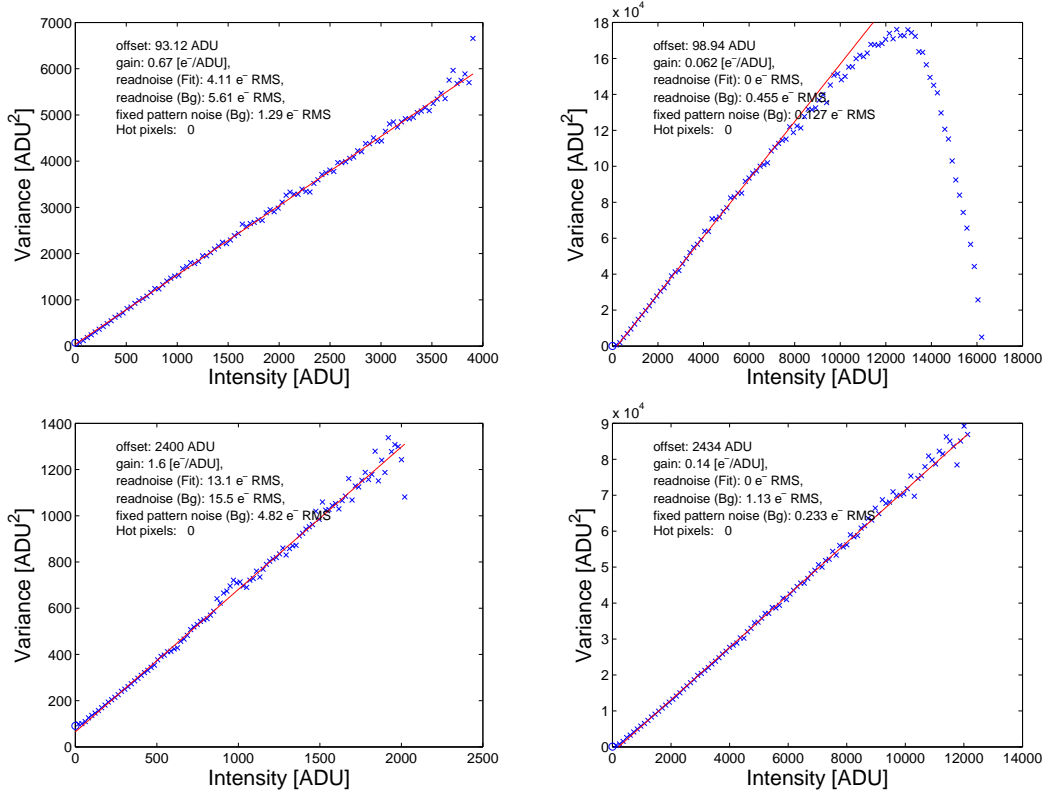


Figure A.4.: **top:** Andor IXon2 **left:** Normal read out with preamp 5. **top right:** EM-gain 100 preamp 5. **bottom:** Cascade II **left:** Normal read out $\text{mean} = 254.82 \text{ e}/\text{px}$. **right:** EM-gain 3000, $\text{mean} = 122.08 \text{ e}/\text{px}$, therefore the excess noise factor is 0.48.

`(fig:old-cams)`

1025 A.3. Comparison with other cameras

1026 In order to compare different EM-CCD cameras one must first convert the EM-gain
 1027 register setting into the real EM-gain as cameras are often not calibrated to have
 1028 a linear gain curve and the multiplicative gain changes with temperature and live
 1029 time of the sensor.

1030 Figure A.4 shows some calibrations on older cameras (Andor IXon2 (head: DU-
 1031 897E-CS0-#BV, sensor: E2V Tech CCD97 512 × 512, pixel pitch 16 μm, cooled to
 1032 -70°C) and Photometrics Cascade II (sensor: e2v CCD97, 512 × 512, pixel pitch
 1033 16 μm, cooled to -70°C) which have been done using the DIPimage function cal-
 1034 readnoise. The real gain of the Andor IXon2 is 0.67/0.062 = 10.8 and it has 0.46 e
 1035 rms/px readnoise. The real gain of the Cascade II is 1.6/0.14 = 11.4 with 1.13 e
 1036 rms/px read noise. Approximately the same real gain is obtained with the IXon3
 1037 at EM-gain 50: 1.32/0.12 = 11.0 with a read noise of 0.49 e rms/px. So the two
 1038 Andor cameras show the same performance.

¹⁰³⁹ **B. Raytracing for spatio-angular** ¹⁰⁴⁰ **microscopy**

¹⁰⁴¹ `<sec:raytrace>` Here we give an overview of some useful equations for raytracing through lens mod-
¹⁰⁴² els. The design parameters of our microscope objectives are not usually known to us.
¹⁰⁴³ However, this is not an insurmountable problem as they can be represented using a
¹⁰⁴⁴ simplified model (Hwang and Lee 2008). We use this to simulate the refraction at
¹⁰⁴⁵ the coverslip–medium interface for non-index matched media.

¹⁰⁴⁶ **B.1. Refraction at plane surface**

We begin by describing refraction at a plane surface¹. The wavelength of the light defines the length of the wave vector \mathbf{k}_0 . The lengths of the incident and transmitted wave vectors \mathbf{k}_1 and \mathbf{k}_2 are given by the refractive index in their respective half space:

$$k_0 = 2\pi/\lambda \tag{B.1} \{ ? \}$$

$$k_1 = n_1 k_0 \tag{B.2} \{ ? \}$$

$$k_2 = n_2 k_0. \tag{B.3} \{ ? \}$$

The normal $\hat{\mathbf{n}}$ is directed in the opposite direction of the incident wave vector \mathbf{k}_1 . We define the transversal and normal component vectors:

$$\mathbf{k}_{1n} = (\mathbf{k}_1 \hat{\mathbf{n}}) \hat{\mathbf{n}} \tag{B.4} \{ ? \}$$

$$\mathbf{k}_{1t} = \mathbf{k}_1 - \mathbf{k}_{1n}. \tag{B.5} \{ ? \}$$

¹The equations are as in (McClain et al. 1993).

B. Raytracing for spatio-angular microscopy

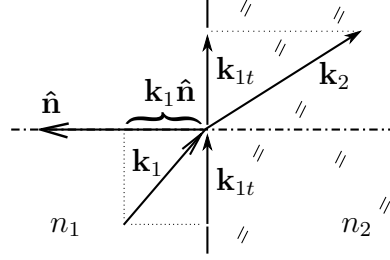


Figure B.1.: Refraction at an interface transforms the incident wave vector \mathbf{k}_1 into the outgoing wave vector \mathbf{k}_2 .

Both of these components are perpendicular and during refraction the transversal component of the wave vector is invariant:

$$k_2^2 = k_{2n}^2 + k_{2t}^2 \quad (\text{B.6}) \{?\}$$

$$\mathbf{k}_{2t} = \mathbf{k}_{1t}. \quad (\text{B.7}) \{?\}$$

Using the two equations from above we can calculate the length of the normal component of the transmitted wave vector \mathbf{k}_2 :

$$k_2^2 = k_{2n}^2 + (\mathbf{k}_1 - \mathbf{k}_{1n})^2 \quad (\text{B.8}) \{?\}$$

$$k_{2n}^2 = k_2^2 - (\mathbf{k}_1 - (\mathbf{k}_1 \hat{\mathbf{n}}) \hat{\mathbf{n}})^2 \quad (\text{B.9}) \{?\}$$

$$= k_2^2 - (k_1^2 - 2(\mathbf{k}_1 \hat{\mathbf{n}})^2 + (\mathbf{k}_1 \hat{\mathbf{n}})^2) \quad (\text{B.10}) \{?\}$$

$$= k_2^2 - k_1^2 + (\mathbf{k}_1 \hat{\mathbf{n}})^2. \quad (\text{B.11}) \{?\}$$

Finally we can express the full transmitted wave vector \mathbf{k}_2 using only known quantities:

$$\mathbf{k}_2 = \mathbf{k}_{1t} - \sqrt{k_2^2 - k_1^2 + (\mathbf{k}_1 \hat{\mathbf{n}})^2} \hat{\mathbf{n}} \quad (\text{B.12}) \{?\}$$

$$= \mathbf{k}_1 - (\mathbf{k}_1 \hat{\mathbf{n}}) \hat{\mathbf{n}} - \sqrt{k_2^2 - k_1^2 + (\mathbf{k}_1 \hat{\mathbf{n}})^2} \hat{\mathbf{n}}. \quad (\text{B.13}) \{?\}$$

We divide by k_2 with $\mathbf{k}_2/k_2 = \hat{\mathbf{t}}$ and $\mathbf{k}_1/k_2 = \eta \hat{\mathbf{i}}$ in order to introduce unit direction vectors $\hat{\mathbf{i}}$ and $\hat{\mathbf{t}}$ for incident and outgoing light. The relative index change across the interface is $\eta = n_1/n_2$.

$$\hat{\mathbf{t}} = \eta \hat{\mathbf{i}} - \eta (\hat{\mathbf{i}} \hat{\mathbf{n}}) \hat{\mathbf{n}} - \sqrt{1 - \eta^2 + \eta^2 (\hat{\mathbf{i}} \hat{\mathbf{n}})^2} \hat{\mathbf{n}} \quad (\text{B.14}) \{?\}$$

$$= \boxed{\eta \hat{\mathbf{i}} - \left(\eta \hat{\mathbf{i}} \hat{\mathbf{n}} + \sqrt{1 - \eta^2 (1 - (\hat{\mathbf{i}} \hat{\mathbf{n}})^2)} \right) \hat{\mathbf{n}}} \quad (\text{B.15}) \{?\}$$

B. Raytracing for spatio-angular microscopy

When the radical in the square root is negative a reflection occurs instead (TIRF). The tangential component is invariant and normal component inverts the sign:

$$\mathbf{k}_2 = \mathbf{k}_{1t} - \mathbf{k}_{1n} \quad (\text{B.16}) \{?\}$$

$$= \mathbf{k}_1 - 2\mathbf{k}_{1n} \quad (\text{B.17}) \{?\}$$

$$= \mathbf{k}_1 - 2(\mathbf{k}_1 \hat{\mathbf{n}}) \hat{\mathbf{n}} \quad (\text{B.18}) \{?\}$$

$$\hat{\mathbf{t}} = \boxed{\hat{\mathbf{i}} - 2(\hat{\mathbf{i}} \hat{\mathbf{n}}) \hat{\mathbf{n}}} \quad (\text{B.19}) \{?\}$$

1047 B.2. Intersection of a ray and a plane

Let a ray start at a point \mathbf{s} with direction $\hat{\mathbf{d}}$. A plane (defined by a point \mathbf{c} and the normal $\hat{\mathbf{n}}$) intersects this ray if normal and ray direction are not perpendicular: $\hat{\mathbf{n}} \hat{\mathbf{d}} \neq 0$. The distance between the plane and the origin is $h = \mathbf{c} \hat{\mathbf{n}}$. We can define the plane equation in Hesse normal form:

$$\mathbf{r} \hat{\mathbf{n}} = h \quad (\text{B.20}) \{?\}$$

We replace the coordinate \mathbf{r} with the ray equation and solve for the parameter τ :

$$(\mathbf{s} + \tau \hat{\mathbf{d}}) \hat{\mathbf{n}} = h \quad (\text{B.21}) \{?\}$$

$$\mathbf{s} \hat{\mathbf{n}} + \tau \hat{\mathbf{d}} \hat{\mathbf{n}} = h \quad (\text{B.22}) \{?\}$$

$$\tau = \boxed{\frac{h - \mathbf{s} \hat{\mathbf{n}}}{\hat{\mathbf{d}} \hat{\mathbf{n}}}} \quad (\text{B.23}) \{?\}$$

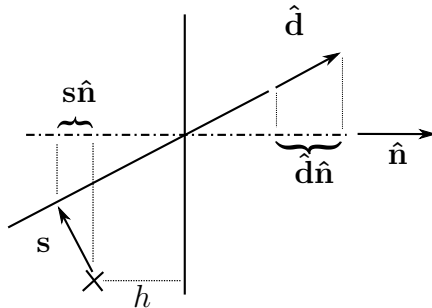


Figure B.2.: Schematic for describing the plane-ray intersection.

1048

1049 **B.3. Intersection of a ray and a sphere**

Let a ray start at a point \mathbf{s} with direction $\hat{\mathbf{d}}$. Let a sphere be centred in \mathbf{c} with radius R . Their two equations

$$(\mathbf{r} - \mathbf{c})^2 = R^2 \quad (\text{B.24}) \{?\}$$

$$\mathbf{r} = \mathbf{s} + \tau \hat{\mathbf{d}} \quad (\text{B.25}) \{?\}$$

define the intersection points. Substitution of \mathbf{r} results in a quadratic equation for τ :

$$(\mathbf{s} + \tau \hat{\mathbf{d}} - \mathbf{c})^2 = R^2 \quad (\text{B.26}) \{?\}$$

$$\mathbf{l} := [\mathbf{s} - \mathbf{c}] \quad (\text{B.27}) \{?\}$$

$$l^2 + 2\tau \mathbf{l} \hat{\mathbf{d}} + \tau^2 - R^2 = 0 \quad (\text{B.28}) \{?\}$$

$$\tau^2 + \underbrace{2\mathbf{l} \hat{\mathbf{d}}}_b \tau + \underbrace{l^2 - R^2}_c = 0 \quad (\text{B.29}) \{?\}$$

1050 **B.3.1. Solving the quadratic equation**

If the determinant d is negative the ray misses the sphere and there is no solution. If the determinant is zero the ray touches the periphery and there is only one solution. A positive determinant corresponds to two solutions. In order to prevent numerical errors the following solution should be used (Press et al. 1997):

$$d := [b^2 - 4ac] \quad (\text{B.30}) \{?\}$$

$$q := \left[\frac{-b + \sqrt{d} \operatorname{sign} b}{2} \right] \quad (\text{B.31}) \{?\}$$

$$\tau = \begin{cases} \frac{q}{a} & \text{when } |q| \approx 0 \\ \frac{c}{q} & \text{when } |a| \approx 0 \\ \left(\frac{q}{a}, \frac{c}{q} \right) & \text{else} \end{cases} \quad (\text{B.32}) \{?\}$$

1051 **B.4. Refraction on paraxial thin lens**

1052 The incident beam with direction $\hat{\mathbf{i}}$ hits the lens at the point ρ . A line parallel to
1053 $\hat{\mathbf{i}}$ through the centre of the lens defines the point on the focal plane, which will be
1054 intersected by the transmitted ray \mathbf{r} as well.

1055 The triangle ABC is similar to triangle FOA . All three angles are identical

B. Raytracing for spatio-angular microscopy

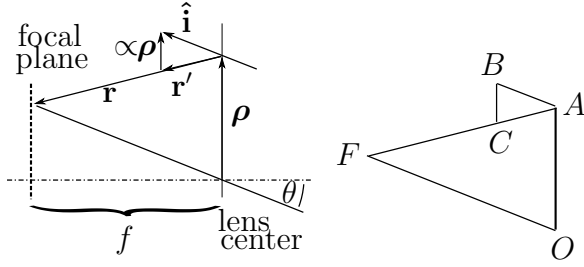


Figure B.3.: Construction of a ray on a thin lens. The incident beam with direction $\hat{\mathbf{i}}$ hits the lens at the point ρ .

1056 because each of the lines are parallel: $\overline{CB} \parallel \overline{OA} \parallel \rho$, $\overline{FA} \parallel \overline{CA}$ and $\overline{AB} \parallel \overline{OF} \parallel \hat{\mathbf{i}}$.
1057 The side \overline{OF} is hypotenuse of a right angled triangle. Its ancatethete with respect to
1058 the angle θ has length f . Therefor the we can deduce the length $|\overline{OF}| = f / \cos \theta$.

Between the two similar triangles, the following relation holds and can be used to calculate the length $|\overline{BC}|$:

$$\frac{|\overline{BC}|}{|\overline{BA}|} = \frac{|\overline{OA}|}{|\overline{OF}|} \quad (\text{B.33}) \{?\}$$

$$\frac{|\overline{CB}|}{1} = \frac{\rho}{f / \cos(\theta)}. \quad (\text{B.34}) \{?\}$$

Given its length, the vector \overline{CB} can now calculated, because we know its direction to be along ρ . With this vector and $\hat{\mathbf{i}}$ we can now obtain the (arbitrarily scaled) transmitted vector \mathbf{r}' . We could normalize it but it turns out to be useful for the high NA immersion lens to find the vector \mathbf{r} , that ends in the focal plane. The procedure from above is condensed in the following equations:

$$\rho = (x_0, y_0, 0)^T = \rho(\cos \phi, \sin \phi, 0)^T \quad (\text{B.35}) \{?\}$$

$$\phi = \arctan(y_0/x_0) \quad (\text{B.36}) \{?\}$$

$$\cos \theta = |\hat{\mathbf{i}} \hat{\mathbf{z}}| \quad (\text{B.37}) \{?\}$$

$$\mathbf{r}' = \hat{\mathbf{i}} - \frac{\cos \theta}{f} \rho \quad (\text{B.38}) \{?\}$$

$$\mathbf{r} = \boxed{\frac{f}{\cos \theta} \hat{\mathbf{i}} - \rho} \quad (\text{B.39}) \{?\}$$

1059 B.5. Refraction through oil objective (illumination)

1060 It is possible to augment the results of the calculation from the previous chapter to
1061 treat an aplanatic immersion objective (Hwang and Lee 2008).

B. Raytracing for spatio-angular microscopy

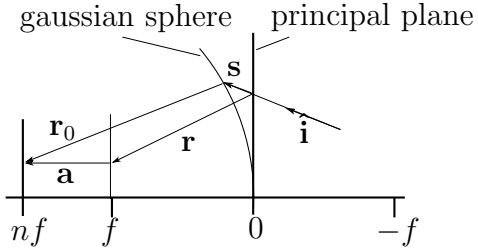


Figure B.4.: Construction of a ray on an high numerical aperture oil immersion objective. As opposed to a thin air lens the objective's focal length needs to be corrected by the focus difference vector \mathbf{a} to accommodate for the immersion and we must take into account spherical principal surface.

We account for the immersion medium by shifting the focal plane in sample space to nf using the focus difference vector \mathbf{a} .

$$\mathbf{a} = \boxed{f(n - 1)\hat{\mathbf{z}}} \quad (\text{B.40}) \{ ? \}$$

$$R = \boxed{nf} \quad (\text{B.41}) \{ ? \}$$

The principal surface² is a sphere of radius $R = nf$ around the image point (Smith (2000) p. 22 and Botcherby et al. (2008)). In the paper (Hwang and Lee 2008) they express the deviation between the real principal surface and the principal plane with an approximation for small angles θ and ϕ :

$$\mathbf{s} = \boxed{(R - \sqrt{R^2 - \rho^2})\hat{\mathbf{i}}} \quad (\text{B.42}) \{ ? \}$$

1062 This is an approximation because it only takes into account the perpendicular (along
 1063 \mathbf{z}) distance between plane and sphere. They demonstrate the viability of this ap-
 1064 proximation by comparing its results with a full raytrace through a 100×1.41
 1065 objective. Focus displacement errors are less than 130 nm for a field of $86.4 \mu\text{m}$ ra-
 1066 dius. This is sufficient for our problem. As we anyway have the code for a ray–sphere
 1067 intersection, we can use it here as well and calculate an exact vector \mathbf{s} .

The final ray exiting the objective has the direction \mathbf{r}_0 :

$$\mathbf{r}_0 = \boxed{\mathbf{r} + \mathbf{a} - \mathbf{s}}. \quad (\text{B.43}) \{ ? \}$$

²An image forming system focuses parallel light into a point. Its principal surface is the surface where an incident parallel ray intersects with a line along the transmitted image forming ray.

1068 B.6. Reverse path through oil objective (detection)

1069 Now we consider the oil objective in the reverse direction (see Figure B.6). We have
 1070 a ray starting within the sample and want to know the transmitted ray in the pupil.

1071 B.6.1. Easy case: back focal plane positions only

1072 If we are only interested in positions of rays in the back focal plane, we don't have
 1073 to do full raytracing. If we are imaging beads in index matched embedding medium
 1074 and we want to calculate shadow maps for the MMA (see section 3.5.1), we don't
 1075 need a full raytrace. Instead it is sufficient to ignore ray origins and just consider
 1076 their directions.

A unit ray direction $\hat{\mathbf{i}} = (x, y, z)^T$ in sample space is transformed into a position $\mathbf{r}_b = (x', y')^T$ in the back focal plane of the objective. The azimuthal angle ϕ isn't changed when going through the objective. The polar angle θ defines how far off axis the back focal plane is hit.

$$\phi' = \phi = \arctan(y/x) \quad (\text{B.44}) \{?\}$$

$$\theta = \arcsin(\sqrt{x'^2 + y'^2}) \quad (\text{B.45}) \{?\}$$

$$r_b = n_f \sin \theta \quad (\text{B.46}) \{?\}$$

$$\mathbf{r}_b = r_b (\cos \phi', \sin \phi')^T \quad (\text{B.47}) \{?\}$$

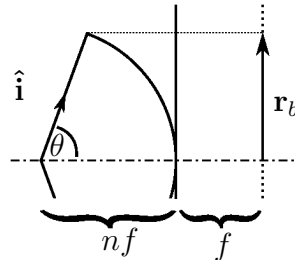


Figure B.5.: Schematic for tracing a ray direction $\hat{\mathbf{i}}$ from sample space into the back focal plane. The bigger the angle between $\hat{\mathbf{i}}$ and the optical axis, the further outside the ray will pass through the back focal plane.

1077

1078 B.6.2. Full raytrace

1079 If we are also interested in the angles of the transmitted rays in the back focal plane,
 1080 when we want to trace the rays further into the camera or if we want to consider

B. Raytracing for spatio-angular microscopy

1081 aberrations due to an index mismatch of the embedding medium, we will have to
1082 calculate a full raytrace, as described below.

The position of the objective is defined by its principal point \mathbf{c} and the normal $\hat{\mathbf{n}}$ (directed along optical axis towards sample space). The incident ray is defined by its starting point \mathbf{p} and the direction $\hat{\mathbf{i}}$. First we calculate the centre of the Gaussian sphere \mathbf{g} :

$$\mathbf{g} = \mathbf{c} + nf\hat{\mathbf{n}}. \quad (\text{B.48}) \{?\}$$

Then we obtain the position \mathbf{p}' by intersecting the incident ray and the plane perpendicular to the optical axis through \mathbf{g} . The focus difference vector is defined by its length and the optical axis. It can be used to calculate an intermediate point \mathbf{p}'' .

$$\mathbf{a} = -f(n-1)\hat{\mathbf{n}} \quad (\text{B.49}) \{?\}$$

$$\mathbf{p}'' = \mathbf{p}' + \mathbf{a}. \quad (\text{B.50}) \{?\}$$

The point \mathbf{p}'' has now been shifted, so that a thin air lens would image it exactly as the oil objective would image \mathbf{p}' . We can use \mathbf{p}'' to find the direction $\hat{\mathbf{t}}$ of the transmitted ray. It is just the normalized difference vector \mathbf{m} to the principal point.

$$\mathbf{m} = \mathbf{c} - \mathbf{p}'' \quad (\text{B.51}) \{?\}$$

$$\hat{\mathbf{t}} = \mathbf{m}/|\mathbf{m}|. \quad (\text{B.52}) \{?\}$$

1083 As a last step we calculate the starting point \mathbf{e} of the transmitted ray by intersecting the incident ray with the Gaussian sphere.

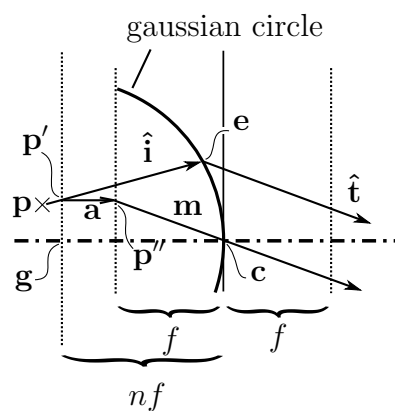


Figure B.6.: Construction to find the transmitted ray through an oil immersion objective from a point within the sample.

1084 `<fig:obj-ref-full>`

1085 B.6.3. Treatment of aberration (detection)

<sec:ray-aberration> Now we consider a ray originating in point \mathbf{p} with direction $\hat{\mathbf{i}}$ within an immersion of index n_e . We want to treat the problem of a non-matched embedding medium $n_e \neq n$. We find the intersection \mathbf{f} of the ray with the coverslip-embedding interface and refract to obtain $\hat{\mathbf{i}}'$. We calculate the time t a photon takes, to travel from \mathbf{p} to the interface \mathbf{p} :

$$t = |\mathbf{f} - \mathbf{p}|n_e c \quad (\text{B.53}) \{?\}$$

1086 and extend the path of the photon backward along $\hat{\mathbf{i}}'$ by $t/(cn)$. This results in the
1087 corrected position \mathbf{p}' that indicates where the photon would have originated if the
1088 embedding would have been index matched. Now we can apply the equations from
1089 the previous sections on the ray defined by \mathbf{p}' and $\hat{\mathbf{i}}'$ to obtain the transmitted ray
1090 in the pupil.

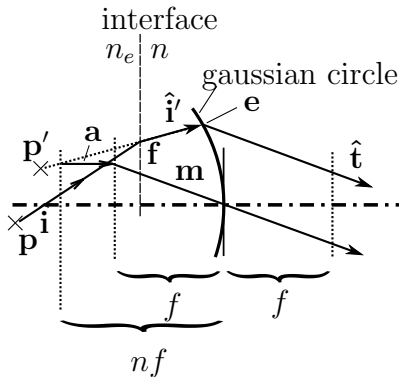


Figure B.7.: Construction that treats the interface between embedding and immersion medium

1091 B.7. Sphere projection

<sec:sphere-projection> When we model our sample as a collection of spheres, it is useful to trace rays from
1092 the periphery of these spheres through an in focus target \mathbf{c} into the back focal plane.
1093 Here we construct the rays.

The tangents of an out of focus sphere S_r^s centred at \mathbf{s} with radius r that pass through the target \mathbf{c} form a double cone (assuming \mathbf{c} is outside of S_r^s). The tangents touch the surface of the sphere S_r^s at the circular intersection C with the sphere S_R^c centred at \mathbf{c} with radius $R = |\mathbf{c} - \mathbf{s}|$. Radius R is the distance from the target to the centre of the out of focus sphere. In order to find a point \mathbf{e} where a tangent

B. Raytracing for spatio-angular microscopy

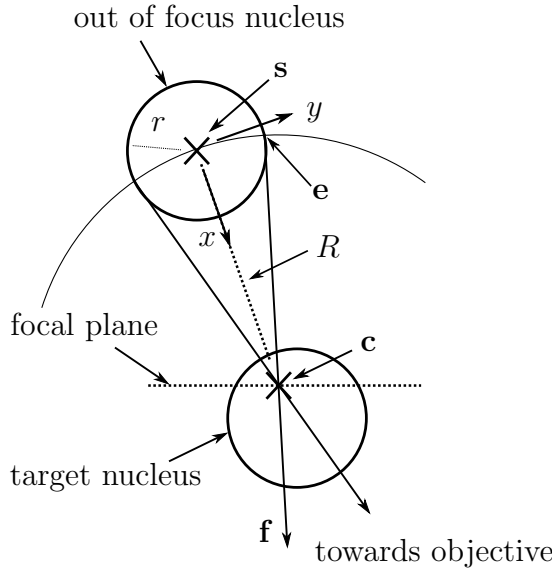


Figure B.8.: Schematic of how an out of focus nucleus defines a cone of tangential rays.

touches the out of focus sphere, it is sufficient to solve the following equation in a 2D coordinate system with the origin in the centre \mathbf{s} of the out of focus sphere:

$$(x - R)^2 + y^2 = R^2 \quad (\text{B.54}) \quad \{\text{?}\}$$

$$x^2 + y^2 = r^2 \quad (\text{B.55}) \quad \{\text{?}\}$$

There are two solutions:

$$x_1 = \frac{r^2}{2R} \quad (\text{B.56}) \quad \boxed{\text{eqn:x1}}$$

$$y_{1/2} = \pm \frac{r}{2R} \sqrt{4R^2 - r^2} \quad (\text{B.57}) \quad \boxed{\text{eqn:y1}}$$

- 1095 In the case $R < r$ the out of focus nucleus is intersecting the target, obviating the
1096 reason to do the projection in the first place.

We construct two vectors $\hat{\mathbf{x}}$ and $\hat{\mathbf{y}}$ in order to transform the solution from 2D into 3D. The (unnormalized) direction \mathbf{x} of the x-axis of this coordinate system is given by the difference vector of the target \mathbf{c} and the nucleus centre \mathbf{s} . The direction \mathbf{y} must be perpendicular to \mathbf{x} and is obtained by calculating the cross product with another vector \mathbf{q} . We ensure that \mathbf{q} and \mathbf{x} are not colinear. The vectors \mathbf{q} and \mathbf{x} are colinear, when the absolute value of their scalar product equals the square of

B. Raytracing for spatio-angular microscopy

the length $|\mathbf{q}\mathbf{x}| = \mathbf{x}^2$.

$$\mathbf{x} = \mathbf{c} - \mathbf{s} \quad (\text{B.58}) \{?\}$$

$$\mathbf{q} = \begin{cases} (0, 0, 1)^T & \text{when } |x_z| < \frac{2}{3}|\mathbf{x}| \\ (0, 1, 0)^T & \text{else} \end{cases} \quad (\text{B.59}) \{?\}$$

$$\mathbf{y} = \mathbf{x} \times \mathbf{q} \quad (\text{B.60}) \{?\}$$

$$\hat{\mathbf{x}} = \mathbf{x}/|\mathbf{x}| \quad (\text{B.61}) \{?\}$$

$$\hat{\mathbf{y}} = \mathbf{y}/|\mathbf{y}| \quad (\text{B.62}) \{?\}$$

Now we can sample the intersection circle C in order to create viable starting points \mathbf{e} for tangential rays. Let $R_{\phi}^{\hat{\mathbf{c}}}$ be a rotation matrix that rotates a vector by angle ϕ around an axis $\hat{\mathbf{c}}$. A point \mathbf{e} on the circle is then defined using one solution from equations B.56 and B.57. The ray direction \mathbf{f} is then easily obtained:

$$\mathbf{e} = \mathbf{s} + x_1 \hat{\mathbf{x}} + y_1 R_{\phi}^{\hat{\mathbf{x}}} \hat{\mathbf{y}} \quad (\text{B.63}) \{?\}$$

$$\mathbf{f} = \mathbf{c} - \mathbf{e}. \quad (\text{B.64}) \{?\}$$

1097 Tracing a sufficient number of rays (e.g. 16) with direction \mathbf{f} for different angles ϕ
1098 to the back focal plane gives the projection of the intersection circle C . Note that
1099 this projection in general is not a circle anymore.

1100 For practical reasons its useful to project vector \mathbf{x} as well. It can be used as the
1101 centre of the (distorted) shape on the back focal plane to rasterize it as a fan of
1102 triangles.

1103 C. Transforming camera coordinates 1104 into LCoS coordinates

`<sec:rigid>` In order to relate coordinates on the LCoS display with pixel positions on the camera, we found it suffices to use a rigid transform. The rigid transform between display and camera is defined as:

$$\mathbf{r}^d = s\mathbf{R}_\phi \mathbf{r}^c + \mathbf{t} \quad (\text{C.1}) \{?\}$$

$$\mathbf{R}_\phi = \begin{pmatrix} \cos \phi & q \sin \phi \\ -\sin \phi & q \cos \phi \end{pmatrix} \quad (\text{C.2}) \{?\}$$

1105 where \mathbf{r}^d is a point on the display, \mathbf{r}^c is a point on the camera and q can be either
1106 +1 or -1 dependent on if there is a reflection.

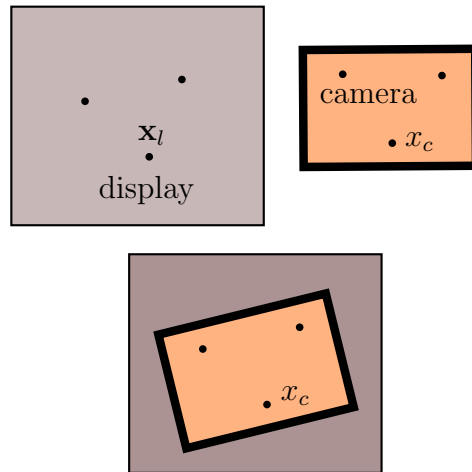


Figure C.1.: Given $n > 3$ camera images of a display showing one point it is possible to calculate the parameters of the rigid transform parameters scaling s , rotation angle ϕ , translation vector \mathbf{t} .

?<fig:calib-align)?

One can find the transform parameters scaling s , rotation angle ϕ , translation

C. Transforming camera coordinates into LCoS coordinates

vector \mathbf{t} by minimizing

$$\sum_i^n |sR_\phi \mathbf{r}_i^c + \mathbf{t} - \mathbf{r}_i^d|^2 \quad (\text{C.3}) \{?\}$$

for all n points on the display \mathbf{r}_i^d and there corresponding camera positions \mathbf{r}_i^c . Each term of the sum can be expressed as two scalar terms:

$$\begin{aligned} & \sum_i^n |s(\cos \phi r_{ix}^c + q \sin \phi r_{iy}^c) + t_x - r_{ix}^d|^2 \\ & + |s(-\sin \phi r_{ix}^c + q \cos \phi r_{iy}^c) + t_y - r_{iy}^d|^2 \end{aligned}$$

1107 The following Maxima code will find the solution to the least squares problem:

```
1108 load(minpack)$
1109 q:-1;
1110 g(s,p,tx,ty):=[ 
1111 s*( cos(p)*<cx>+q*sin(p)*<cy>)+tx-<dx>,
1112 s*(-sin(p)*<cx>+q*cos(p)*<cy>)+ty-<dy>
1113 ...
1114 ]$ 
1115 minpack_lsquares(
1116   g(s,p,x,y),
1117   [s,p,x,y],
1118   [0.88,-3.1,1200,-20]);
```

1119 We define the function g to contain all the terms of the sum. This can easily written
1120 by a program that constructs the lines according to the given pattern, replacing
1121 $\langle cx \rangle, \langle cy \rangle$ with camera coordinates and $\langle dx \rangle, \langle dy \rangle$ with display coordinates.

1122 The function `minpack_lsquares` calls the subroutine `lmder` from the Fortran
1123 package `minpack`.

```
1124 C      subroutine lmder (http://www.netlib.org/minpack/lmder.f)
1125 C
1126 C      the purpose of lmder is to minimize the sum of the squares of
1127 C      m nonlinear functions in n variables by a modification of
1128 C      the levenberg-marquardt algorithm. the user must provide a
1129 C      subroutine which calculates the functions and the jacobian.
1130 C
1131 C      the subroutine statement is
```

C. Transforming camera coordinates into LCoS coordinates

```

1132  C
1133  C      subroutine lmder(fcn,m,n,x,fvec,fjac,ldfjac,ftol,xtol,gtol,
1134  C                           maxfev,diag,mode,factor,nprint,info,nfev,
1135  C                           njev,ipvt,qtf,wa1,wa2,wa3,wa4)

```

1136 An advantage of using Maxima is, that it conveniently calculates the symbolic
1137 jacobian for the problem.

1138 The following Common Lisp code shows how the result of the optimization can be
1139 used to initialize the OpenGL modelview matrix to transform objects in its buffer,
1140 so that they will appear at the given positions on the camera.

```

1141 (defun load-cam-to-lcos-matrix (&optional (x 0s0) (y 0s0))
1142   (let* ((s 0.828333873909549)
1143         (sx s)
1144         (sy (- s))
1145         (phi -3.101722728951688)
1146         (sp (sin phi))
1147         (cp (cos phi))
1148         (tx 608.4330743004457)
1149         (ty 168.9188383630887)
1150         (a (make-array
1151           (list 4 4) :element-type 'single-float
1152           :initial-contents
1153           (list (list (* sx cp)    (* sy sp) .0 (+ x tx))
1154                 (list (* -1 sx sp) (* sy cp) .0 (+ y ty))
1155                 (list .0 .0 1.0 .0)
1156                 (list .0 .0 .0 1.0))))))
1157   (gl:load-transpose-matrix (sb-ext:array-storage-vector a)))

```

1158 Alternatively, here is the equivalent code in C:

```

1159 float m[4*4]; // OpenGL Modelview Matrix
1160 float s=-.8749328910202312,
1161     sx=s, sy=-s, phi=-.8052030670943575,
1162     cp=cos(phi), sp=sin(phi),
1163     tx=1456.71806436377,
1164     ty=910.4787738693659;
1165     m[0]=sx*cp;
1166     m[1]=-1*sx*sp;
1167     m[2]=0;

```

C. Transforming camera coordinates into LCoS coordinates

```

1168     m[3]=0;
1169
1170     m[4]=sy*sp;
1171     m[5]=sy*cp;
1172     m[6]=0. ;
1173     m[7]=0. ;
1174
1175     m[8]=0;
1176     m[9]=0;
1177     m[10]=1;
1178     m[11]=0;
1179
1180     m[12]=tx;
1181     m[13]=ty;
1182     m[14]=0;
1183     m[15]=1;
1184     glMatrixMode(GL_MODELVIEW);
1185     glLoadMatrixf(m);

```

1186 For the calibration a fluorescent plane (see Figure C.2 left for a uniform widefield
 1187 image) is imaged with the LCoS display showing spots in the illuminated area. Ide-
 1188 ally for this measurement all mirrors on the MMA are undeflected and the apertures
 1189 B_0 and B_1 completely open (see Figure 3.3). Then the square exit of the integrating
 1190 tunnel illuminates the biggest possible area on the LCoS.

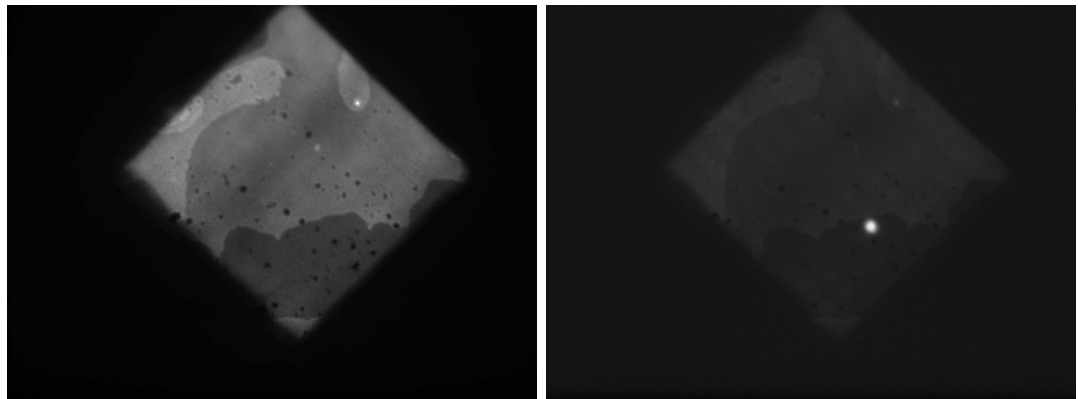


Figure C.2.: **left:** Uniformly illuminated fluorescent plane (mono and double layer of yellow beads with 110 nm diameter, excited with 473 nm laser in a 63x/1.47 objective). **right:** Image with the the LCoS displaying a disk with 24 pixels diameter (corresponding to 2.4 μm in the sample) centred at LCoS position (550, 750).

`{fig:rigid-pics}`

C. Transforming camera coordinates into LCoS coordinates

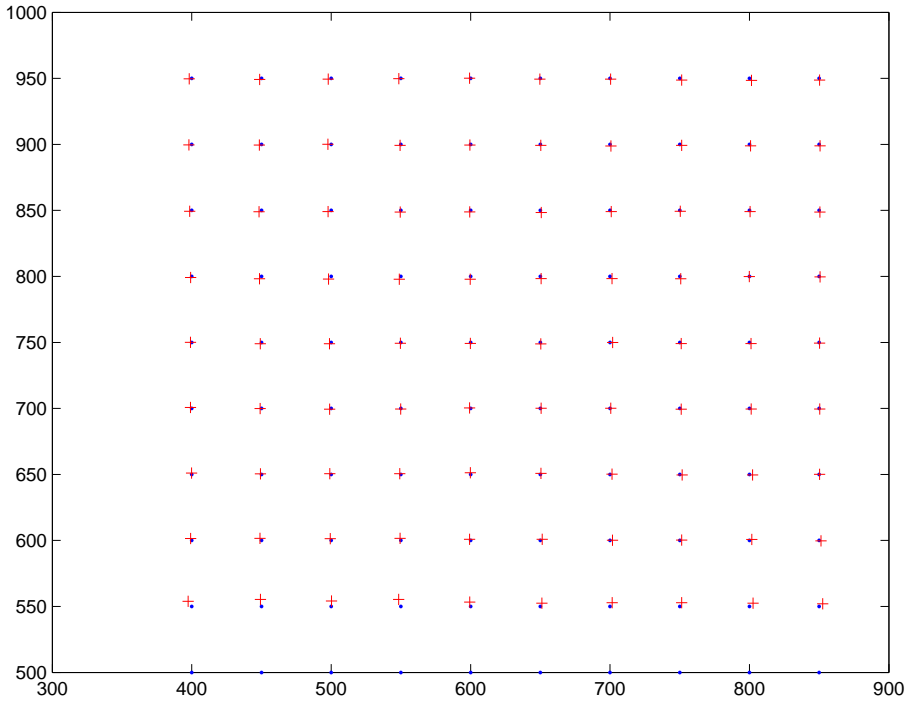


Figure C.3.: Red “+” signs indicate where the spots that were localized in the camera images end up after a rigid transform. There is sufficient agreement with the original display positions.

?<fig:rigid-compare)?

1191 For the calibration 10×10 images were captured with a disk of 24 pixels diameter
 1192 at the positions $(400 + 50i, 500 + 50j) \forall i, j \in [0, 99]$. Furthermore, one uniformly il-
 1193 luminated image is used to correct for intensity fluctuations in the fluorescent plane.
 1194 The following Matlab/DIPimage code is used to normalize the images and localize
 1195 the spots. The coordinates are then assembled into the Maxima command that
 1196 finds the parameters of the rigid transform. Finally the transformed spot positions
 1197 from the camera images are compared with the original LCoS pixel positions.

```

1198 %% load the files
1199 % 0 .. 99 spot images
1200 % only 10..99 usable because the first are on border and not illuminated
1201 a = newim(1392,1040,103);
1202 for i=0:102
    % Andor's FITS format isn't read correctly
    % correct this by adding 2^15
    a(:,:,i) = 2^15 + readim(sprintf('o%03d.fits',i));
1206 end
1207
1208 %% bright image is at position 102 in the stack

```

C. Transforming camera coordinates into LCoS coordinates

```

1209 % diphist(a(:,:,102),[min(a),max(a)])
1210
1211 %% bright image has minimum at 800 ADU
1212 bright = squeeze(a(:,:,102));
1213 % create mask with illuminated area
1214 mask = gaussf(bright,8) > 800;
1215
1216 %% the background is be 510 ADU
1217 % diphist(a(:,:,0),[min(a),max(a)])
1218 bg = 510;
1219
1220 posmax = newim(100,2);
1221 for i = 10:99
1222     % correct for sample non-uniformity with homogene image (102)
1223     corr = (squeeze(a(:,:,i)) - bg) / bright * mask;
1224     % find coordinates of maximum
1225     [coords,vals]=findmaxima(gaussf(corr,32));
1226     [valss,valsind] = sort(vals);
1227     tmp = coords(valsind,:);
1228     posmax(i,:) = tmp(end,:);
1229 end
1230
1231 %% store the positions as ascii text
1232 q = double(posmax)';
1233 save /dev/shm/o.mat q -ASCII -DOUBLE
1234
1235 %% create maxima input for optimization
1236 c = double(posmax)';
1237
1238 cmd = '';
1239 for i=10:99
1240     dx = num2str(400+50*mod(i,10));
1241     dy = num2str(500+50*floor(i./10));
1242     cx = num2str(c(i+1,1));
1243     cy = num2str(c(i+1,2));
1244     cmd=[cmd ' s*( cos(p)*' cx '+q*sin(p)*' cy ') +tx-' dx ',s*(-sin(p)*' ...
1245             cx '+q*cos(p)*' cy ') +ty-' dy ','];
1246 end
1247

```

C. Transforming camera coordinates into LCoS coordinates

```

1248 cmd(:,end) = [] ; % delete last comma
1249
1250 % load the fitting package and start defining the merit function g
1251 pre = 'load(minpack)$ q:-1; g(s,p,tx,ty):=[';
1252 % now put cmd between
1253 % call the fitting function and store the parameters into /dev/shm/max.out
1254 cod = [']$ fit:minpack_lsquares(g(s,p,x,y),[s,p,x,y],[.88,-1.3,1200,-20]);' ...
1255 'write_data(fit[1],"./home/martin/max.out");'
1256
1257 %% write maxima commands into file and execute
1258 fid = fopen('/dev/shm/fit.max','w');
1259 fwrite(fid,[pre cmd cod]);
1260 fclose(fid);
1261 [max_status,max_result]=system('maxima -b ./dev/shm/fit.max');
1262
1263 %% load rigid transformation parameters from the file into matlab
1264 params = load('./home/martin/max.out');
1265 scale = params(1); phi = params(2);
1266 tx = params(3); ty = params(4);
1267
1268 mirr = -1;
1269 R = [cos(phi),mirr*sin(phi);
1270        -sin(phi),mirr*cos(phi)];
1271 T = [tx ty]';
1272
1273 %% plot the two grids on top of each other
1274 mapped = zeros(100,2);
1275 for i=11:100 % camera coordinates into display coordinates
1276     mapped(i,:) = (scale*R*q(i,:)' + T)';
1277 end
1278
1279 dpos = zeros(100,2);
1280 for i=0:99 % calculate display points
1281     dpos(i+1,1) = 400+50*mod(i,10);
1282     dpos(i+1,2) = 500+50*floor(i./10);
1283 end
1284
1285 hold off; plot(dpos(:,1),dpos(:,2),'.');
1286 hold on; plot(mapped(11:end,1),mapped(11:end,2),'r+');

```

1287 D. Implementation of a robust 1288 structured illumination 1289 reconstruction technique

1290 We implement a robust technique to computationally recover sectioned im-
1291 ages from only two structured illumination image and propose a modification
1292 of the algorithm that may be beneficial if gratings are produced with a spatial
1293 light modulator.

1294 D.1. Simulated image acquisition

1295 As a test object we create a thick sphere shell, a line and a rectangle. The sphere
1296 shell will provide out of focus light, which we then try to remove. The objective is a
1297 NA1.4 oil with coherent 473 nm excitation light and incoherent detection at 520 nm.

1298 The following listing shows how the image of the grating for structured excitation
1299 is calculated. The z-section of the result is shown in Figure D.1. The illumination
1300 source is coherent therefor the grating structure is repeated over nearly $6 \mu\text{m}$ in z
1301 (Talbot effect).

```
1302 n=128;
1303 nmperpixel=100; % one pixel is corresponds to 100nm
1304 sz=2;
1305 NA=1.4;
1306 znmperpixel=sz*nmperpixel;
1307 %% vector amplitude point spread function for excitation
1308 asf=squeeze(kSimPSF({'lambdaEx',473,'na',NA,'ri',1.518;...
1309 'sX',n;'sY',n;'sZ',sz*n;...
1310 'scaleX',nmperpixel;'scaleY',nmperpixel;'scaleZ',znmperpixel;...
1311 'computeASF',1}));%
1312 P=6; % grating period
1313 grat2d=(mod(xx(n,n),P)>(floor(P/2)-1))*1000;
1314 grat=newim(n,n,sz*n); % copy the 2D grating into middle of volume
```

D. Implementation of a robust structured illumination reconstruction technique

```

1316 grat(:,:,sz*n)/2)=grat2d(:,:,);
1317 kgrat=ft(grat);
1318 imgratx=ift(kgrat.*ft(squeeze(asf(:,:,0))));% field components
1319 imgraty=ift(kgrat.*ft(squeeze(asf(:,:,1))));% in sample for
1320 imgratz=ift(kgrat.*ft(squeeze(asf(:,:,2))));% coherent image
1321 % intensity distribution in sample space:
1322 imgrat=abs(imgratx).^2+abs(imgraty).^2+abs(imgratz).^2
1323

```

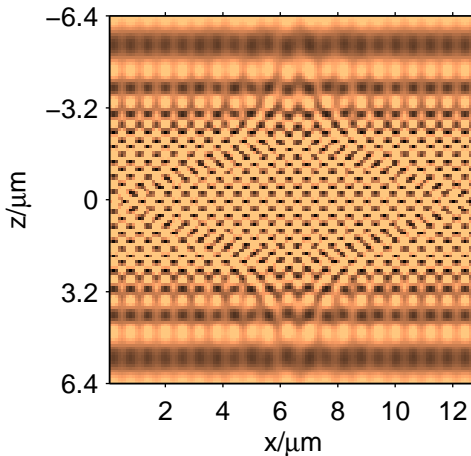


Figure D.1.: $x - z$ -Section of the intensity distribution $\text{imgrat}(:, 64, :)$ of the coherent image of the grating in sample space.

`(fig:grating)`

1324 The following listing shows how the sample object, i.e. fluorophore concentration, is
1325 generated. The spherical shell is calculated as the product of two Sinc functions in k-
1326 space and a product with r in real space. There is also a vertical line and a rectangle.
1327 A slice through the simulated fluorophore concentration is shown Figure D.2 left.
1328 Note that the sphere is very faint but it is the only of the three objects that is
1329 extended in z .

1330 The shift by dz in z -direction is done by multiplication with $\exp(-ik\text{dz})$ in k-
1331 space. This is only a good method to defocus small distances dz as the object will
1332 wrap around the borders.

```

1333 %% hollow sphere
1334 kobj=sinc(rr(kpsf)./2).*sinc(rr(kpsf)./0.7);% in k-space
1335 obj=rr(psf).*abs(ift(kobj));% this is the sphere
1336 maximum=max(obj);
1337 obj(83:114,23:43,(sz*n)/2)=4*maximum;% rectangle in-focus rig ht ←
1338 top
1339 obj(21:21,40:90,(sz*n)/2)=12*maximum;% in-focus line on the left
1340 kobj=ft(obj);% shift the object a little bit in z
1341

```

D. Implementation of a robust structured illumination reconstruction technique

```

1342 %dz=1; % shift in pixels -> 1 equals 100nm
1343 kobj=kobj.*exp(-i*2*pi*zz(kobj,'freq')*dz);
1344 obj=ift(kobj);

```

1346 In order to simulate the final image the fluorophore concentration is multiplied by
 1347 the excitation intensity and the result is convolved with the detection point spread
 1348 function (PSF) of the microobjective (this time according to the rules of incoherent
 1349 imaging).

```

1350
1351 %% for imaging the fluorescence light
1352 psf=kSimPSF({'lambdaEx',473;'lambdaEm',520;'na',1.4;'ri',1.518;...
1353 'sX',n;'sY',n;'sZ',sz*n;'scaleX',nmPerPixel;...
1354 'scaleY',nmPerPixel;'scaleZ',znmPerPixel});
1355 kpsf=ft(psf); % otf
1356 fluo=obj.*imgrat; % excited fluorophores
1357 strucflimg=ift(ft(fluo).*kpsf); % fluorescence image with
1358 % structured illumination
1359 flimg=ift(ft(obj).*kpsf); % widefield fluorescence image
1360 %% extract focal planes
1361 iu=real(squeeze(flimg(:,:,sz*n/2))); % uniform illumination
1362 in=real(squeeze(strucflimg(:,:,sz*n/2)));% structured illumination

```

1364 The image for uniform illumination is shown in the middle of Figure D.2. The
 1365 right picture shows the image for non-uniform illumination with the 600 nm-period
 grating. Figure D.3 shows the non-uniformly illuminated images for the object

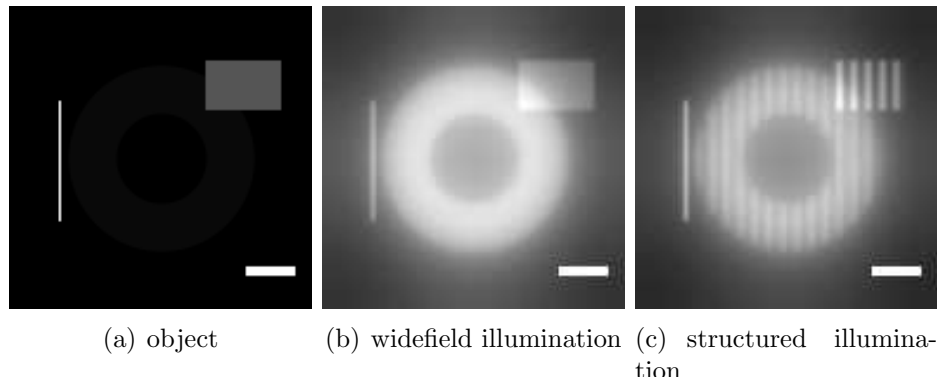


Figure D.2.: Slice of the object in the focal plane. It consists of a line, a spherical shell and a rectangle. Only the shell is extended in z. **(a)**, Image with widefield illumination. **(b)**, Image with structured illumination (grating period 600 nm). **(c)** The scalebar is 2 μ m wide.

`<fig:input>`

1366 being moved relative to the plane of focus. The line and the rectangle are both

D. Implementation of a robust structured illumination reconstruction technique

1368 blurred and the contrast of the grating decreases. One can still see the image of the grating in the sphere.

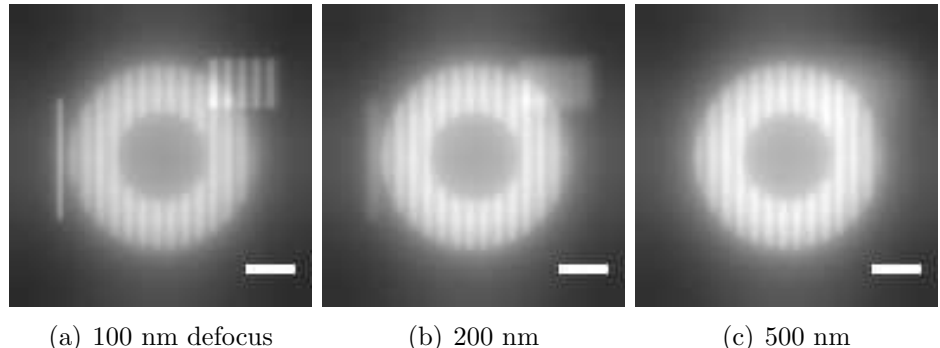


Figure D.3.: Defocus series of the test object under structured coherent illumination (grating period 600 nm). The scalebar is $2 \mu\text{m}$ wide.

1369 `(fig:defocus)`

1370 D.2. Fundamentals of structured illumination

1371 If a fluorescent plane is imaged with a fluorescence widefield microscope, the inten-
1372 sity of the image is constant no matter if the plane is in focus or not (missing cone
1373 problem).

1374 D.2.1. Apotome

1375 Using non-uniform excitation light Neil et al. (1997) circumvents this problem.
1376 They project a grid pattern into the sample. For a fluorescent plane sample the
1377 modulation in the image is highest, when the sample is in focus. If the plane
1378 is moved out of focus, the modulation decreases. Hence it is possible to achieve
1379 z-sectioning in a widefield microscope.

For one section I_p they combine three grating images I_i (grating period $1/\nu$) with different phases:

$$I_p = |I_1 + I_2 e^{i2\pi/3} + I_3 e^{i4\pi/3}| \sim \left| 2 \frac{J_1(2u\nu(1 - \nu/2))}{u\nu(1 - \nu/2)} \right|. \quad (\text{D.1}) \{?\}$$

1380 The last term is their result for the intensity of a fluorescent plane with the
1381 defocus u . If no grating is displayed ($\nu = 0$) the resulting image I_p is constant and
1382 the microscope has no sectioning capability. A fine grating gives best sectioning
1383 capability. However sometimes there is also a trade off to be made because a fine
1384 grating will give very low contrast in a thick specimen.

D. Implementation of a robust structured illumination reconstruction technique

1385 For their reconstruction method it is necessary to capture three images to generate
 1386 one sectioned slice. This can be a problem if the movement of the grating isn't
 1387 perfect or if the object moves during these exposures.

1388 D.2.2. HiLo

This problem is addressed by Lim et al. (2008) and Santos et al. (2009). They describe an approach, where only two images need to be captured for each z -sectioned slice. An image with uniform illumination contains contributions of both in-focus and out of focus fluorophores:

$$I_u(x, y) = I_{\text{in}}(x, y) + I_{\text{out}}(x, y). \quad (\text{D.2}) \boxed{\text{eqn:Iu}}$$

The contribution from out of focus light I_{out} is limited to low spatial frequencies, i.e. $\tilde{I}_{\text{out}}(k_x, k_y)$ has small support. The modulated part of the non-uniformly illuminated image I_n contains only information of the in-focus object structure:

$$I_n(x, y) = I_{\text{in}}(x, y)(1 + M \sin(\kappa x + \varphi)) + I_{\text{out}}(x, y), \quad (\text{D.3}) \boxed{\text{eqn:In}}$$

$$\kappa = \frac{2\pi}{\lambda} n \sin(\alpha) \nu. \quad (\text{D.4}) \{?\}$$

1389 We can recover the sectioned image as a combination of high-frequency components
 1390 of the widefield image I_u and the low-frequency components of the modulated part
 1391 of the non-uniform image I_n .

1392 Using speckle pattern as non-uniform illumination (local variance estimation)

1393 In the older publication (Lim et al. (2008)) a random speckle pattern is projected
 1394 into the sample. For comparison with the other methods we describe a reimplementa-
 1395 tion of their method.

In order to process the non-uniform image it is divided into subregions. As a measure of local contrast in each of these subregions the relative standard deviation c is calculated (the operator $\langle \cdot \rangle$ indicates averaging over a pixel neighbourhood):

$$c_n = \frac{\sqrt{\langle I_n^2 \rangle - \langle I_n \rangle^2}}{\langle I_n \rangle}. \quad (\text{D.5}) \{?\}$$

1396 The relative standard deviation c_n will be zero for image regions without in-focus
 1397 contributions. Its value increases as the modulation of the non-uniform illumination
 1398 increases (that's what we want). However c_n also increases if there is a small in-

D. Implementation of a robust structured illumination reconstruction technique

1399 focus feature. In that we are not interested as we only want to build up an image
 1400 of in-focus fluorophores with low spatial frequencies.

The authors state that a corrected relative standard deviation c_s of the non-uniform illumination can be obtained by removing the standard deviation $c_0 = \frac{\sqrt{\langle I_u^2 \rangle - \langle I_u \rangle^2}}{\langle I_u \rangle}$ of the widefield image:

$$c_s^2 = \frac{c_n^2 - c_0^2}{1 + c_0^2} = \frac{\langle I_n^2 \rangle}{\langle I_n \rangle^2} \frac{\langle I_u^2 \rangle}{\langle I_u \rangle^2} - 1. \quad (\text{D.6}) \{?\}$$

1401 The product $I_{su} = c_s \langle I_u \rangle$ then provides a low resolution version of I_u that is optically
 1402 sectioned even for dc frequencies.

1403 The following listing shows how this algorithm can be applied to two input images
 1404 `iu` and `in`. Instead of doing a discrete integration over regions we multiply with a
 1405 Gaussian in Fourier space. The cutoff frequency k_c of the filter is chosen low enough
 1406 so that c_s doesn't contain any structure of the grating anymore.

```
1407
1408 si=size(in); n=si(1); % only square images
1409 kc=0.04; % filter cutoff
1410 r=rer(in, 'freq');
1411 klp=exp(-r.^2/(2*kc.^2)); % low pass
1412 khp=1-klp; % high pass
1413 ina=ift(ft(in).*klp);
1414 in2a=ift(ft(in.^2).*klp);
1415 iua=ift(ft(iu).*klp);
1416 iu2a=ift(ft(iu.^2).*klp);
1417 cs2=in2a.*iua.^2./(ina.^2.*iu2a)-1;
1418 isu=sqrt(cs2).*iua; % sectioned version of iu
1419 kihp=ft(iu).*khp;
1420 kilp=ft(isu).*klp;
```

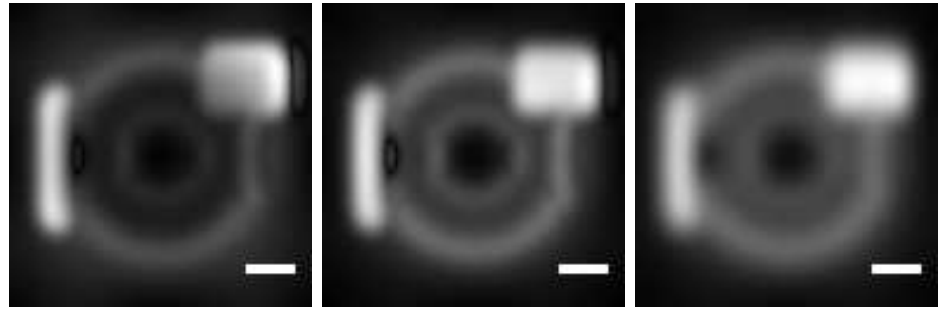
The HiLo method combines a low-pass filtered version of I_{su} with a high pass filtered version of the uniformly illuminated image I_u . To do this the two images are scaled for a seamless interface along the circle K with radius $|\mathbf{k}_c|$ in k-space and then added:

$$\eta = \oint_{\partial K_{k_c}} \frac{|I_{hp}|}{|I_{lp}|} d\mathbf{k}, \quad (\text{D.7}) \{?\}$$

$$I_{\text{hilo}} = \eta I_{\text{lp}} + I_{\text{hp}}. \quad (\text{D.8}) \{?\}$$

1422 This is done in the following listing:

D. Implementation of a robust structured illumination reconstruction technique



(a) Corrected relative standard deviation c_s . (b) The product $I_{su} = c_s I_u$ (c) Low spatial frequency section I_{lp}

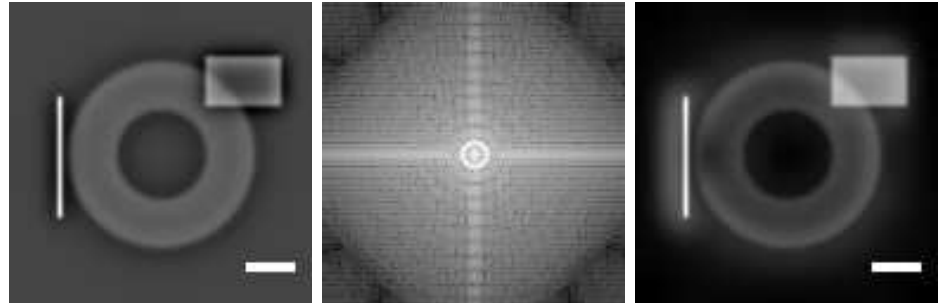
Figure D.4.: Several intermediate results of the algorithm. The scalebar is $2 \mu\text{m}$ wide.

?<fig:hilo1interm>

```

1423 ring=real( ft( besselj(0,2*pi*kc*n.*r))) ;
1424 ring2=r-1./n<kc & r+1./n>kc ;
1425 cring=ring .* ring2 ;
1426 nring=cring ./ sum(cring); % normalized ring with radius kc
1427 eta=sum( abs(kihp) ./ abs(kilp).*nring) ;
1428 i hilo=ift( eta .* kilp+kihp) ;
1429
1430

```



(a) High frequency components I_{hp} of widefield. (b) Combined images \tilde{I}_{hilo} in k-space. (c) Combined section I_{hilo} .

Figure D.5.: More intermediate and the end result of the HiLo local variance estimation algorithm. The white circle in image (b) marks the cutoff frequency k_c of the spatial low pass filter. The scalebars are $2 \mu\text{m}$ wide.

?<fig:hilo1interm2>

1431 Discussion

1432 This algorithm only requires that the illumination intensity in I_n fluctuates over
 1433 a certain region. The results somewhat resemble a sectioned image. The main
 1434 advantage is that all the filtering could have been done in real space, without ever
 1435 doing any Fourier transform.

**1436 Reconstructing the sample illuminated with a grating pattern (single
1437 side-band demodulation)**

1438 The younger paper Santos et al. (2009) uses a more defined pattern in the excitation
1439 illumination than random speckle. A grating is projected into the specimen using
1440 a spatial light modulator.

Starting from a widefield image I_u and an image I_n that has been illuminated with a grating they first determine the ratio $R = I_n/I_u$. With equations (D.2) and (D.3) defining the relationship between in-focus and out of focus light in both images they obtain:

$$R = 1 + CM \sin(\kappa x + \varphi), \quad (\text{D.9}) \{?\}$$

$$C = \frac{I_{\text{in}}}{I_{\text{in}} - I_{\text{out}}}. \quad (\text{D.10}) \{?\}$$

1441 Here C is the local image contrast (containing information similar to c_s in the
1442 HiLo ‘‘speckle’’ method) that is necessary to determine the low-resolution sectioned
1443 image. The Fourier transform \tilde{R} (see Figure D.6(b)) of the ratio contains a peak in
1444 the centre (due to the constant 1) and at least two more peaks (± 1 order) on the k_x
1445 axis. There are a strong ± 1 order and a weaker ± 2 order as a rectangular grating
1446 is imaged into the sample (as opposed to a Sine grating).

1447 To extract the modulated signal a filter is constructed that selects only the first
1448 order on the right side of the Fourier transform. The result of the filter is shown in
1449 Figure D.6(c). The intermediate image $I_{su} = |R^+|I_u$ (see Figure D.7(a)) contains
1450 the low-resolution sectioned image.

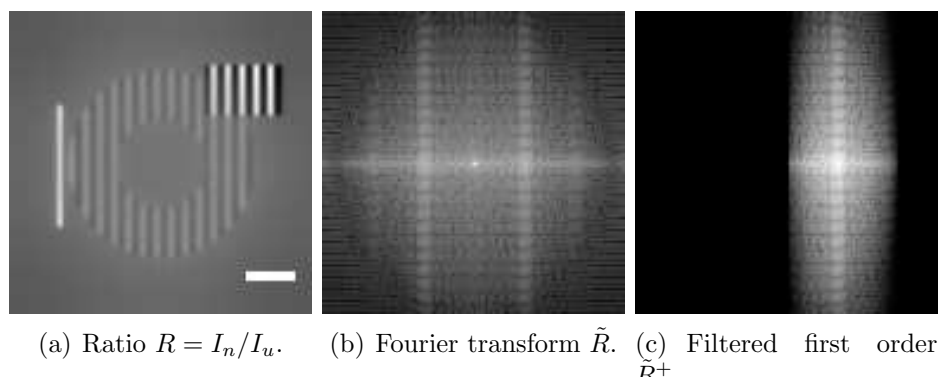


Figure D.6.: Intermediate results for the HiLo single side-band demodulation algorithm. The scalebar in (a) is $2 \mu\text{m}$ wide.

?<fig:hilo2?

1451 The following listing shows the code for the algorithm:

```

1452 si=size(in); n=si(1); r=rr(in, 'freq');
1453 ratio=in./iu;
1454 %% select R+ and construct isu
1455 filter=gaussf((xx(in, 'freq')>0.1) & (xx(in, 'freq')<0.27), 4);
1456 ftratio=ft(ratio);
1457 cm=abs(ift(filter.*ftratio));
1458 isu=cm.*iu
1459 kc=.07; % calculate low pass filtered low-res section
1460 klp=exp(-r.^2/(2*kc.^2));
1461 ilp=real(ift(klp.*ft(isu)));
1462 % calculate high pass filtered high-res section
1463 ihp=real(ift((1-klp).*ft(iu)));
1464 % construct the circle for integration in k-space
1465 ring=abs(ft(besselj(0,2*pi*kc*n.*r)));
1466 ring2=r-1./n<kc & r+1./n>kc;
1467 cring=ring.*ring2;
1468 nring=cring./sum(abs(cring));
1469 eta=sum(abs(ft(ihp))/abs(ft(ilp)).*nring) % integrate along circle
1470 ihi=eta.*ilp+ihp % combined section
1471
1472

```

1473 We chose the cutoff frequency k_c high enough so that I_{lp} doesn't look too smooth
 1474 but also low enough so that I don't lose too much information from the I_{hp} image.
 1475 The scale factor η for I_{lp} and I_{hp} is calculated as in the previous section. Finally
 the combined sectioned image is displayed in Figure D.7(c).

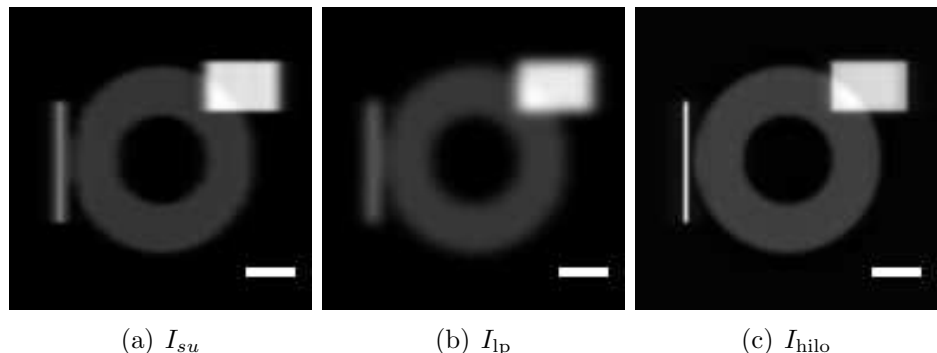


Figure D.7.: Intermediate results and the end result for the HiLo single side-band demodulation algorithm. The scalebars are $2 \mu\text{m}$ wide.

?<fig:hilo2_2>

1477 Discussion

1478 One advantage of the single side-band demodulation method compared to the local
 1479 variance estimation method is that it allows for a higher cut-off frequency k_c without

1480 introducing artifacts in the intermediate image I_{su} . That accounts for the better
 1481 appearance of the result Figure D.7(c) compared to Figure D.5(c) (at least for this
 1482 particular grating).

1483 Another thing that comes to mind is that the calculation of the ratio³ isn't
 1484 the only way to extract the modulated signal. Another approach would involve
 1485 subtracting the widefield image¹ and shifting in Fourier space. This will be discussed
 1486 in the following section.

1487 D.3. Alternative method (subtraction method)

1488 Instead of using a non-hermitian filter to extract the modulated part of the non-
 1489 uniformly illuminated image I_n it is also possible to employ the Fourier shift theo-
 1490 rem: A shift in real space is multiplication with a phase factor in k-space.

Given two images in real space $f(\mathbf{x})$ and $g(\mathbf{x})$. The image g contains the same information as f but shifted by a vector \mathbf{a} . The theorem can be expressed like this:

$$g(\mathbf{x}) = f(\mathbf{x} + \mathbf{a}) \quad \rightarrow \quad \tilde{g}(\mathbf{k}) = e^{i\mathbf{k}\mathbf{a}} \tilde{f}(\mathbf{k}). \quad (\text{D.11}) \{?\}$$

One can find the shift by searching for the maximum $\mathbf{x}_0 = \mathbf{a}$ in the cross-correlation $cov(\mathbf{x})$:

$$cov(f, g)(\mathbf{x}) = \int f(\chi)g(\mathbf{x} + \chi)d\chi = f(\mathbf{x}) \otimes g(-\mathbf{x}) = FT^{-1}(\tilde{f}(\mathbf{k}) \cdot \tilde{g}^*(\mathbf{k})). \quad (\text{D.12}) \{?\}$$

1491 First the uniform image I_u is subtracted from the image with the grating I_n in
 1492 order to suppress the zero order. The following code integrates over a circle around
 1493 the origin in k-space to find a constant **kappa** to scale I_u with. Furthermore the
 1494 Fourier transform of the images is divided by the OTF in order to correct for the
 1495 non-constant frequency transfer in the micro objective²

```
1496
1497 kin=ft(in);
1498 kiu=ft(iu);
1499 % scale kin and kiu so that ic has no zero order
1500 kappa=sum(abs(kin)./abs(kiu).*(rr(in)<5))./sum(rr(in)<5)
1501 %% project otf along z
1502 skpsf=squeeze(sum(kpsf,[],3));
1503 corr=gaussf((rr(skpsf,'freq')<.42),3)./skpsf;
```

¹Suggested by R. Heintzmann.

²Note that for this to work with real noisy data a Wiener filter would be necessary.

D. Implementation of a robust structured illumination reconstruction technique

```

1504 %% correct for the otf
1505 ckin=corr.*kin;
1506 ckiu=corr.*kiu;
1507 %% correlate to find grating positions
1508 ackin=abs(ckin-kappa.*cki);
1509 ackiu=abs(cki).* (rr(ackiu,'freq')<.16 | abs(xx(ackiu,'freq'))<.06);
1510

```

1511 The Fourier transform of the OTF-corrected non-uniform image is shown in Figure D.8(a). It still contains the ± 1 orders. In order to measure their exact position
 1512 (depending on grating period P) the zero order of the widefield k-space is selected
 1513 (in variable `ackiu`) and cross-correlated with `ackin`.

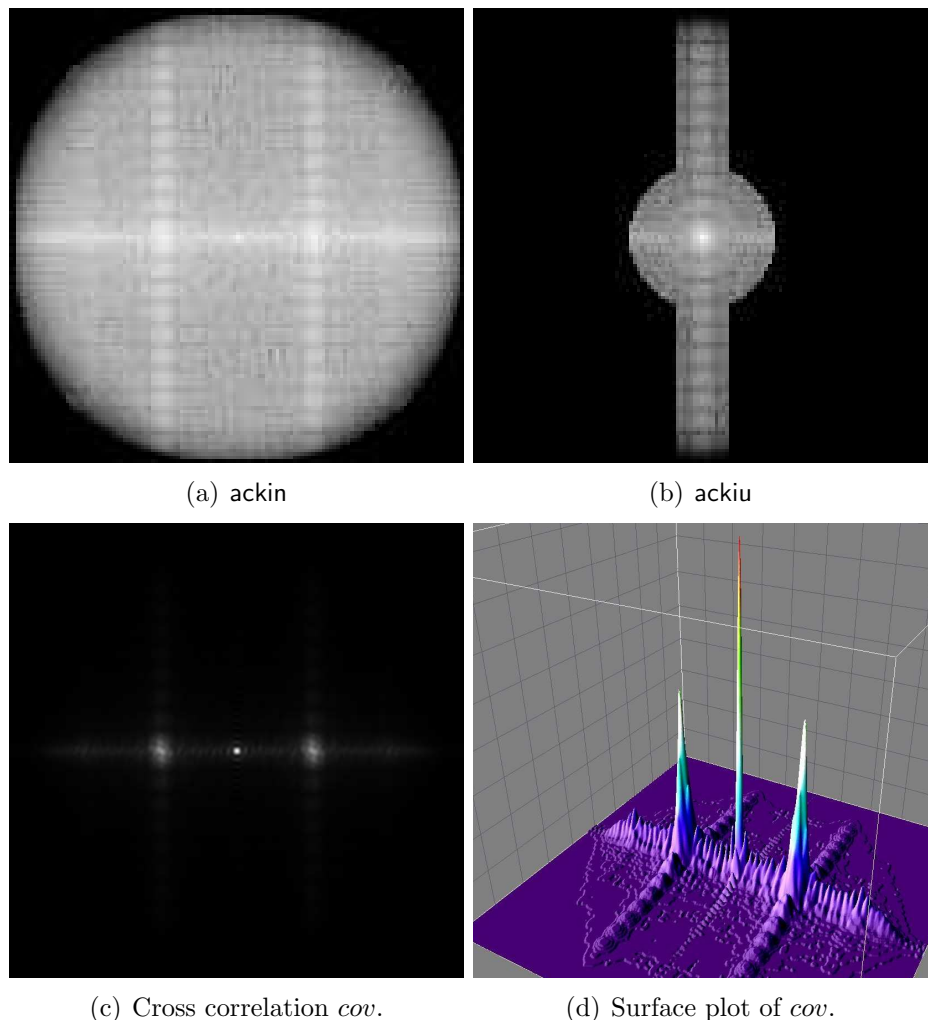


Figure D.8.: Intermediate results for our HiLo “shift” algorithm.

?<fig:hilo3?

1515 In order to locate the maximum in the cross-correlation with a high enough
 1516 accuracy the convolution is done on a finer grid by zero-padding the input images
 1517 as shown in the following listing:

D. Implementation of a robust structured illumination reconstruction technique

```

1518 kcov=ft(ackin).*conj(ft(ackiu));
1519 % subsample the correlation by zero padding
1520 kcov_big=newim(512,512)+i-i; % allocate complex array
1521 st=256-64; w=127; en=st+w;
1522 kcov_big(st:en,st:en)=kcov;
1523 cov=abs(ift(kcov_big)); % this contains the cross correlation
1524
1525

```

1526 The 512×512 image **cov** is shown in Figure D.8(c) and Figure D.8(d). The next
 1527 listing is the code to locate the centre of gravity of the nine points on top of the
 1528 right peak:

```

1529 %% find maximum on the right of the correlation
1530 startx=75*4;
1531 [m, p]=max(abs(cov(startx:end,:)));
1532 pos=[p(1)+startx, p(2)];
1533 % determine center of mass of the 3x3 region around the maximum
1534 region=abs(cov(pos(1)-1:pos(1)+1, pos(2)-1:pos(2)+1));
1535 region=region-min(region);
1536 cm=[sum(xx(region).*region), sum(yy(region).*region)];
1537 shift=(pos+cm-[256,256])/4 % divide by 4 to undo subsampling
1538
1539

```

1540 For the example the displacement **shift** is $(21.25, 0)$ relative to the centre of the
 1541 128×128 image. The following listing shows how the non-uniform image is shifted

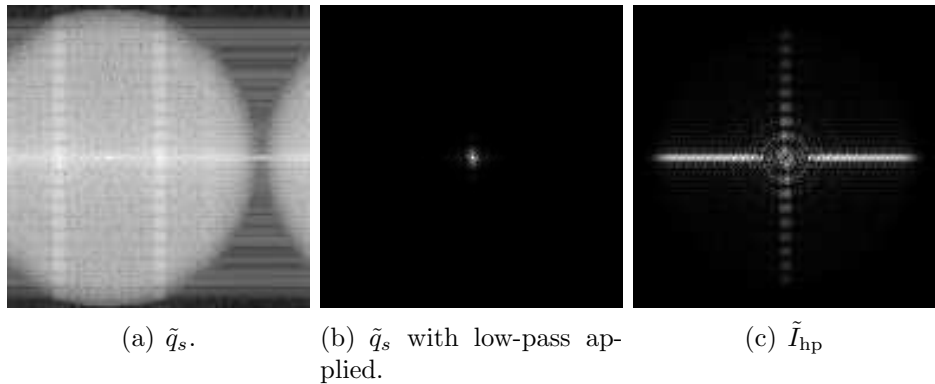


Figure D.9.: The Fourier transform of the shifted zero-order-suppressed non-uniform image q_s with (a) and without (b) low-pass filter and the Fourier transform of the corrected high-pass filtered uniform image (c). As opposed to all other k-space images (b) and (c) are not logarithmic.

?<fig:hilo3_2>

1541
 1542 in k-space so that the first order becomes dc. The result \tilde{q}_s is shown in Figure D.9(a).

1543

D. Implementation of a robust structured illumination reconstruction technique

```

1544 %% multiply by this in object space to shift +1 order into middle
1545 doshift=exp(-i*2*pi*(xx(ckin,'freq').*shift(1)+...
1546     yy(ckin,'freq').*shift(2)));
1547 kc=0.052;
1548 r=rr(ckin,'freq');
1549 klp=exp(-r.^2/(2*kc.^2)); % low pass filter in k-space
1550 q1=ift(ckin-kappa.*cki);
1551 kqs=ft(q1.*doshift);
1552 cm=abs(ift(kqs.*klp));
1553 ihp=real(ift(ft(iu).*corr.*(1-klp)));
1554 % integrate over ring with radius kc to find eta
1555 ring=abs(ft(besselj(0,2*pi*kc*n.*r)));
1556 ring2=r-1./n<kc & r+1./n>kc;
1557 cring=ring.*ring2;
1558 nring=cring./sum(abs(cring));
1559 eta=sum(abs(ft(ihp))/abs(ft(cm)).*nring);
1560 % combine highpass and lowpass filtered images
1561 ihilo3=2.*cm+ihp; % don't use eta
1562

```

1563 The calculation of η gives the value 1.16. It turns out that the reconstructed slice
 1564 (Figure D.10(c)) looks better with a value of $\eta = 2$. This makes sense as the grating
 reduces the illumination power approximately by this factor.

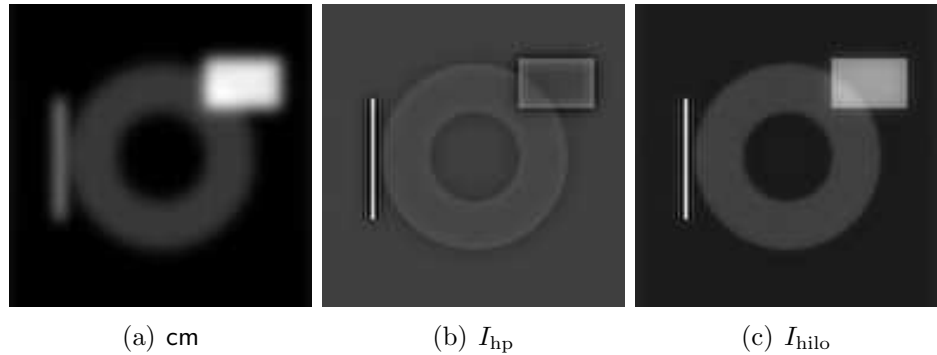


Figure D.10.: Low (a) and high-frequency (b) images in real space and the end result (c).

?<fig:hilo3_3? 1565

1566 Discussion

1567 We believe conceptually the subtraction approach is simpler to understand than the
 1568 single side-band demodulation method.

1569 Indeed, long after this section was devised we found Mertz and Kim (2010), where
 1570 they used a subtraction followed by a rectification $|I_u - 2I_n|$ to partially demodulate
 1571 the signal.

D. Implementation of a robust structured illumination reconstruction technique

₁₅₇₂ As a follow up it might be instructive to investigate the performance of the three
₁₅₇₃ different demodulation approaches in the presence of noise.

E. Wave optical simulation of the spatio-angular microscope

1574

1575

(sec:sim-angle)

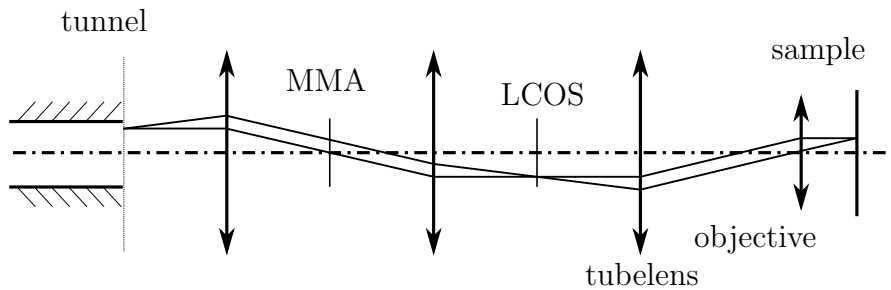


Figure E.1.: Given two masks for MMA and LCoS plane, it is possible to predict the light intensity in the sample by propagating fields from each MMA pixel into sample space and integrating an incoherent sum there.

(fig:memi-simple-app)?

1576 The objective of an optical microscope is defined by its support on the Ewald
1577 sphere, i.e. the set of angles at which k -vectors contribute to the image. In
1578 the following we assume an ideal air objective with unit numerical aperture. This
1579 objective collects all light emitted into one half space and therefore half the Ewald
1580 sphere.

1581 The following code calculates the amplitude point spread function of such an
1582 objective (see Figure E.2 right for a display of its $x - z$ section).

```

1583 n = 128;
1584 nh = n/2;
1585
1586 % generate spherical shell in k-space
1587 a = sinc(rr(n,n,n));
1588 ka = ift(a);
1589
1590 % select top of the shell (NA=n):
1591 ke = ka * (zz(ka)<0);
1592

```

E. Wave optical simulation of the spatio-angular microscope

```

1593 % show kx-kz section of ewald-sphere
1594 ke(:,nh,:)

1595
1596 e = ift(ke);
1597
1598 % xz section of electric field
1599 e(:,nh,:)

```

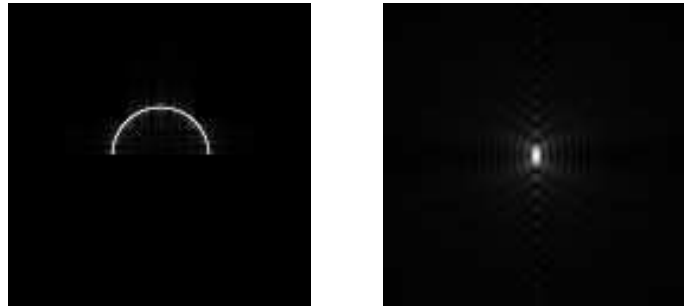


Figure E.2.: **left:** $k_x - k_z$ section of the Ewald sphere – the k -vectors that can traverse the objective lens. **right:** $x - z$ section of electric field in sample space (amplitude point spread function).

`(fig:simple-apsf)`

1600 If the microscope would contain no MMA but just the LCoS being illuminated by a
 1601 parallel plane, then the 3D field distribution in the sample plane could be obtained by
 1602 propagating the field from the LCoS plane into the back focal plane of the objective (by a
 1603 single 2D Fourier transform). Then one multiplies each of the points of the Ewald sphere
 1604 with the corresponding complex value of the illumination field. A 3D Fourier transform
 1605 then results in the 3D field distribution within the sample. By calculating the absolute
 1606 square of the field one obtains the 3D light intensity distribution in sample space.

1607 In the case of our spatio-angular microscope each of the pixels of the MMA can be
 1608 assumed to be an independent coherent source. In the following code their fields are sepa-
 1609 rately propagated into sample space and then incoherently summed into the 3D intensity
 1610 distribution.

1611 The right picture in Figure E.4 displays an $x - z$ section of the intensity distribution
 1612 for the masks shown in in Figure E.3. Note that the MMA window is shifted slightly to
 1613 the right. The intensity distribution clearly shows that some angles are missing.

```

1614 % define rectangular window as an lcos pattern
1615 lcx = 0;
1616 lcy = 10;
1617 lw = 32;
1618 lh = 32;

```

E. Wave optical simulation of the spatio-angular microscope

```

1619 lsx = lcx-lw/2;
1620 lex = lcx+lw/2;
1621 lsy = lcy-lh/2;
1622 ley = lcy+lh/2;
1623 lcos= lsx<=xx(n,n) & xx(n,n)<lex & lsy<=yy(n,n) & yy(n,n)<ley
1624
1625 % define a circular window as an mma image (with quite low resolution)
1626 mmazoom = 4;
1627 mman = n / mmazoom;
1628 mma = (xx(mman,mman)-3)^2+(yy(mman,mman)-0)^2 < 4^2

```

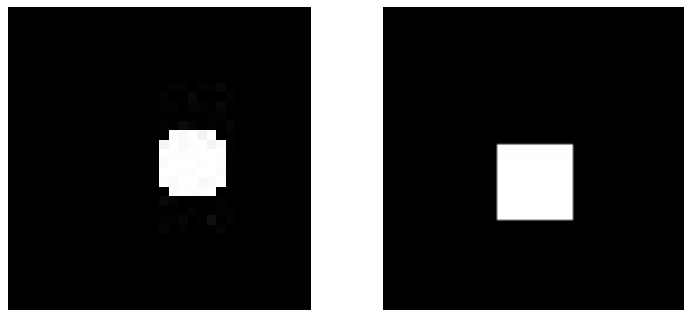


Figure E.3.: **left:** circular MMA window with 45 “on” pixels. **right:** Rectangular mask for LCoS.

`<fig:mmma-lcos-window>`

```

1629 intens = newim(n,n,n);
1630 % visit each point in the mma image
1631 for i=0:mman-1
1632     for j=0:mman-1
1633         if mma(i,j)
1634             rphase=newim(n,n);
1635             rphase(mmazoom*i,mmazoom*j) = 1.0;
1636             % create corresponding illumination direction on lcos plane
1637             bfp=ft(lcos .* ift(rphase));
1638             field=ift(repmat(bfp,[1 1 n]) .* ke);
1639             % accumulate intensity image (incoherent)
1640             intens = intens+field.*conj(field);
1641         end
1642     end
1643 end
1644
1645 intens(:,:,nh,:)

```

E. Wave optical simulation of the spatio-angular microscope

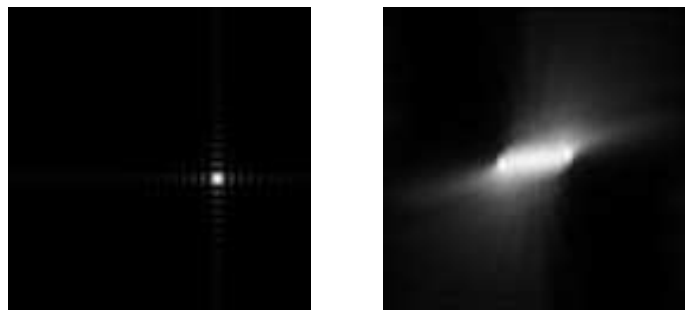


Figure E.4.: **left:** BFP image for one particular of the “on” MMA pixels. **right:** $x - z$ section through the intensity distribution in sample space.

`<fig:sim-bfp-intens>`

1646 **F. MEMI optical system**

F. MEMI optical system

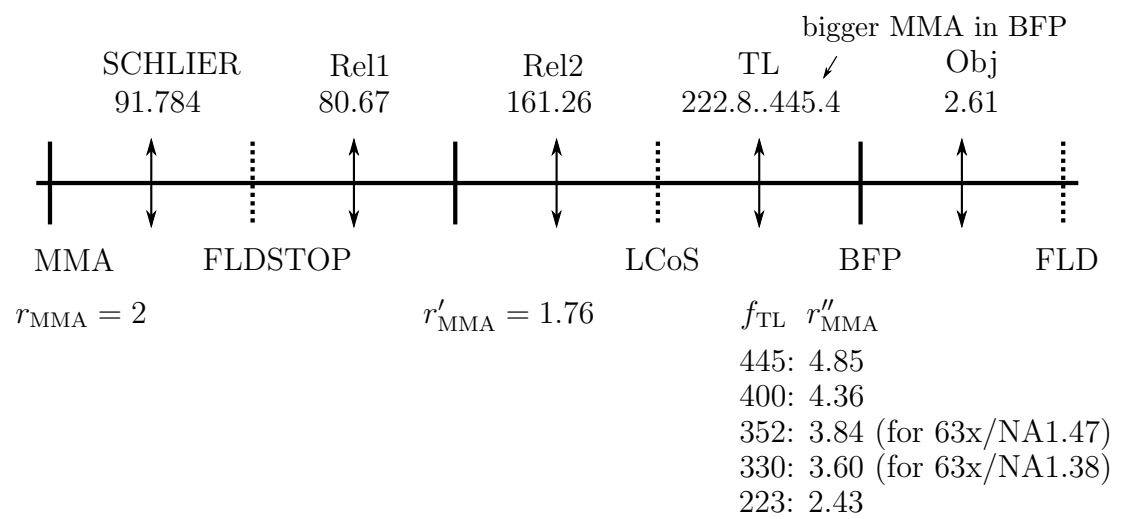


Figure F.1.: Schematic of the lenses in the MEMI system and their focal lengths. The focal length f_{TL} of the tubelens can be varied. This allows to scale the second intermediate image r''_{MMA} of the micro mirror array to fit the back focal plane of different objectives. Dimensions in mm.

(fig:memi-sketch)

G. Experiments with DVI LCoS

?<sec:dvi>?
Initially we strived to create a prototype, that would allow feedback between
the spatial SLM and the camera with 60 Hz. It was based on a fast ferro-
electric liquid crystal on silicon device with DVI (digital video interface) data
input as the spatial SLM.

We overcame several problems with synchronization, latencies and light ef-
ficiency. Finally the remaining problems turned out to be too difficult to
overcome¹ and we rather switched to a spatial SLM solution with local stor-
age as described in the main body in this work.

Nevertheless we believe spatio-angular illumination with realtime control will
be very useful and therefor we describe our system, even though it is imprac-
tical for now.

G.1. Description of the setup (fast MMA)

The optical setup is the same as in Figure 3.3. Sometimes we use a blue LED diode array (CoolLed) instead of the laser as a light source, that we couple with a fibre bundle into the integration tunnel. The LED delivers less brightness but a more uniform illumination – especially of the MMA.

The ferroelectric LCoS display is nearly identical to the one used in the main text (SXGA R3, ForthDD) but the data is transferred into the controller from the computers graphics card via DVI. The computer transmits digital 24-bit images (1280×1024 pixels) with 60 Hz². The LCoS controller then displays a sequence of 24 bitplanes. Each bitplane is shown for $276.27 \mu\text{s}$ as indicated in the RED-ENABLE signal in Figure G.1.

Originally the LCoS controller was designed by ForthDD to display colour images with 8 bits per colour. In order to do this it would display three times eight images of pulses, where each pulse would be half the length of its predecessor. Three separate

¹Retrospectively, there seems to be a solution which we mention in the discussion to this section.

²Up to 85 Hz are supported by the ferroelectric LCoS. This corresponds to a frame rate of $24 \times 85 \text{ Hz} = 2040 \text{ Hz}$ of individual bit planes.

1673 galvanically decoupled TTL signals would then enable corresponding LEDs for red,
1674 green and blue. We use the controller in a modified mode (48366 BitSlice 768-line
1675 60Hz V1.0), where it would display each bitplane for equal amounts of time and
1676 generate all light enable pulses on RED-ENABLE.

1677 Unfortunately the company doesn't provide the vertical sync signal (which is gen-
1678 erated by the graphics card in the computer). As a remedy we use a microcontroller
1679 (Arduino) program (see code listing on page 98), that reads the RED-ENABLE sig-
1680 nal, counts the pulses and measures the time between them. This way we are able
1681 to find the longer gap of $587\ \mu s$ in front of the first pulse (which corresponds to bit
1682 0 of the red byte).

1683 Initially we planned our device to run at the fastest possible speed. The MMA has
1684 a delay of $850\ \mu s$ between receiving a trigger edge and the mirrors having settled in
1685 the requested orientation. In order to run the MMA at a fast frame rate we decided
1686 to generate a trigger pulse in the Arduino microcontroller after every second LCoS
1687 bitplane³. This gives enough time to the MMA controller to set the mirrors and
1688 we can display simultaneous images on MMA and LCoS during 11 out of 24 LCoS
1689 bitplanes. The system therefore achieves a frame rate of $60\text{ Hz} \times 11 = 660\text{ Hz}$ and a
1690 duty cycle of just $277\ \mu s \times 11 \times 60\text{ Hz} = 0.18$.

1691 **G.1.1. On using OGP1 as graphics hardware**

1692 Using a graphics card to generate the images for the LCoS is a non-optimal solution.
1693 A normal graphics card can't be externally triggered. This means we can no longer
1694 have the slowest device (the camera) as the master for synchronization and things
1695 will be either slow or inflexible. Therefore we obtained a FPGA based graphics card
1696 (the OGP1 from the open graphics project) which in principle could be modified to
1697 generate the image, when requested. As it is still in development stage its features
1698 were not fully developed. At the time we were able to bring an image onto the
1699 LCoS but changing the content of the video memory was rather slow (in the range
1700 of hundreds of milliseconds) because it had to be done by direct access and drawing
1701 operations or bit block image transfer had not been implemented.

1702 Later we learned from the manufacturer of the LCoS (ForthDD) that varying the
1703 framerate at the DVI input would probably anyway not work.

³Note that microcontroller programming for synchronization requires a peculiar style. One must be careful about conditionals and loops. In order to have predictable pulse generation make sure each code path is run in the same time. It is best to unroll loops in order to prevent their initial overhead. Therefore we often generate these programs with another program.

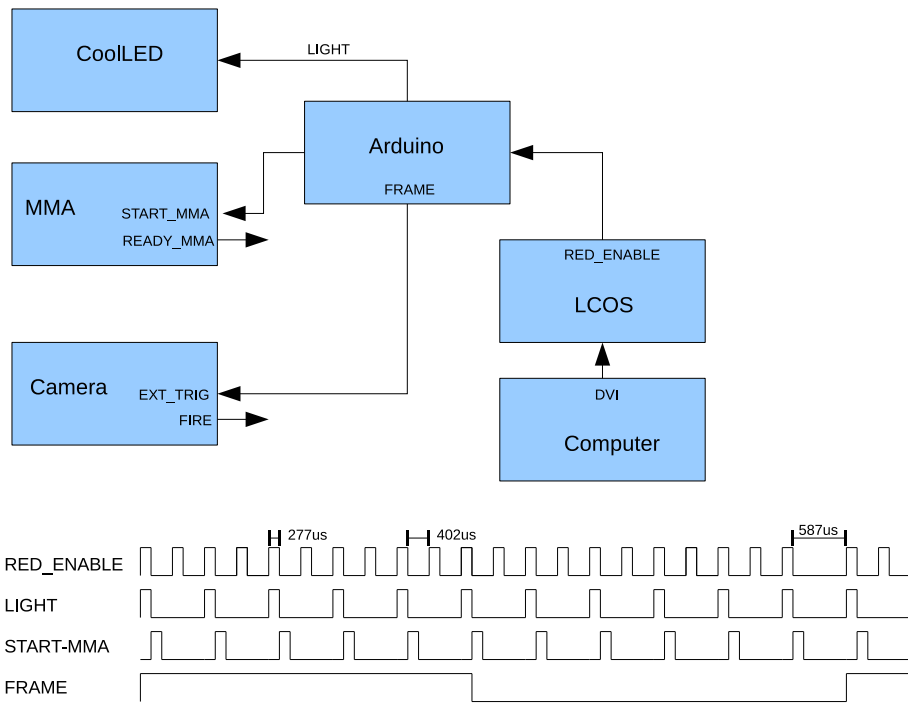


Figure G.1.: **top:** Schematic of the electronic components of the system for the “fast MMA” trigger scheme. **bottom:** Depiction of TTL trigger signals for this configuration. The RED-ENABLE signal is high, when the LCoS displays a bitplane. LIGHT enables the laser and START-MMA triggers the MMA, which displays an image after a delay of $850\ \mu\text{s}$. The signal FRAME indicates the beginning of video frames and is necessary to start camera exposures at the right time.

{fig:trigger0}

1704 **G.2. Description of the trigger generation (slow**
1705 **MMA)**

sec:dvi_slow 1706 We should note, that the MMA is a prototype as well and its controller, though being
1707 connected to the computer via Ethernet, doesn't provide 1 Gbit/s communication
1708 or any other means that would allow realtime update of its image, e.g. support for
1709 run-length encoding of the image data. Therefor the MMA can display images with
1710 660 Hz but uploading one new image roughly takes 80 ms.

1711 It therefor seems reasonable to switch to a different triggering scheme, where the
1712 mirrors of the MMA are tilted for one full video frame. The MMA has a limited
1713 maximum duty cycle of 50%. This means we have to drop every other frame from
1714 the graphics card. If camera exposure times of 16.66 ms are sufficient, we have even
1715 doubled the duty cycle of the full system to $277\ \mu\text{s} \times 23 \times 60\ \text{Hz} = 0.38$. Note that
1716 we loose the first bitplane due to the MMA's $850\ \mu\text{s}$ load delay.

G. Experiments with DVI LCoS

1717 The z-stage of the microscope can perform $1\text{ }\mu\text{m}$ steps in 20 ms. Therefor dis-
 1718 playing two black images on the LCoS (and capturing one of them) is sufficient to
 1719 ensure that the stage is at the next position.

1720 The following code listing shows the Arduino microcontroller program, that re-
 1721 covers the vsync signal from the pulse train on the RED-ENABLE signal from the
 1722 LCoS controller it generates pulses with 60 Hz on pin 13 that synchronize the MMA
 1723 controller.

`<fig:arduino-vsync>`

```

1724 // takes the lclos signal (train of 24 pulses, followed by a pause)
1725 // and generates a trigger signal for the mma at the end of each train
1726 // so for every DVI image (consisting of 24 bit planes) a different
1727 // mma image can be shown.

1728
1729 volatile unsigned int Ticks;      // holds the pulse count as .5 us ticks
1730 // pin 8 takes signal from lclos
1731 char icpPin = 8;                // this interrupt handler must use pin 8
1732 volatile char bit_plane_change = 0; // incremented whenever a
1733                                         // different bitplane is displayed
1734 char mma = 13;                  // output towards mma

1735
1736 ISR (TIMER1_CAPT_vect) // interrupt gets called when pin 8 changes
1737 {
1738     if (!bit_is_set (TCCR1B, ICES1)) // was rising edge detected?
1739         TCNT1 = 0;           // reset the counter
1740     else {                 // falling edge was detected
1741         Ticks = ICR1;
1742         if (Ticks > 1000) {
1743             bit_plane_change = 0;
1744         }
1745     }
1746     TCCR1B ^= _BV (ICES1); // toggle bit value to trigger on the
1747                             // other edge
1748     if (bit_plane_change == 47) {
1749         digitalWrite (mma, HIGH);
1750     }
1751     else if (bit_plane_change == 0) {
1752         digitalWrite (mma, LOW);
1753     }
1754     bit_plane_change++;
1755 }
```

G. Experiments with DVI LCoS

```

1756 void setup ()                                // run once, when the sketch starts
1757 {
1758     pinMode (icpPin, INPUT);
1759     pinMode (mma, OUTPUT);
1760     TCCR1A = 0x00;      // COM1A1=0, COM1A0=0 => Disconnect Pin OC1
1761                     // from Timer/Counter 1
1762                     // PWM11=0,PWM10=0 => PWM Operation disabled
1763     TCCR1B = 0x02;      // 16MHz clock with prescaler means TCNT1
1764                     // increments every .5 uS (cs11 bit set)
1765     Ticks = 0;          // default value indicating no pulse detected
1766     TIMSK1 = _BV (ICIE1); // enable input capture interrupt for timer 1
1767 }
1768 int getTick ()
1769 {
1770     int akaTick;      // holds a copy of the tick count so we can
1771                     // return it after re-enabling interrupts
1772     cli ();           // disable interrupts
1773     akaTick = Ticks;
1774     sei ();           // enable interrupts
1775     return akaTick;
1776 }
1777 char get_plane_change ()
1778 {
1779     int aka;
1780     cli ();
1781     aka = bit_plane_change;
1782     sei ();
1783     return aka;
1784 }
1785 void loop () {}

```

1786 Eventually, with generous support by a ForthDD engineer, we found a way to
1787 access the vsync signal on the LCoS controller board, making the above program
1788 obsolete. However, the process involved producing our own circuit board because
1789 we needed to connect with an obscure SMD size board to board connector and
1790 provide our own means of galvanic isolation. Microcontroller programs, similar to
1791 the one above, have since then proved quite useful to other members in our lab.

G. Experiments with DVI LCoS

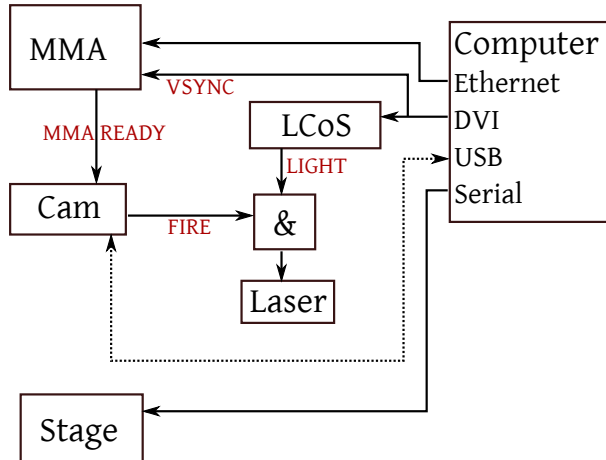


Figure G.2.: Schematic of the electronic system for the “slow MMA” trigger scheme. The graphics card in the computer is the master. It generates images on the LCoS with 60 Hz. The LCoS defines when the light can turn on but the Laser is only enabled, when the camera is integrating as well. The MMA selects only every second video frame from the graphics card and notifies the camera, when it has deflected its mirrors. The z-stage is controlled by the computer from within the display loop for the graphics card (synchronized with the signal VSYNC).

?<fig:09trigger>?

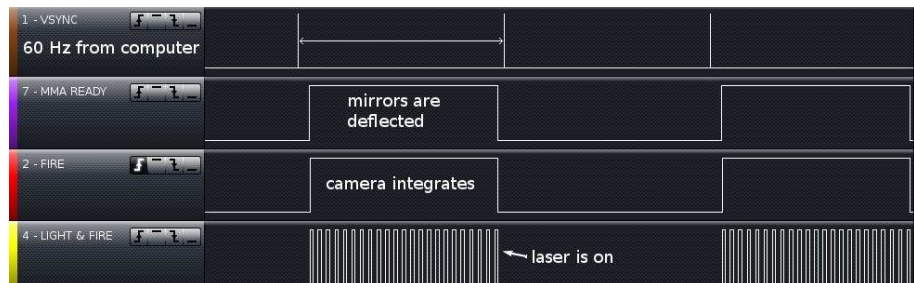


Figure G.3.: Snapshot of the trigger signals for the “slow MMA” configuration with a logic analyzer (Saleae Logic). The LCoS is the master, every second frame from the graphics card is integrated by the camera (which is running at 30 Hz). The MMA has its mirrors tilted when the camera integrates, due to the delay of 850 μ s the first image from the LCoS isn’t collected in the exposure.

:screen_logic_labels)?

1792 G.3. Verification of the synchronization

- 1793 In order to verify that the system is working, the graphics card is displaying images
- 1794 with counters that incremented every frame (see Figure G.4). As only every second
- 1795 image is captured one would expect only odd counter numbers on the camera.
- 1796 However, every 400 (or so) images a jump of on or more frames occurs. This

G. Experiments with DVI LCoS

1797 problem can be traced back to the Steel Banks Common Lisp⁴ garbage collector.
 1798 A garbage collection can take up to 80 ms, which is not sufficient for the required
 1799 update rate of 16 ms. Porting the code to C fixes this issue.

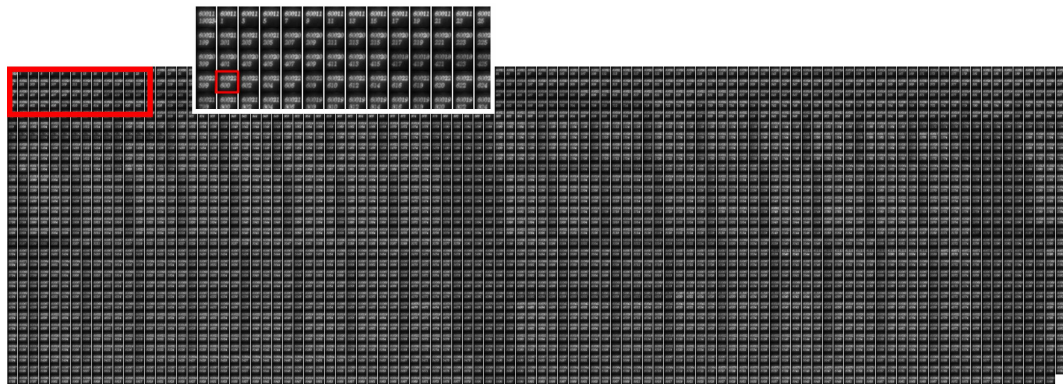


Figure G.4.: Montage of many camera images captured in sequence. The LCoS was showing two frame counters. The bottom of the two numbers is reset at the beginning of the experiment and therefore counts 1, 3, 5, By design only every second image is captured. Occasionally a jump in the numbers was observed (see marked image) when the garbage collector ran. This was fixed by porting the code to C.

`ig:fast4-no-first_cut)`

1800 The system was now able to capture images with a rate of 30 Hz with a constant
 1801 integration time of 16 ms. An experiment has been devised, that can capture stacks
 1802 of sectioned data. In this acquisition protocol the MMA is not used for angular
 1803 control. It just displays white images and every fourth image a black image. The
 1804 LCoS displays three phases of a vertical grating and a black image. When both
 1805 displays show the black image, the stage moves to the next slice. Capturing the
 1806 slice and moving $1\mu m$ takes eight video frames. A stack with 10 slices can be
 1807 acquired in 1.3 s. Figure G.5 left shows images of a 3D distribution of $2\mu m$ beads
 1808 in agar acquired with this imaging protocol.

1809 The right mosaic in Figure G.5 shows a reapplication of the same acquisition
 1810 protocol. However, there the devices didn't start exactly at the same time. Maybe
 1811 one in seven experiments, the acquisition is successful. Trying to debug this problem
 1812 proves difficult.

1813 On the one hand the camera doesn't provide time stamps, which would be helpful
 1814 to measure the latency between issuing the `StartAcquisition` command and when the
 1815 camera actually starts integrating. The same is true for the MMA. There is no

⁴We used Common Lisp to develop most of our system. The main reason being an 8 s initialization time in our camera's (Andor Clara) driver, that can't be disabled and hinders the C style edit-compile-run cycle.

specification of how long SLM-SetStartMMA or SLM-SetPictureSequence take and when the next incoming trigger is processed.

One solution to the problem would be to display a sequence of patterns in the beginning of each experiment that would allow the system to recover the offset between the devices. An example pattern could be five white images on the MMA (++++), two dark double images on LCoS, one dark LCoS double image, two dark LCoS double images (---+--).

By analyzing the camera images one could then recover when the bright image arrived. The same procedure could be applied for the MMA as well. In that case we would display ++++ on the LCoS and ---+-- on the MMA. This solution is rather cumbersome. Therefor we didn't try it and replaced the LCoS with one that contains local storage.

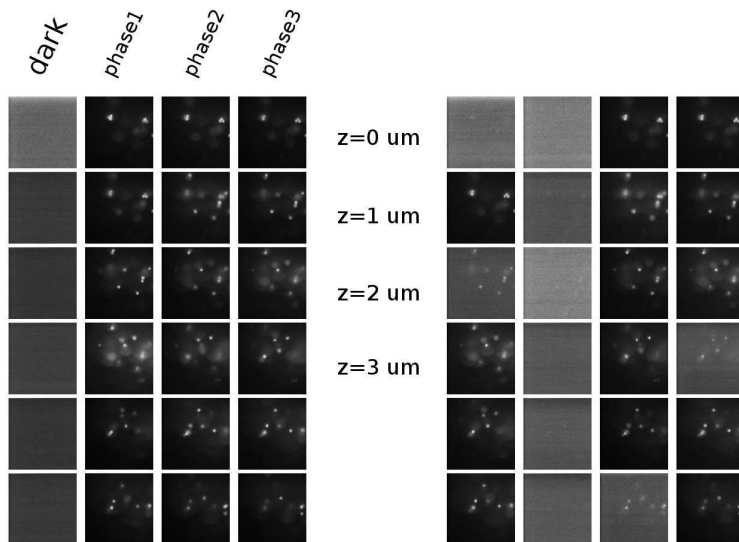


Figure G.5.: **left:** Sequence of images that was acquired while LCoS, MMA, z-stage and camera are running in sync. The camera is constantly running at 30 Hz and the stage moves while a black mask is displayed on the MMA as well as the LCoS. The sample is a $2 \mu\text{m}$ yellow-green beads in agar **right:** Same sequence of images should be displayed but the devices (camera, MMA and LCoS) do not start at the same time.

(fig:dvi-mosaic)

1828 G.4. Conclusion

The approach of sending data from the computer graphics card to the LCoS by DVI would have its advantages but a synchronized start of camera, MMA and LCoS proved to be too difficult or impractical.

G. Experiments with DVI LCoS

1832 If there was one display less, the approach would work perfectly fine. Indeed we
1833 planned to build the optics using a spherical mirror and bring conjugate planes of
1834 the pupil and the field (angular and spatial control) next to each other on one LCoS.

1835 We could have investigated the synchronization problem (e.g. camera time stamps)
1836 further by sniffing data on the USB stack using the tool Wireshark.

1837 Another approach to solving the problem, is to generate a trigger pulse from
1838 within the frame rendering loop in the computer software. This pulse could ensure
1839 that all devices start running with the same video frame.

H. Shearing interferometer-based intensity modulation with a MEMS mirror device

Here we describe an alternative approach to turn the micro mirror array, which acts as a phase device, into a intensity spatial light modulator.

H.1. Introduction

One of the main partners of the MEMI project is Fraunhofer IPMS (Dresden, Germany). Before being part of the MEMI project, they developed a micro mirror array (MMA) which with optimized reflectivity in the ultra violet wavelength range (generation-0). The application of this device mainly being semiconductor manufacturer.

During the MEMI project, they developed a new version of the MMA (generation-2) that can be used up to near infra red wavelengths. Initially Fraunhofer provided generation-0 MMA's to the project partners. From the beginning of the project a

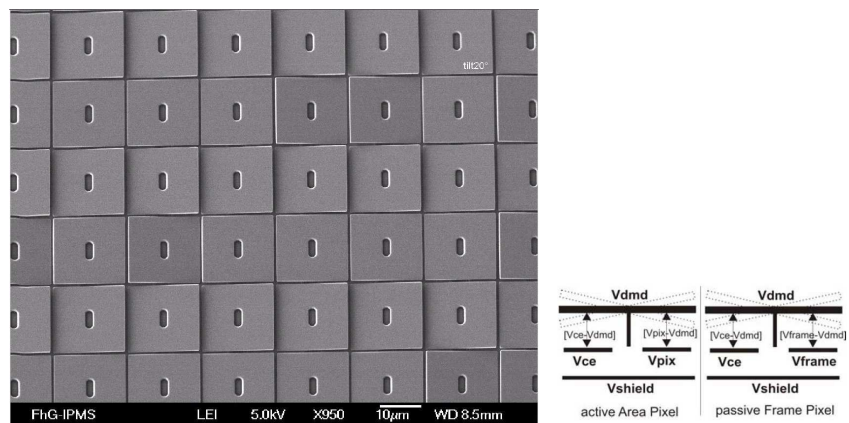


Figure H.1.: **left:** Electron micrograph showing generation-2 MMA with tilted mirrors. **right:** Schematic of the voltages on one mirror (both figures by Fraunhofer IPMS).

?<fig:mmma-tilts?

1853
1854 Fourier filtering-based approach was planned in order to turn the minute tilts of the
1855 micro mirrors into intensity modulations: An aperture is placed on the zero order
1856 of the Fraunhofer diffraction pattern of the MMA. When mirrors are tilted, they
1857 reflect the light outside of the aperture, where it will be absorbed. This technique
1858 has been applied for the generation-0 MMAs. As long as the diffraction efficiencies
1859 are sufficient, it functions for multiple wavelengths.

1860 However, the Fourier filtering approach has the drawback, that illumination an-
1861 gles and the size of the aperture are limited by the diffraction angles of the MMA.
1862 In our optical system this limits the area on the LCoS, that can be illuminated and
1863 therefor the field of view in the specimen.

1864 A shearing interferometer-based approach was suggested instead. There, the
1865 images of neighbouring mirrors are overlapped and can interfere. A system based on
1866 Wollaston (or Nomarski) prisms would give better angular acceptance. It promises
1867 good contrast and will work for multiple wavelengths as well.

1868 H.2. Description of the setup

1869 Figure H.2 shows a schematic and a photograph of the setup. The light source is a
1870 liquid light guide-coupled 480 nm LED (CoolLed). It illuminates a square integra-
1871 tion rod (10 cm length) to provide a uniform light distribution in the conjugate F''
1872 of the field.

1873 The optical path for the illumination contains two apertures to confine the field
1874 and to control the illumination angles. We use a wire grid polarizer (Moxtek, UT,
1875 US) as polarizing beam splitter.

1876 Achromatic doublets were used as the two imaging lenses.

1877 The position of the focal plane of the Nomarski prisms was estimated by measur-
1878 ing the distance between the prism and the back focal plane of the matching micro
1879 objectives (the result is generally 2 – 3 cm). For the fine adjustment the prism is
1880 axially shifted until the dark band encompasses the full field of view.

1881 We selected the prism with the biggest split angle ($\theta = 0.078$ mrad, see section
1882 H.4.1 for the measurement; matching a $63 \times /1.4$ oil immersion objective) in order
1883 to keep the distances small and minimize beam distortion due to air fluctuations.
1884 Later we found that the size of the prism is the limiting factor. For a good DIC
1885 effect at least three orders of the MMA diffraction pattern have to pass through the
1886 prism. To ensure this, two identical DIC prisms were used sequentially. Note that
1887 the distance between the prisms allows to vary the split angle (Schwertner et al.

H. Shearing interferometer-based intensity modulation with a MEMS mirror device

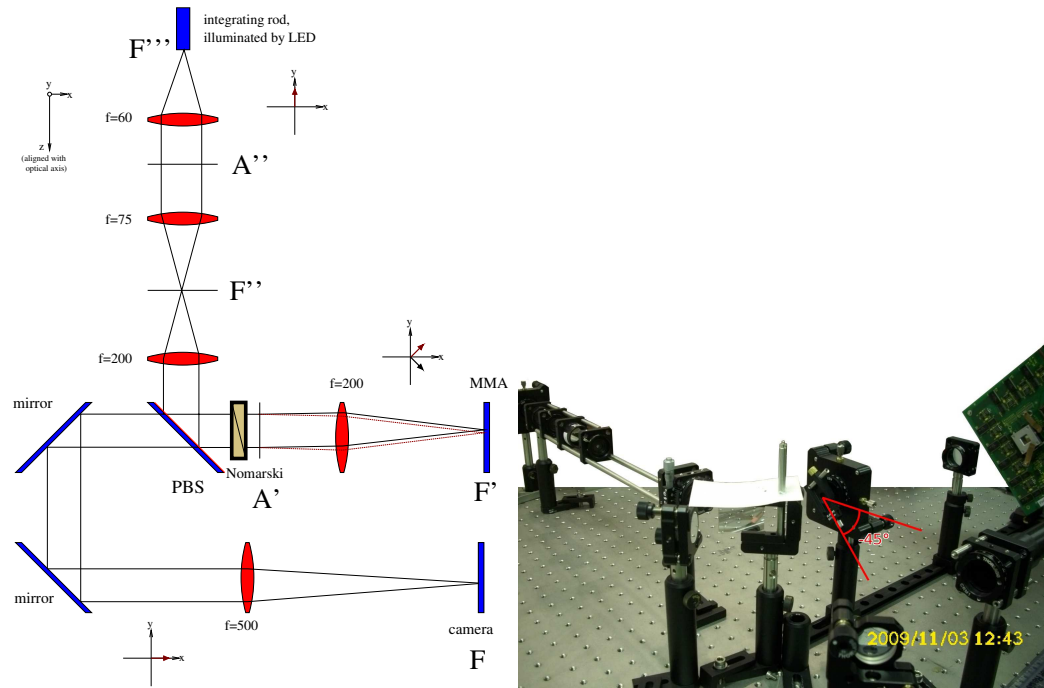


Figure H.2.: Schematic and photograph of the optical setup. **left:** Apertures allow control of the illumination in the planes A'' and F'' . The wire grid polarizing beam splitter (PBS) is oriented with the aluminium structured side towards the Nomarski prism. The Nomarski prism can be rotated around the optical axis. Given the orientation of the MMA, the DIC method only works for $\pm 45^\circ$ and $\pm 135^\circ$ settings. **right:** Nomarski prism is oriented in -45° direction. A white paper card protects the wire grid polarizer from dust. This setup contains two additional cleanup polarizers that are not shown in the schematic in.

`(fig:dic_mma)`

1888 2008).

1889 The objective lens and the MMA are positioned on a rail to simplify focusing.
 1890 The lens positions were pairwise adjusted by sending a plane wave of a green laser
 1891 through each “telescope” and moving one lens until the outgoing wave was plane
 1892 (using a shear plate). The distance of tube lens and camera was set to the focal
 1893 length by reflecting a parallel beam into the tube lens and minimizing the size of
 1894 the spot on the camera.

1895 **H.3. Displaying arbitrary gray values using the DIC approach**

First we consider a simplified arrangement of one piston micro mirror of width Λ on a plane mirror (see Figure H.3). Let $k = 2\pi/\lambda_0$ with vacuum wavelength λ_0 . We

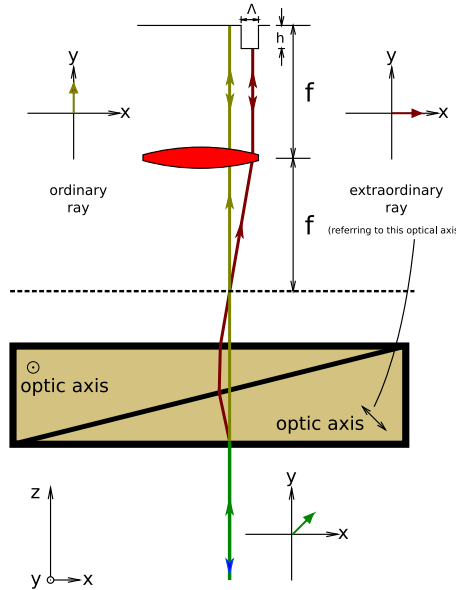


Figure H.3.: Linearly polarized light is split by the prism into two rays with slightly diverging angle. They hit the MMA at two spots, which are one shearing distance apart. The light returning through the Nomarski prism has different polarization states depending on the height difference h of the mirrors at those two beam positions.

`(fig:prism)`

write the influence of a retarder (the height difference h of the small piston mirror) on a polarized wave in Jones calculus as (Goodman (1996) p. 418):

$$L_r(\Delta) = \begin{pmatrix} 1 & 0 \\ 0 & e^{-i\Delta} \end{pmatrix} \quad (\text{H.1}) \{?\}$$

with a phase difference $\Delta = 2kh$ (the factor 2 due to the reflection). The matrix for a polarizer that passes the component of the electrical field which is linearly polarized at an angle α to the x-axis is:

$$L_p(\alpha) = \begin{pmatrix} \cos^2 \alpha & \sin \alpha \cos \alpha \\ \sin \alpha \cos \alpha & \sin^2 \alpha \end{pmatrix}. \quad (\text{H.2}) \{?\}$$

In our setup the incoming light has a 45° polarization $\mathbf{U} = (1, 1)^T / \sqrt{2}$ after the first reflection on the PBS. The light passes through the Nomarski prism and is reflected by the MMA. Here depending on the mirror height a phase retardation is imposed on one of the two beams. The reflected light is recombined in the Nomarski prism and only the component that is polarized at $\alpha = -45^\circ$ passes through the PBS onto

the camera: $\mathbf{U}' = L_p(-45^\circ)L_r(\Delta)$.

$$I' = |\mathbf{U}'|^2 = (1 - \cos \Delta)/2 \quad (\text{H.3}) \{?\}$$

The camera image is dark for a plane mirror and is maximal for a piston height $h = \lambda/4$. For a piston mirror of width Λ the intensity of the corresponding pixel on the camera is (assuming it receives all the light from one mirror):

$$I_p = \int_{-\Lambda/2}^{\Lambda/2} I'(\Delta(x')) dx' = \frac{\Lambda}{2}(1 - \cos \Delta). \quad (\text{H.4}) \{?\}$$

As the mirrors of the MMA tilt (and don't move like pistons) it is necessary to

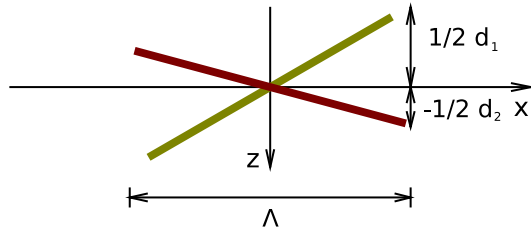


Figure H.4.: Two mirrors that tilt with different deflections d_1 and d_2 in opposite directions. The pitch of the mirrors is Λ .

`(fig:tilt)`

integrate along the DIC shift direction x' to get the brightness of one pixel depending on the tilt of the two neighbouring mirrors (this calculation is done for small mirror tilts, see Figure H.4):

$$I_t = \int_{-\Lambda/2}^{\Lambda/2} I'(\Delta(x')) dx' = \frac{\Lambda}{2} \left(1 - \frac{\sin(k\Delta d)}{k\Delta d} \right). \quad (\text{H.5}) \boxed{\text{eqn:it}}$$

1897 Here $\Delta d = d_1 - d_2$ is the difference between the deflections d_1 and d_2 of the two
 1898 mirrors and Λ is the mirror pitch (see Figure H.4). Note that the integral sums
 1899 incoherently across the mirror because in our experiment we use a LED light source.
 1900 Note that the DIC image of torsion mirrors is in general not constant over the width
 1901 Λ of one mirror. Neighbouring mirrors do not differ in their height at the positions
 1902 where they are fixed. Therefor there will always be a dark stripe in the centre of
 1903 the mirrors. This artifact wouldn't occur with piston style mirrors.

The scale factor of I_t is arbitrary. In order to get a more useful result we compare the brightness of MMA mirrors I_t to a theoretical device consisting of pistons that

can move the distance d away from the equilibrium position:

$$\eta(\Delta d) = \frac{I_t}{I_p} = \frac{1 - \sin(k\Delta d)/(k\Delta d)}{1 - \cos(2kd)}. \quad (\text{H.6}) \quad \text{?eqn:eta?}$$

The data sent to the generation-0 MMA are integers $q \in [0, 255]$ that set the voltage

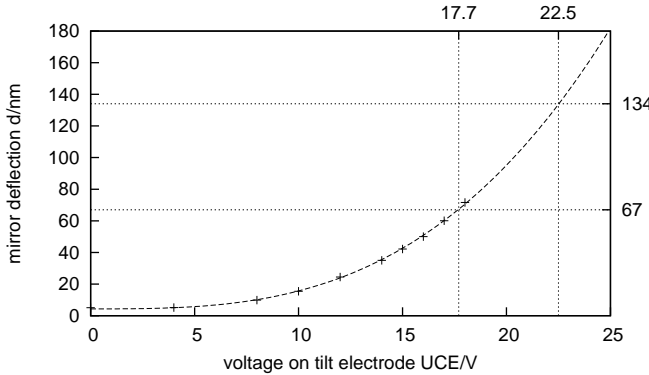


Figure H.5.: Deflection curve for our generation-0 MMA sample (data supplied by Fraunhofer IPMS) and corresponding fit of cubic polynomial $d = a \cdot x^3 + b$ with $a = (0.01136 \pm 0.0001) \text{ nm V}^{-3}$ and $b = (4.32 \pm 0.3) \text{ nm}$. The x-axis is the voltage U_{CE} that is applied to one of the electrodes of the mirror and the y-axis shows the deflection d of the mirror (distance from mirror edge to the equilibrium position). The maximum voltage that we apply to the mirrors in our experiments is 22.5 V.

(fig:deflection)

of the counter electrode U_{CE}

$$U_{CE}(q) = s_{\text{img}} \cdot 30 \text{ V} \cdot \frac{q}{255}. \quad (\text{H.7}) \quad \{\text{?}\}$$

The scale factor s_{img} is 0.75 in our experiments. Fraunhofer provides a transfer function for the MMA that describes the relation between the voltage and the deflection (see Figure H.5) from 0 to $U_{CE} = 18 \text{ V}$. They also request, not to use any voltages higher than 22.5 V. If the extrapolation to higher deflections is correct, then the maximum deflection is:

$$d_{\max} = 0.01136 \frac{\text{nm}}{\text{V}^3} \cdot (0.75 \cdot 30 \text{ V})^3 + 4.32 \text{ nm} = (134 \pm 2) \text{ nm}. \quad (\text{H.8}) \quad \text{[eqn:dmax]}$$

1904 For a wavelength of 480 nm the maximum η we can achieve is 0.21. Therefor for
 1905 this wavelength and this particular generation-0 MMA, pistons instead of torsion
 1906 mirrors would achieve five times higher contrast (assuming the piston can only move
 1907 in one direction from the plane of equilibrium).

1908 Due to the bidirectional tilt of the mirrors along alternating rows (see Figure H.6)

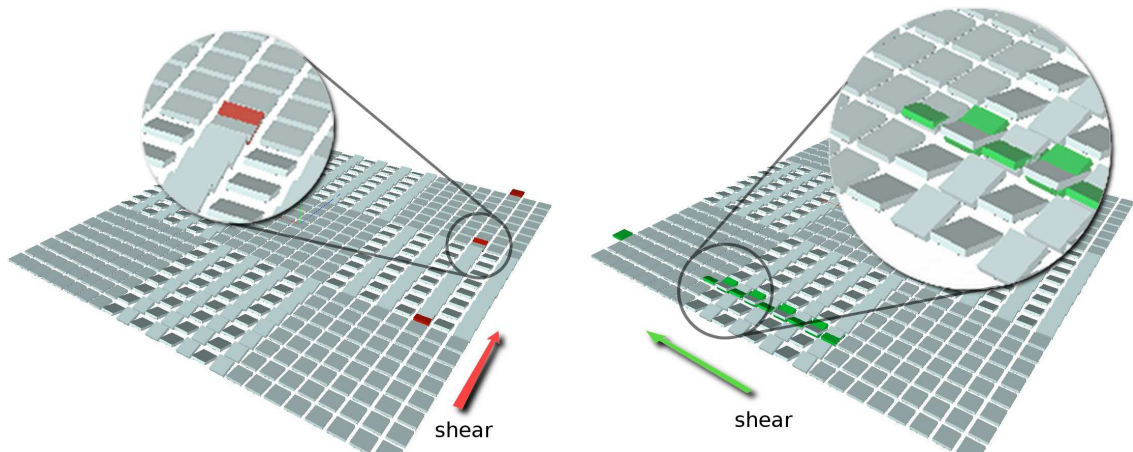


Figure H.6.: Diagrams showing how rows (Nomarski prism in -45° angle, left) or columns (Nomarski prism in $+45^\circ$, right) of the MMA are overlaid by the DIC prism. The coloured parts depict the neighbouring mirror as it is overlaid by the DIC. These images only show a 24×24 section of mirrors with a checkerboard of 16×16 periodicity.

`{fig:screen}`

1909 the MMA allows two different DIC modes. Either the mirrors are overlaid along
 1910 rows (all mirrors tilt into the same direction, see the left image in Figure H.6)
 1911 or mirrors are overlaid in column direction (neighbouring mirrors tilt to opposite
 1912 sides, see the right image in Figure H.6). The latter mode we cannot employ to
 1913 display arbitrary images. Two neighbouring flat mirrors will produce black and two
 1914 opposite-tilt mirrors will produce a maximum. There is no way how these mirror
 1915 tilts can be adjusted such, that arbitrary gray value images can be generated –
 1916 which is our goal.

1917 However, when the DIC shear direction is the same as the mirror tilt direction it
 1918 is indeed possible to display arbitrary gray value images.

1919 We generate a black image pixel by setting two immediate neighbours to the
 1920 same tilt angle. We create arbitrary gray values by tilting neighbouring mirrors in
 1921 slightly different directions. Equation (H.5) describes the relation between tilts of
 1922 the mirrors and the intensity of the image pixel. The brightest value $\eta = 0.214$ can
 1923 be achieved when one mirror is flat and the neighbour is tilted to the maximum
 1924 possible deflection d_{\max} (equation (H.8) shows its value for our generation-0 MMA).
 1925 However, it is not possible to exploit the full dynamic range of the device when
 1926 arbitrary images are to be displayed (at least not with the algorithm that we are
 1927 going to describe). Instead the maximum dynamic range is from $\eta = 0$ to $\eta = 0.064$.

1928 The algorithm that we use to calculate the mirror tilts – or rather the pixel values
 1929 q – that will result in a given intensity image after the DIC device. It uses our model

wrong

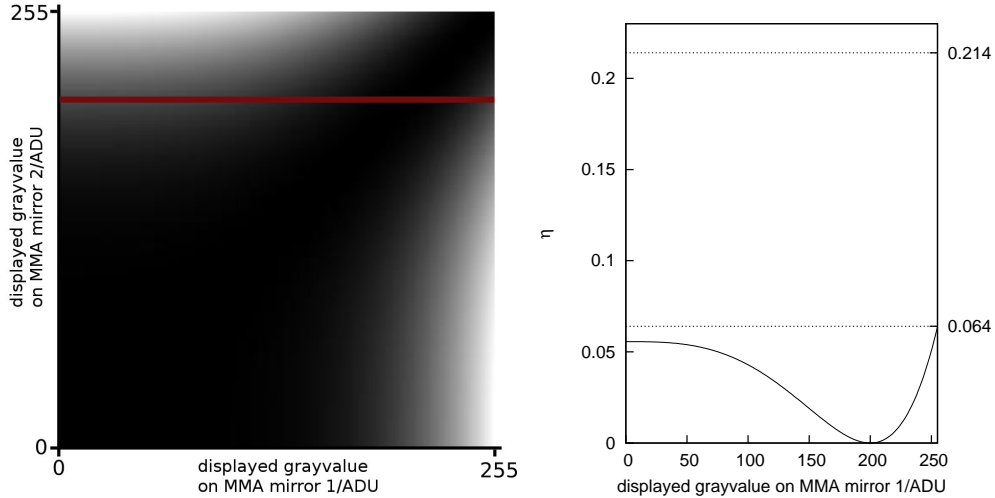


Figure H.7.: **left:** Theoretical η in dependence of the tilts of neighbouring mirrors. The analog-digital units (ADU) are proportional to the voltage U_{CE} . An ADU of 255 corresponds to a deflection of 134 nm. Black corresponds to $\eta = 0$ and white corresponds to $\eta = 0.21$. **right:** The graph shows the values along the red line in the matrix on the left, i.e. “mirror 2” is not tilted with gray value 200 corresponding to a tilt voltage $U_{CE} = 17.7\text{ V}$ that deflects the mirror to half of the maximum possible deflection. The maximum brightness $\eta = 0.064$ that can be obtained with this setting (when “mirror 1” is tilted to the maximum angle) is 30% of the brightness for maximum tilt difference between two mirrors.

`(fig:deflection2)`

1930 of the DIC device and the transfer function that maps voltages to mirror tilts.
 1931 Set a pixel on the border of the MMA to 0. We call this pixel “mirror 2”. Then
 1932 go one pixel in the direction of the DIC shift. We call this pixel “mirror 1”. Look
 1933 in the target image what intensity should be produced at this position. Search this
 1934 intensity in the look up table (Figure H.7) along the abscissa (for gray value 0 of
 1935 “mirror 2”) and set the gray value of “mirror 1” to the corresponding gray value.
 1936 Now rename “mirror 1” to “mirror 2” and go to the next pixel of the matrix. Repeat
 1937 this procedure for all pixels in this rows and do this algorithm for all columns of
 1938 the MMA.

1939 When the shear induced by the Nomarski prism doesn’t equal the mirror pitch of
 1940 $16\text{ }\mu\text{m}$, then the interference image of two mirrors will be deteriorated by line like
 1941 artifacts on the sides.

1942 H.4. Experimental results

1943 H.4.1. Procedure to measure the split angle of a Nomarski 1944 prism

1945 **<sec:prism>** The Nomarski prism consists of two quartz wedges. Its function is based on the
1946 birefringence of the crystal. The prism splits a 45° linearly polarized wavefront into two wavefronts with slightly diverging angles. The split is so small that its

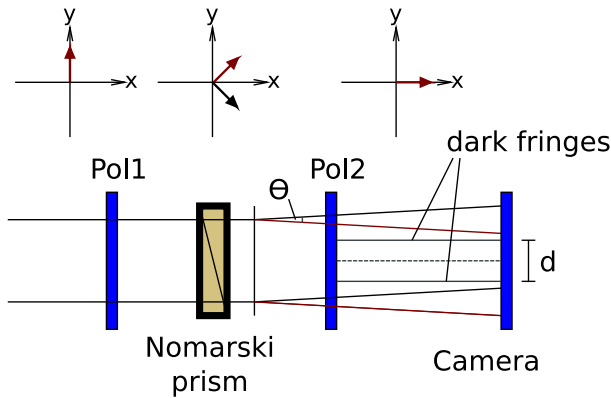


Figure H.8.: Setup to measure the split angle θ of a Nomarski prism by interference of the two beams. The polarizers Pol1 and Pol2 are crossed and in a 45° angle relative to the shift axis of the prism.

1947 **<fig:nomarski_split>**

1948 direct measurement — illuminating the prism with a parallel beam and putting the
1949 camera into the back focal plane of a lens with a long focal length — is difficult.
1950 Instead we put the prism between crossed polarizers, illuminate it with a parallel
1951 beam and measure a fringe pattern on the camera (see Figure H.8 for a schematic
1952 of the setup and Figure H.9 for the data).

The electrical field U after the second polarizer is:

$$U = e^{i\mathbf{k}_1 \cdot \mathbf{r}} + e^{i\mathbf{k}_2 \cdot \mathbf{r}}, \quad (\text{H.9}) \{ ? \}$$

$$|\mathbf{k}| = \frac{2\pi}{\lambda}, \quad (\text{H.10}) \{ ? \}$$

$$\mathbf{k}_1 = |\mathbf{k}|(0, \sin(\theta/2), \cos(\theta/2))^T, \quad (\text{H.11}) \{ ? \}$$

$$\mathbf{k}_2 = |\mathbf{k}|(0, -\sin(\theta/2), \cos(\theta/2))^T. \quad (\text{H.12}) \{ ? \}$$

The camera measures the intensity I :

$$I = |U|^2 = 4 \cos^2(|\mathbf{k}|y \sin(\theta/2)). \quad (\text{H.13}) \{ ? \}$$

Therefore the dark bands have a distance d (for small split angles θ):

$$d = \frac{\lambda}{2 \sin \theta/2} \approx \frac{\lambda}{\theta}. \quad (\text{H.14}) \{?\}$$

Our prism has a split angle $\theta = 0.078$ mrad. For a lens with a focal distance

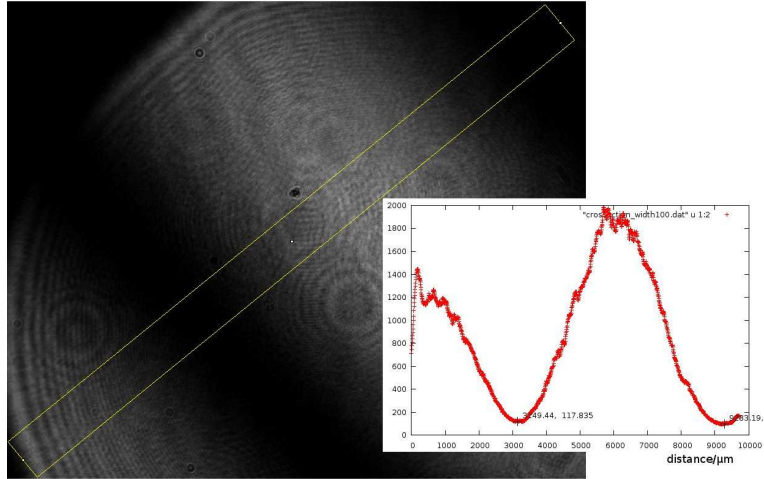


Figure H.9.: Camera image for the prism with the biggest split. The distance between the two dark fringes is $d = (6.06 \pm 0.08)$ mm. The light source is a laser with 473 nm wavelength. The values were integrated over the width of the yellow bar to reduce the influence of the disturbing fringes on the cross section.

`ig:nomarski_split_exp`

$f = 200$ mm this corresponds to a Nomarski split Δx :

$$\Delta x = 2f \tan(\theta/2) \approx f\theta = (15.6 \pm 0.2) \mu\text{m}. \quad (\text{H.15}) \{?\}$$

1953 This is close to the pixel pitch of 16 μm of the MMA.

1954 **H.4.2. Imaging the MMA with the DIC method**

1955 Figure H.10 shows see two typical images that can be achieved with the DIC setup.
1956 On these images the mirrors of the MMA tilt in -45° (to the bottom right) or in
1957 $+135^\circ$ (to the top left).

1958 The image that is displayed on the MMA for both pictures is a black and white
1959 checkerboard with a periodicity of 16×16 elements (as in Figure H.6). Fig-
1960 ure H.10 b) contains the case that is not usable for us. The DIC shift is along
1961 the $+45^\circ$ direction and brings mirrors that tilt in different directions to interfe-
1962 rence. The parts of the checkerboard pattern, where the mirrors are tilted appear
1963 bright in this image. The regions where the mirrors are flat are dark in the image.

1964 According to the right diagram in Figure H.6 the bright rectangles should have a
1965 darker border. Indeed this can be seen in the image on the camera (indicated by
1966 purple arrow in bottom right of Figure H.10).

1967 Figure H.10 a) shows the corresponding image with the prism turned by 90°
1968 relative to the right image. The displayed image on the MMA is the same black
1969 and white checkerboard. According to the left diagram in Figure H.6 one would
1970 expect white lines perpendicular to the shift direction. The image on the camera
1971 has these features and again one can make out the dark lines in the centres of the
1972 pixels.

1973 The contrast ratio for this experiment is only 0.6 and also the contrast in Fig-
1974 ure H.10 b) isn't much higher. This is probably because two identical DIC prisms
1975 were used in sequence to achieve twice the split (see Figure H.11). Without this
1976 disputable trick a 200 mm lens has to be used to get the necessary 16 μm DIC split
1977 but then the Fourier pattern is too big for the size of our DIC prisms. Figure H.12
1978 shows the gray value image that should be displayed on the camera. The image
1979 that has to be displayed on the MMA is shown in Figure H.13 b) and Figure H.13 c)
1980 shows the result on the camera (for the configuration with two DIC prisms).

1981 In section section H.4.3 some measurements for the setup with a 200 mm objective
1982 lens and only one prism are shown.

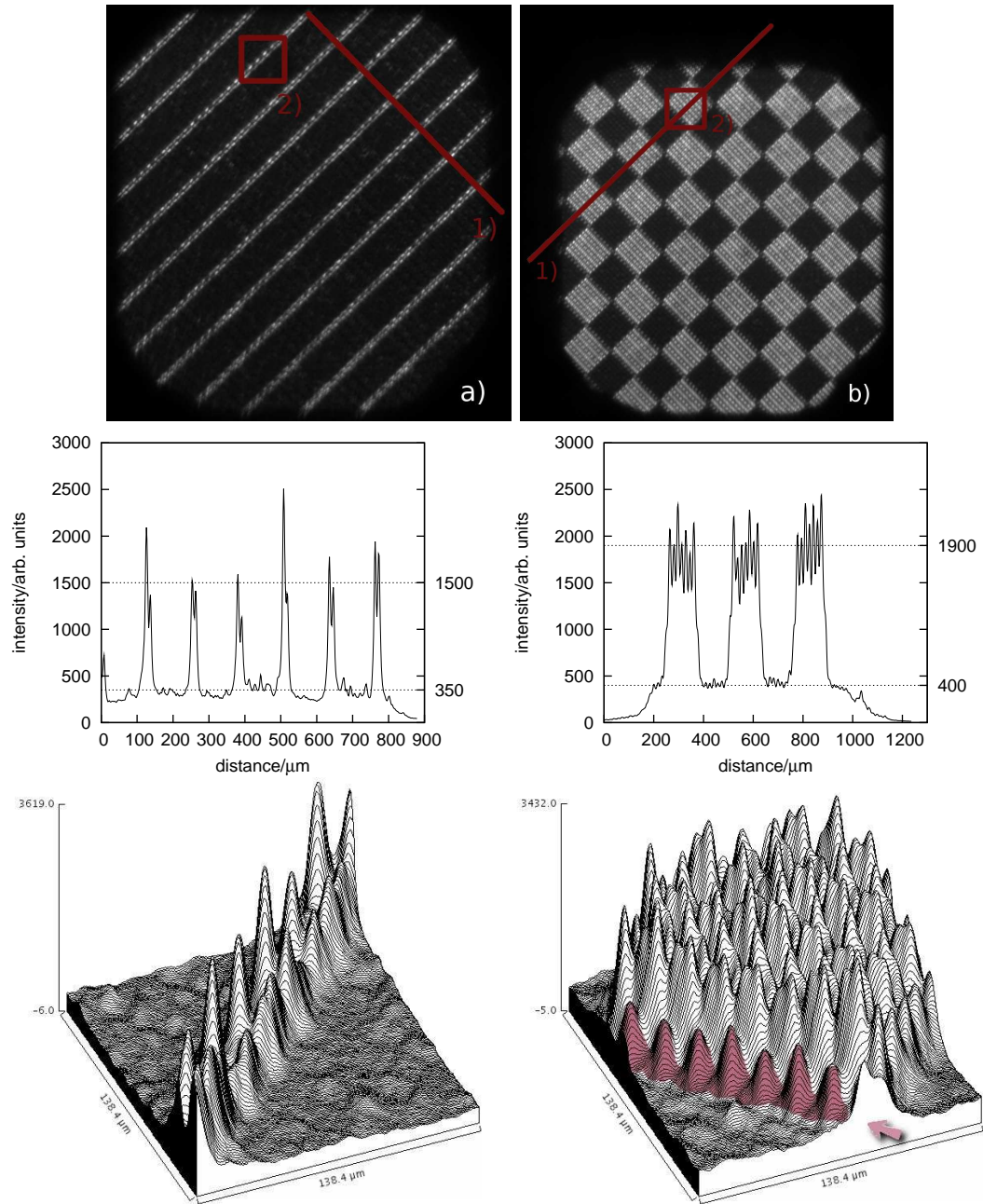


Figure H.10.: DIC image for a prism setting of -45° (a) and $+45^\circ$ (b). Below both images a cross section in the direction of the DIC shift is shown (along the line marked with 1)). The horizontal lines in those graphs show the values I_{\max} and I_{\min} for contrast estimation. The contrast ratios are 0.62 for (a) and 0.65 for (b). The rectangular region that is marked with 2) in the images is shown in the bottom diagrams. These images were taken with two identical sequential DIC prisms (for $63 \times /1.4$), a 100 mm objective lens and a 300 mm tube lens.

`(fig:screen5)`

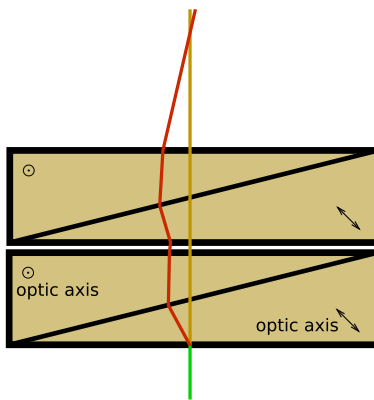


Figure H.11.: Combination of two identical DIC prisms to increase the split. The prism in the experiments are for a $63 \times /1.4$ oil immersion objective.

`<fig:double-prism>`

1983 **H.4.3. Effects of limited crystal size on DIC image**

1984 `<sec:size>` The split angle of the DIC prism defines the focal length of the objective lens that
 1985 needs to be used because the shift on the MMA must be $16 \mu\text{m}$. Our prism with
 1986 the biggest split needs a 200 mm lens. However the free aperture of the prism is
 1987 only 10 mm. Therefore it is problematic to capture three orders in the image on the
 1988 camera. These orders are needed to form an object-like image.

1989 For Figure H.14 one DIC prism was used with a 200 mm objective lens. It is not
 1990 possible to get the two outside orders with their complete surrounding information
 1991 through the prism. The relative size of the diffraction pattern on the DIC prism
 1992 aperture is shown on top of the images in Figure H.14. Note that the angular extend
 1993 of the illumination is indicated by the red spots in the Fourier pattern.

1994 The main advantage of the DIC method – and here we didn't make use of this –
 1995 is that the angular extend of the illumination can be significantly increased. Then
 1996 the red spots grow and may overlap. However all of them should still pass through
 1997 the DIC prism.

1998 In this experiment most of the orders were cut off. This leads to some artifacts
 1999 that are more pronounced when the aperture of the prism is artificially shrunken
 2000 (with a circular aperture).

2001 The experiment showed that the artifacts originate from line-like image patterns
 2002 that accidentally develop during our look-up table algorithm. See Figure H.15) for
 2003 a closeup of one such region. For this particular image it was possible to reduce the
 2004 number of line-like patterns on the face by starting the look up table algorithm on
 2005 a central column and then computing to the left and the right.

2006 However even with this trick there are still some phase jumps after strong gray
 2007 value discontinuities in the input image (see the red arrows in Figure H.15). The

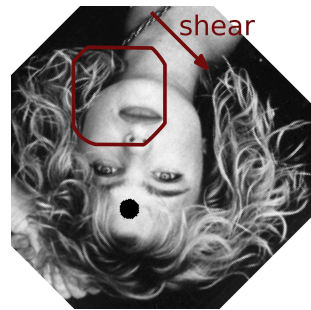


Figure H.12.: The input image that should be displayed on the camera. The rectangular region is illuminated by the integrating rod and imaged on the CCD.

`<fig:erika-overview>`

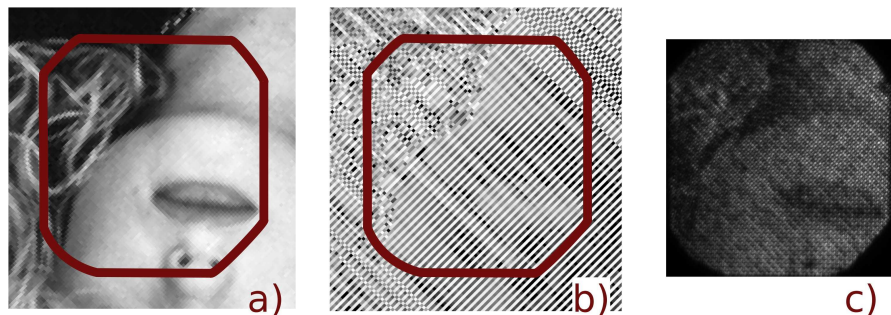


Figure H.13.: (a) Closeup of the input image. (b) The precomputed (with the look up table algorithm) image that is displayed on the MMA. The DIC shift will occur from the left top towards the right bottom. Note that regions that are white in the input image have a grating structure with high contrast. (c) The resulting image on the camera.

`<fig:erika-detail>`

2008 only real solution is to make the Nomarski prism bigger or use piston mirrors.

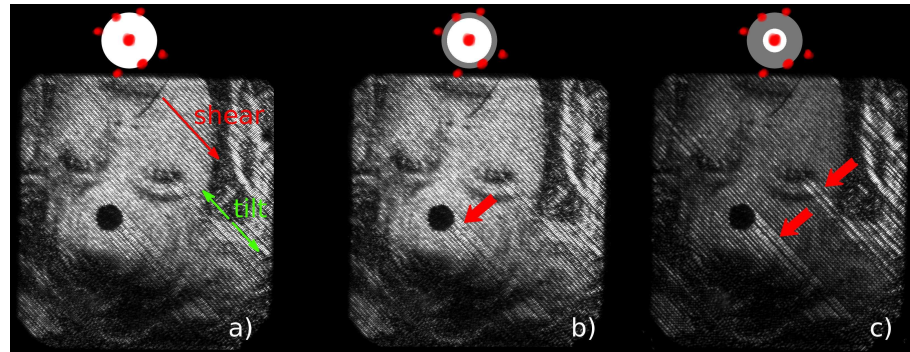


Figure H.14.: These three images show artifacts in gray level images that arise when less than three orders contribute to the image. The diagram in the top shows the aperture diameter in relation to the Fourier pattern of the MMA device. Phase changes in the displayed MMA image (see Figure H.15) result in banding artifacts (see red arrows) for decreasing aperture diameter. These images were taken with one DIC prism (for $63\times$, 1.4 micro objective) a 200 mm objective lens and a 500 mm tube lens.

`{fig:erikas}`

2009 H.5. Discussion

2010 The theoretical considerations lead to the conclusion that a piston device possesses
 2011 two significant advantages compared to the torsion mirrors. The DIC prism has to
 2012 be big enough so that at least three orders of the diffraction pattern of the torsion
 2013 mirrors can form an image. Torsion mirrors always have a black line in the centre of
 2014 the pixel because here neighbouring mirrors have the same height. A piston device
 2015 therefore will achieve higher contrast at equivalent deflection height and will need
 2016 a smaller prism diameter.

2017 For optimal performance it is crucial to have the MMA exactly in focus. Currently
 2018 it is very hard to focus the MMA as it is fixed to a large printed circuit board with
 2019 a heavy cable. After each focus change the angle of the board generally has to be
 2020 readjusted so that the zero order returns back through the Nomarski prism. With
 2021 the generation-2 MMA this problem has been solved as the device is connected to
 2022 the circuit board by a flexible cable.

2023 As an interesting application of the DIC method (other than improving the con-
 2024 trast) it might be possible to determine characteristic deflection curves for all mirrors
 2025 of a device individually. One approach would be to set all the mirrors parallel to the
 2026 device surface with a $+45^\circ$ DIC setting and then check for blackness with a -45°

H. Shearing interferometer-based intensity modulation with a MEMS mirror device

2027 setting and different voltages applied to neighbouring mirrors. With a device that is
2028 calibrated in such a way even better contrast will be possible, as mirror tilts can be
2029 adjusted to be exactly equal (with an uncalibrated device there is some spread due
2030 to manufacturing differences). At the time of the experiments no programmable
2031 update of images was possible. Therefor no such iterative calibration algorithm has
2032 been implemented.

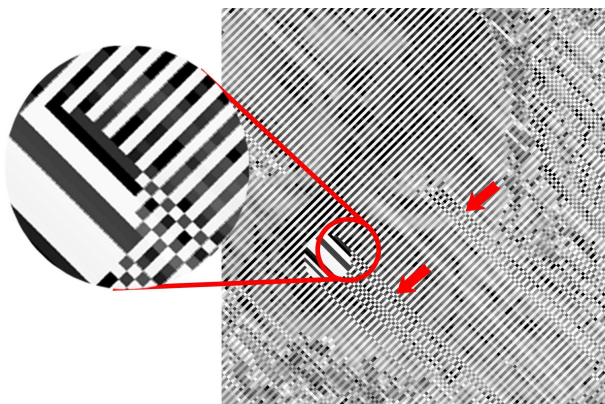


Figure H.15.: This image is displayed on the MMA in order to create a gray value DIC image. The shear direction is from top left to bottom right. When neighbouring image values are black and white the resulting pixel on the camera will be bright. If the image values don't change (look e.g. at the inside of the black circle) the pixel will be dark on the camera. When a dark gray value is to be generated there are many gray value pairs that result in the same intensity after the DIC device. However, if not all Fourier orders contribute to the camera image this is not true. Especially phase steps (see red arrows) produce banding artifacts. Note that this image generates a gray value image without artifacts when the two DIC prisms with a 100 mm lens are used.

erika-streak-overview>

I. Holographic approach to spatio-angular illumination

Here we present an alternative system for spatio-angular control. It is based on a single phase-only LCoS.

I.1. Introduction

In this part we describe a very different approach that simplifies the setup considerably.

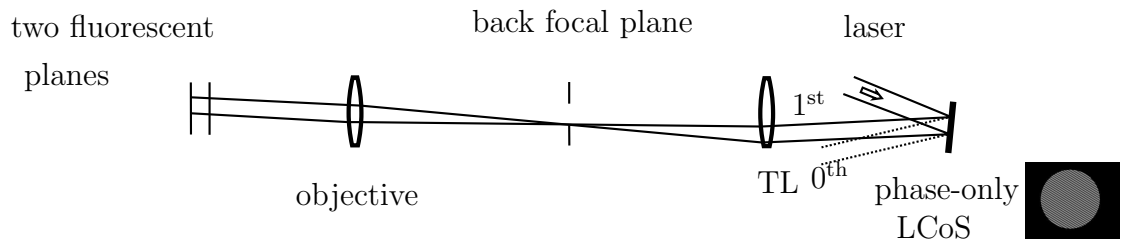


Figure I.1.: Schematic of the holographic spatio-angular microscope. A phase only LCoS in the intermediate image plane displays a grating and steers the first order into the back focal plane of the objective. Period and orientation define the angle of the illumination in the sample. Shape and contrast of the grating define the illuminated area and intensity of the illumination.

(fig:holo-setup3)

Figure I.1 shows a schematic of the setup. The main component is a phase-only spatial light modulator in the intermediate image plane. When nothing is displayed on the spatial light modulator, it will reflect the Gaussian laser beam into a beam dump.

I.2. Description of the holographic method

The spatial light modulator is then programmed to display a phase grating. The direction and periodicity of a grating can be chosen such, that the first order is

I. Holographic approach to spatio-angular illumination

2047 steered into any position on the back focal plane. In the sketch the grating directs
2048 the first order into the periphery of the back focal plane. Accordingly the region that
2049 contains the (demagnified) grating will be illuminated with an off-axis parallel beam
2050 of light. Decreasing the size of the grating will decrease the size of the illuminated
2051 area in the object. Note that a grating of very small size will make a broad order
2052 in the back focal plane, limiting the possible angular control.

2053 I.2.1. Description of the experimental setup

2054 We use a HEO 1080 P High-Resolution LCOS Phase Only Spatial Light Modulator
2055 (Holoeye, Berlin, Germany) to control the phase in the intermediate plane. The light
2056 source is a 473 nm DPSS diode laser. It is coupled into a polarization maintaining
2057 fibre and collimated by a 150 mm lens with 50 mm diameter.

2058 The tube lens has 300 mm diameter and the objective is a $63 \times /1.4$ with oil
2059 immersion. For aligning the optical system a sequence of device filling gratings was
2060 displayed at 60Hz. The parameters of the grating were chosen so that the point
2061 describes a circle in the back focal plane. It was then possible to align the LCOS
2062 angle so that the parallel beams leave the objective at the same angle relative to
2063 the optical axis.

2064 As the phase-only SLM never displays perfect blazed gratings, we prevent higher
2065 orders than the 1st from entering the back focal plane.

2066 I.2.2. Description of the sample

2067 To show that the illumination angle of the light was indeed adjustable a test sample
2068 was constructed. A slide and a cover slip were coated with a thin fluorescent plane.
2069 The air gap between was approximately five micrometres.

2070 Imaging the fluorophore plane on the slide resulted in a haze of background fluo-
2071 rescence stemming from the cover slip (see Figure I.2). Changing the illumination
2072 angle resulted in a rotation of this haze as one would expect.

2073 I.3. Characterization of the phase-only spatial light 2074 modulator

2075 Here We measure the correspondence between gray values and phase differ-
2076 ence on the Holoeye HEO 1080P spatial light modulator.

I. Holographic approach to spatio-angular illumination

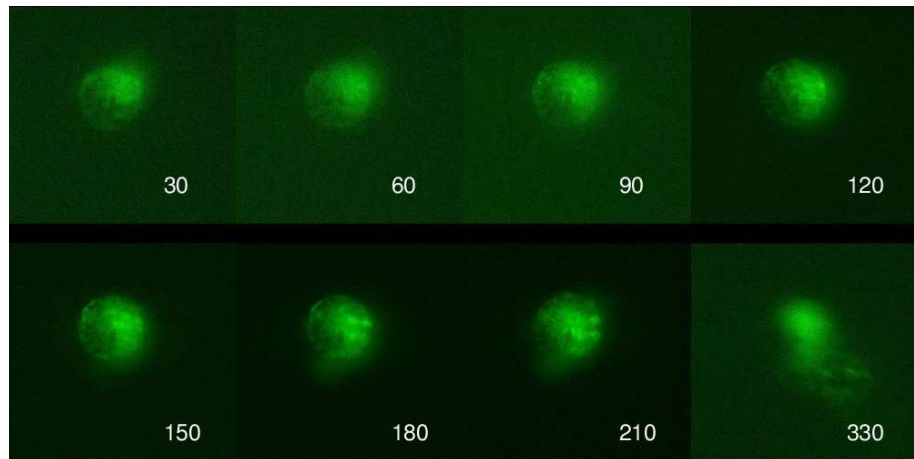


Figure I.2.: The numbers in the following image give the azimuth of the illumination angle in degree.

`(fig:holo-meas)`

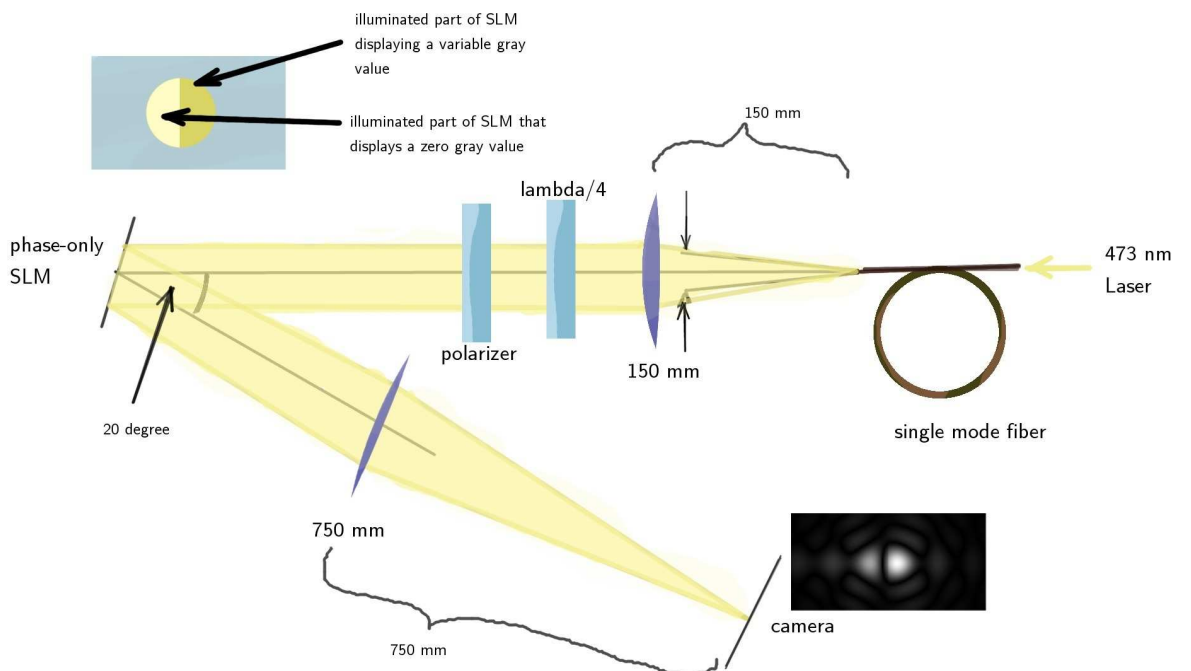


Figure I.3.: Setup for calibrating the transfer function of the phase SLM. We will establish, which gray values correspond to what phase delay. The light from a polarization maintaining single mode fibre is circularly polarized and a polarizer is then used to select the optimum polarization direction. The Fraunhofer diffraction pattern of light, which has been reflected from the device, is captured with a fast camera. The display's cable would come out at the top, perpendicular to the paper plane.

?`(fig:holo-calib)`?

2077 We use approximately the same setup as given in the Manual (Holoeye 2006). The
2078 SLM is illuminated with a parallel linearly polarized wave front. The plane of

2079 vibration of the electric field is in the paper plane.

2080 The SLM displays two vertical bars. The left bar shows black (0) and the upper
 2081 bar displays a gray value that is varied for the measurement. The beam has a circular
 2082 shape and a (sufficiently) constant intensity distribution. The beam is centred on
 2083 the line between the two bars of different phase. In contrast to the measurement
 2084 setup in the manual we did not place an analyzer between display and camera.

2085 **I.3.1. Numerical simulation**

2086 The minima of the diffraction pattern in the Fourier plane (on the camera) move
 2087 proportional to the phase difference between the two parts of the display (see Figure I.4). For the simulation we calculated the Fourier transform of a phase image

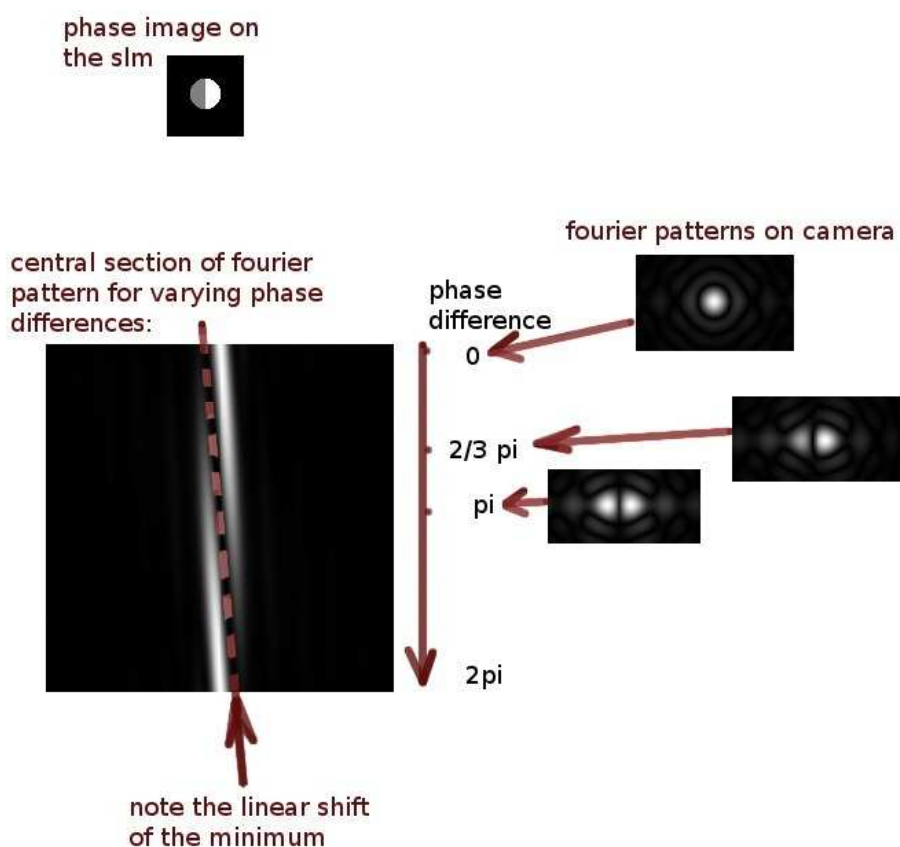


Figure I.4.: Theoretical simulation of the Fraunhofer diffraction pattern for varying phase difference between the two sides of the display.

(fig:holo-theory)
2088

2089 with a geometry as shown in the top left image in Figure I.4. The three images
 2090 on the right show the Fraunhofer diffraction patterns of this (reflective) phase im-
 2091 age for three different values of the phase difference between the half circles. The
 2092 position of the minimum changes proportionally to the phase difference. Therefor

I. Holographic approach to spatio-angular illumination

2093 we can measure the position of the extrema to determine the relationship between
2094 gray value and phase difference (the device's transfer function).

2095 I.3.2. Measurement

2096 The result of this measurement is shown in the top of Figure I.5 (horizontal section
through centre of the Fourier pattern against gray value) The measurement shows

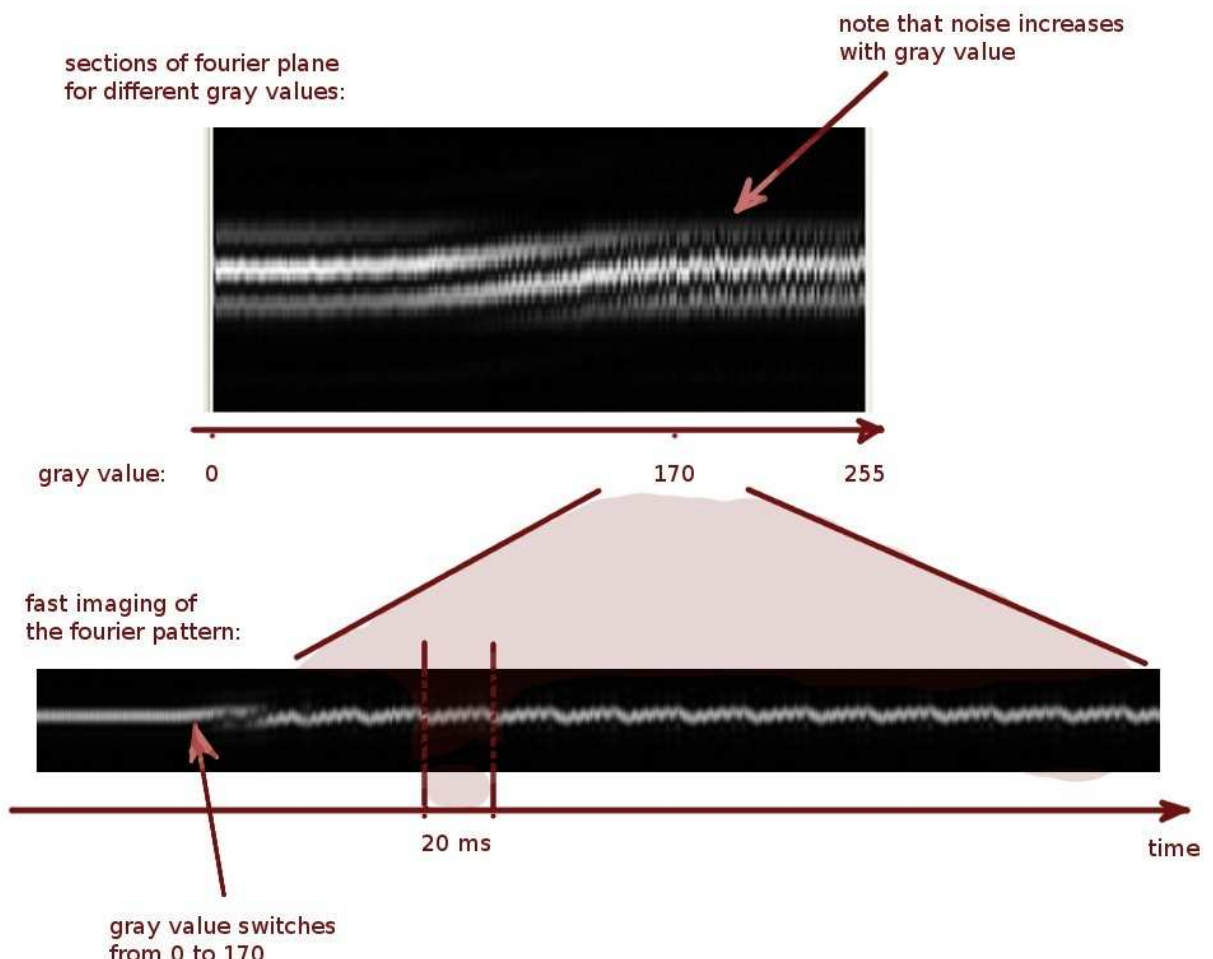


Figure I.5.: **top:** horizontal sections through the Fraunhofer diffraction pattern on the camera are plotted as columns. The displayed gray value is plotted as the x-axis. **bottom:** Time variation of the phase, when a constant value of 170 is shown. The phase fluctuates considerably.

`(fig:holo-transfer)`

2097
2098 that a phase difference of 2π can be induced for a sufficiently high gray value.
2099 However we observe significant noise for the phase measurements. There are jumps
2100 in the data that amount to several 10 gray values. As it turns out this isn't noise
2101 but the phase difference is time dependent.

I. Holographic approach to spatio-angular illumination

2102 To analyze this effect further a fast camera (mvBlueFox 102G, 2400 Hz, 200×4
2103 region of interest, $6 \mu\text{m}$ pixel size) was used to image the Fourier pattern with a
2104 high time resolution. The bottom image in Figure I.5 displays 1000 horizontal line
2105 sections over the centre of the Fourier plane. In the beginning both half circles
2106 were displaying a gray value of zero. Then the right half circle was suddenly set to
2107 170. The transient occurs quite fast but then there is a waveform with 5 peaks that
2108 repeats with 50 Hz (the refresh rate of the display).

2109 The measurement suggests that the phase difference of the Holoeye SLM is vary-
2110 ing significantly over time. In order to improve the performance for displaying
2111 computer generated holograms we could trigger the laser only for a short time be-
2112 fore a new frame will be displayed.

2113 From other experiments we know that there is also cross talk between the pixels,
2114 i.e. if a fine grating is displayed, the displayed phase contrast is lower than for a
2115 coarser grating.

I.4. Conclusion

2117 With our prototype system we showed that it is possible to use the phase-only
2118 SLM to do angular and spatial control of the illumination. Further work would
2119 be necessary to optimize the grating fine structure so that more light is directed
2120 towards the first order (blazing).

2121 Compared to the MEMI system a lot less synchronization between devices needs
2122 to be done. Note however, that this technique is only possible with coherent illumi-
2123 nation. Furthermore there is no inherent advantage in the holographic method as
2124 light from dark areas is sent into a beam stop and is lost as in the MEMI system.

2125 It might be possible to build a system using a kinoform element (two phase
2126 holograms in different positions). This would allow to redirect light from dark areas
2127 into bright areas leading to a much more efficient system. But a different display
2128 device with less cross talk and fluctuations would be advisable for this.

J. Equidistant spiral sampling

2129 In our system the MMA is imaged into the circular back focal plane of the
2130 microscope objective. Here we propose a method of storing images of circular
2131 apertures in its linear frame buffer.
2132

J.1. Archimedes Spiral

2133 An Archimedes spiral in polar coordinates (r, θ) is defined like this:

$$r(\theta) = a\theta. \quad (\text{J.1}) \boxed{\text{eqn: def}}$$

The step height h of the spiral is constant and given by

$$h = |r(\theta) - r(\theta + 2\pi)| = r(2\pi) = 2\pi a. \quad (\text{J.2}) \{?\}$$

2134 We would like to distribute circular windows at equidistant points along the spiral
2135 (Ahn et al. 1986).

J.2. Equidistance sampling

2136 We want to start sampling in the centre at $r(0) = 0$ and sample the arc length
of the spiral with equidistant points. The arc length of an Archimedes spiral is
(Weisstein):

$$s(\theta) = \frac{a}{2} (p\theta + \log(p\theta)) \quad \text{with} \quad p = \sqrt{1 + \theta^2}. \quad (\text{J.3}) \boxed{\text{eqn:arclen}}$$

The arc length Δs between successive points along the spiral should be equal to
the step height h . Starting from the central point $\theta_0 = 0$ the arc length where to
sample the i -th point can be obtained by inverting equation (J.3):

$$\theta_i = \theta(i \Delta s). \quad (\text{J.4}) \{?\}$$

J. Equidistant spiral sampling

This inversion can be done efficiently with Newton iteration:

$$x_0 = 1, \quad (\text{J.5}) \{ ? \}$$

$$x_{n+1} = x_n - \frac{f(x)}{f'(x)}. \quad (\text{J.6}) \{ ? \}$$

Here we introduce the function $f(\theta)$ that vanishes at a given arc length s and its derivative $f'(\theta)$:

$$f(\theta) = \frac{a}{2} (p\theta + \log(p\theta)) - s, \quad (\text{J.7}) \{ \text{eqn:f} \}$$

$$f'(\theta) = \frac{\partial f(\theta)}{\partial \theta} = \frac{a}{2} \frac{(1 + 2\theta^2)(1 + p\theta)}{p^2\theta}. \quad (\text{J.8}) \{ ? \}$$

J.3. Filling the back focal plane

We want to find the coordinates of equally distributed sampling points along the arc length inside of a circle with radius R . We put the first sampling point $\theta_0 = 0$ in the centre and the last point θ_n on the periphery of the circle. By definition (J.1) of the spiral we know

$$\theta_n = R/a. \quad (\text{J.9}) \{ ? \}$$

2137 Now we obtain the arc length $s(\theta_n)$ of the spiral contained inside the circle via (J.3). Dividing by the number of sub-intervals gives the appropriate sampling step 2139 $\Delta s = s(\theta_n)/(n - 1)$.

Note that we are only interested in solutions with $\Delta s = h$. We want the sampling step to be equal to the step height $h = 2\pi a$ of the spiral. We therefore need to find the zero of the function:

$$g(a) = \frac{s(\theta_n)}{n - 1} - 2\pi a \quad (\text{J.10}) \{ \text{eqn:g} \}$$

$$= \frac{a}{2} \frac{p\theta_n + \log p\theta_n}{n - 1} - 2\pi a \quad (\text{J.11}) \{ ? \}$$

$$= \frac{a}{2} \frac{\sqrt{1 + \frac{R^2}{a^2}} \frac{R}{a} + \log \left(\sqrt{1 + \frac{R^2}{a^2}} \frac{R}{a} \right)}{n - 1} - 2\pi a. \quad (\text{J.12}) \{ ? \}$$

J. Equidistant spiral sampling

We know $a \neq 0$ therefor we can transform the function to simplify its derivative:

$$g_1(a) = \underbrace{\sqrt{1 + \frac{R^2}{a^2}}}_{p_1} \frac{R}{a} + \log \left(\sqrt{1 + \frac{R^2}{a^2}} \frac{R}{a} \right) - 4\pi(n-1), \quad (\text{J.13}) \boxed{\text{eqn:g1}}$$

$$g'_1(a) = -\frac{R^3}{p_1} \frac{1}{a^4} - \frac{R^2}{p_1^2} \frac{1}{a^3} - Rp_1 \frac{1}{a^2} - \frac{1}{a}. \quad (\text{J.14}) \{?\}$$

- 2141 Newton's method can be used to find the zero a_0 of $g(a)$. Then Δs can be obtained
2142 and the circle drawn.

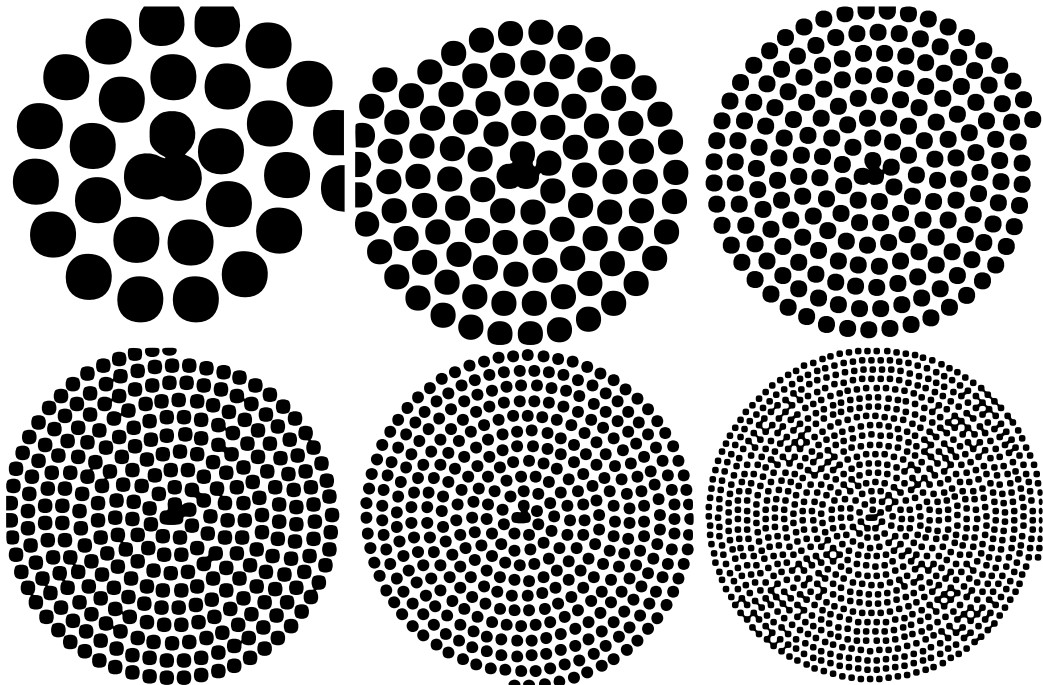


Figure J.1.: Equidistant sampling of a circle of the same radius $R = 128$ with different number of points (from top left to bottom right: 30, 100, 200, 300, 400, 1024).

2143 **J.4. Improvement for sampling with disks**

It is useful to modify the filling formula (J.10) such, that disks with radius $r_s = \alpha\Delta s/2$ on the sample points don't overlap the periphery of the big circle. Again we have $\theta_n = R/a$ but R is smaller than the back focal plane radius R_B :

$$R = R_B - r_s. \quad (\text{J.15}) \{?\}$$

Thus we can define the equivalent to (J.13):

$$g_2(a) = \overbrace{\sqrt{1 + \frac{(R_B - \pi\alpha a)^2}{a^2}} \frac{R_B - \pi\alpha a}{a} + \log \left(\sqrt{1 + \frac{(R_B - \pi\alpha a)^2}{a^2}} \frac{R_B - \pi\alpha a}{a} \right)}^{p_2} \\ - 4\pi(n - 1), \quad (\text{J.16}) \{?\}$$

$$g'_2(a) = -\frac{R^3}{p_2} \frac{1}{a^4} - \left(\frac{\pi\alpha R^2}{p_2} + \frac{R^2}{p_2^2} \right) \frac{1}{a^3} - \left(Rp_2 + \frac{\pi\alpha R}{p_2^2} \right) \frac{1}{a^2} - (\pi\alpha p_2 + 1) \frac{1}{a} + \frac{\pi\alpha}{R}. \quad (\text{J.17}) \{?\}$$

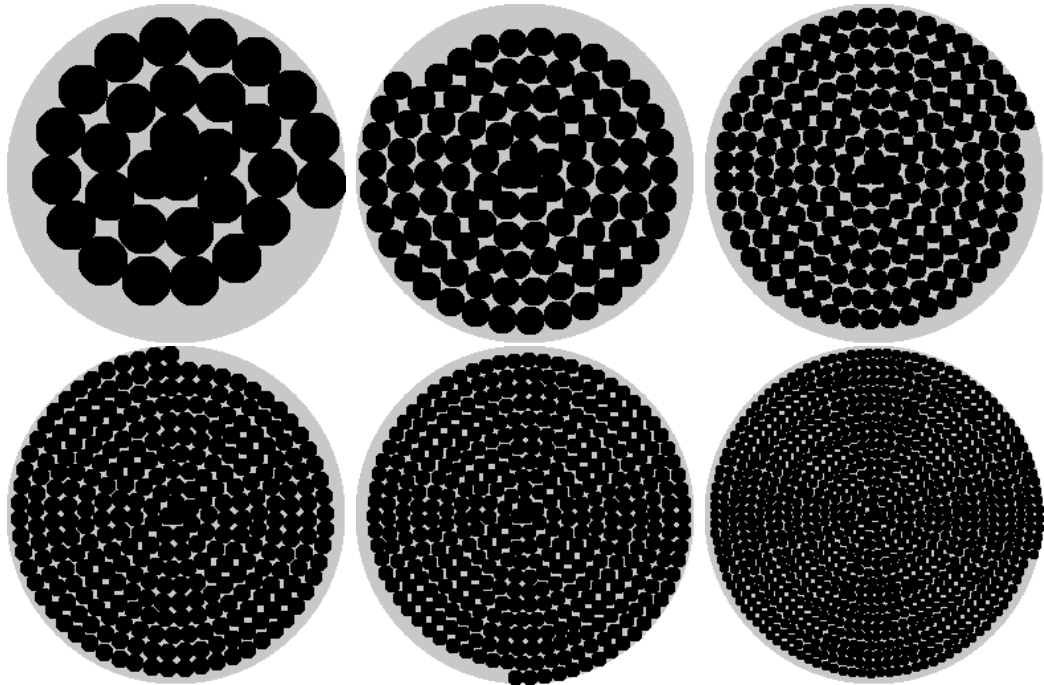


Figure J.2.: A back focal plane of radius 100 is filled with equidistant spiral sampling, ensuring that the outermost disk is contained inside. The number of disks are (from top left to bottom right): 30, 100, 200, 300, 400, 1024.

2144 J.5. Discussion

2145 It is possible to distribute sample points along a spiral over the back focal plane.
2146 However, there doesn't seem to be any advantage to placing the circles nodes of a
2147 polar grid. Indeed the spiral sampling is actually worse because for high angles the
2148 circles are either cut off or quite a large part of the BFP is not covered.

J. Equidistant spiral sampling

2149 We believe hexagonal sampling (Middleton and Sivaswamy 2001) will be a better
2150 alternative. It provides easy access to nearest neighbours and a natural hierarchy.

Bibliography

- Ahn1986**²¹⁵¹[1] C. B. Ahn, J. H. Kim, and Z. H. Cho. High-Speed Spiral-Scan Echo Planar NMR Imaging-I. *IEEE transactions on medical imaging*, 5(1):2–7, 1986. doi: 10.1109/TMI.1986.4307732.
- Amos1987**²¹⁵²[2] W B Amos, J G White, and M Fordham. Use of confo-cal imaging in the study of biological structures. *Applied Optics*, 26:3239–3243, 1987. doi: doi:10.1364/AO.26.003239. URL <http://www.opticsinfobase.org/abstract.cfm?URI=ao-26-16-3239>.
- Berndt2153**²¹⁵³[3] Dirk Berndt, Jörg Heber, Steffen Sinning, Dirk Rudloff, Steffen Wolschke, Mark Eckert, Jan-uwe Schmidt, Martin Bring, Michael Wagner, and Hubert Lakner. Calibration of diffractive micromirror arrays for microscopy applications.
- Botcherby2008**²¹⁵⁴[4] E J Botcherby, Rimvydas Juškaitis, M J Booth, and Tony Wilson. An optical technique for remote focusing in microscopy. *Opt. Commun.*, 281, 2008.
- Bozinovic2008**²¹⁵⁵[5] Nenad Bozinovic, Cathie Ventalon, Tim Ford, and Jerome Mertz. Fluorescence endomicroscopy with structured illumination. *Optics Express*, 16, 2008.
- Caarls2011**²¹⁵⁶[6] W Caarls, B Rieger, a H B De Vries, D J Arndt-Jovin, and T M Jovin. Minimizing light exposure with the programmable array microscope. *Journal of microscopy*, 241(1):101–10, January 2011. ISSN 1365-2818. doi: 10.1111/j.1365-2818.2010.03413.x. URL <http://www.ncbi.nlm.nih.gov/pubmed/21118211>.
- Chu2007**²¹⁵⁷[7] Kengyeh K Chu, Daryl Lim, and Jerome Mertz. Enhanced weak-signal sensitivity in two-photon microscopy by adaptive illumination. *Opt. Lett.*, 32(19):2846–2848, October 2007. doi: 10.1364/OL.32.002846. URL <http://ol.osa.org/abstract.cfm?URI=ol-32-19-2846>.
- Denk1990**²¹⁵⁸[8] W Denk, J H Strickler, and W W Webb. Two-photon laser scanning fluorescence microscopy. *Science*, 245, 1990.
- Dunsby2008**²¹⁵⁹[9] Christopher Dunsby. Optically sectioned imaging by oblique plane microscopy. *Optics Express*, 16, 2008.

Bibliography

- [Fischer1996] [210] M Fischer and J Georges. Fluorescence quantum yield of rhodamine 6G in ethanol
2179 as a function of concentration using thermal lens spectrometry. *Chem. Phys.*
2180 *Lett.*, 260, 1996. doi: 10.1016/0009-2614(96)00838-X.
- [Goodman1996] [211] Joseph W Goodman. *Introduction to Fourier Optics*. McGraw-Hill, second edition,
2182 1996.
- [grossman2010] [212] Nir Grossman, Vincent Poher, Matthew S Grubb, Gordon T Kennedy, Kon-
2184 stantin Nikolic, Brian McGovern, Rolando Berlinguer Palmini, Zheng Gong,
2185 Emmanuel M Drakakis, Mark A A Neil, Martin D Dawson, Juan Bur-
2186 rrone, and Patrick Degenaar. Multi-site optical excitation using ChR2 and
2187 micro-LED array. *Journal of Neural Engineering*, 7(1):16004, 2010. URL
2188 <http://stacks.iop.org/1741-2552/7/i=1/a=016004>.
- [Haken2006] [213] Hermann Haken and Hans Christoph Wolf. *Molekülphysik und Quantenchemie*.
2190 Springer, fifth edition, 2006. doi: 10.1007/3-540-30315-4.
- [Hamai1983] [214] Sanyo Hamai and Fumio Hirayama. Actinometric determination of absolute fluores-
2192 cence quantum yields. *J. Phys. Chem.*, 87:83–89, 1983. doi: 10.1021/j100224a020.
- [Hoebe2007] [215] R A Hoebe, C H Van Oven, T W J Gadella Jr., P B Dholukshe, C J F Van
2194 Noorden, and E M M Manders. Controlled light-exposure microscopy reduces
2195 photobleaching and phototoxicity in fluorescence live-cell imaging. *NATURE*
2196 *BIOTECHNOLOGY*, 25(2):249–253, February 2007. ISSN 1087-0156. doi: 10.
2197 1038/nbt1278.
- [Hoebe2010] [216] R A Hoebe, C J F Van Noorden, and E M M Manders. Noise effects and fil-
2199 tering in controlled light exposure microscopy. *Journal of Microscopy*, 240(3):
2200 197–206, 2010. ISSN 1365-2818. doi: 10.1111/j.1365-2818.2010.03400.x. URL
2201 <http://dx.doi.org/10.1111/j.1365-2818.2010.03400.x>.
- [Holoeye2006] [217] Holoeye. Application Note HDTV Phase Panel Developer Kit. Technical report,
2203 2006.
- [Huiskens2004] [218] Jan Huisken, Jim Swoger, Filippo Del Bene, Joachim Wittbrodt, and Ernst
2205 H K Stelzer. Optical Sectioning Deep Inside Live Embryos by Selec-
2206 tive Plane Illumination Microscopy. *Science*, 305(5686):1007–1009, Au-
2207 gust 2004. ISSN 0036-8075. doi: 10.1126/science.1100035. URL
2208 <http://www.lmg.embl.de/pdf/huisken04.pdf>.

Bibliography

- [Hwang2008] [20] Sun-uk Hwang and Yong-gu Lee. Simulation of an oil immersion objective lens : A simplified ray-optics model considering Abbe's sine condition. *Optics Express*, 16(26):363–370, 2008.
- [Konopka2008] [20] Catherine A Konopka and Sebastian Y Bednarek. Variable-angle epifluorescence microscopy: a new way to look at protein dynamics in the plant cell cortex. *The Plant Journal*, 53:186–196, 2008. URL <http://www.biochem.wisc.edu/faculty/bednarek/lab/publications/Konopka2007Plant.pdf>.
- [Levoy2009] [21] M Levoy, Z Zhang, and I McDowall. Recording and controlling the 4D light field in a microscope using microlens arrays. *Journal of Microscopy*, 235(2):144–162, 2009. ISSN 1365-2818. doi: 10.1111/j.1365-2818.2009.03195.x. URL <http://dx.doi.org/10.1111/j.1365-2818.2009.03195.x>.
- [Levoy2006] [22] Marc Levoy, Ren Ng, Andrew Adams, Matthew Footer, and Mark Horowitz. Light field microscopy. *ACM Trans. Graph.*, 25(3):924–934, July 2006. ISSN 0730-0301. doi: <http://doi.acm.org/10.1145/1141911.1141976>. URL <http://doi.acm.org/10.1145/1141911.1141976>.
- [2008Lim] [23] D Lim, K K Chu, and J Mertz. Wide-field fluorescence sectioning with hybrid speckle and uniform-illumination microscopy. *Optics Letters*, 33(16):1819–1821, 2008.
- [Lippmann1908] [24] Gabriel Lippmann. Epreuves reversibles. Photographies intégrals. *Comptes-Rendus Academie des Sciences*, 146:446–451, 1908. URL <http://ci.nii.ac.jp/naid/10019520779/en/>.
- [Lutz2008] [25] C Lutz, T S Otis, V DeSars, S Charpak, D A DiGregorio, and V Emiliani. {H}olographic photolysis of caged neurotransmitters. *Nat. Methods*, 5:821–827, September 2008. URL <http://www.ncbi.nlm.nih.gov/pmc/articles/PMC2711023/>.
- [Mackay] [26] Craig D Mackay, Robert N Tubbs, Ray Bell, David Burt, and Ian Moody. Sub-Electron Read Noise at MHz Pixel Rates. *SPIE*, 2001.
- [McClain1993] [27] Stephen C McClain, Lloyd W Hillman, and Russell A Chipman. Polarization ray tracing in anisotropic optically active media. I. Algorithms. *J. Opt. Soc. Am. A*, 10, 1993.
- [Mertz2010] [28] Jerome Mertz and Jinhyun Kim. Scanning light-sheet microscopy in the whole mouse brain with HiLo background rejection. *Journal of biomedical*

Bibliography

- 2241 *optics*, 15(1):016027, 2010. ISSN 1560-2281. doi: 10.1117/1.3324890. URL
2242 [http://www.ncbi.nlm.nih.gov/pmcarticles/PMC2917465/](http://www.ncbi.nlm.nih.gov/pmc/articles/PMC2917465/)
- [Middleton2001] [29] Lee Middleton and Jayanthi Sivaswamy. Edge detection in a hexagonal-image processing framework. *Image and Vision computing*, 19(14):1071–1081, 2001. URL
2244 <http://www.sciencedirect.com/science/article/pii/S0262885601000671>.
- [Minsky1961] [30] Marvin Minsky. Microscopy Apparatus, December 1961. URL
2247 http://www.google.co.uk/patents/download/3013467_MICROSCOPY_APPARATUS.pdf?id=1
- [Minsky1988] [31] Marvin Minsky. Memoir on Inventing the Confocal Scanning Microscope. *Scanning*, 10:128–138, 1988. URL
2249 <http://web.media.mit.edu/~minsky/papers/ConfocalMemoir.html>.
- [Neil1997] [32] Mark A A Neil, Rimvydas Juškaitis, and Tony Wilson. Method of obtaining optical sectioning by using structured light in a conventional microscope. *Optics Letters*, 22:1905–1907, 1997.
- [Nikolenko2008] [33] V Nikolenko, B O Watson, R Araya, A Woodruff, D S Peterka, and R Yuste. SLM Microscopy: Scanless Two-Photon Imaging and Photostimulation with Spatial Light Modulators. *Front Neural Circuits*, 2:5, 2008. URL
2255 <http://www.ncbi.nlm.nih.gov/pmc/articles/PMC2614319/>.
- [Oron2005] [34] D Oron, E Tal, and Y Silberberg. {S}canningless depth-resolved microscopy. *Opt Express*, 13:1468–1476, March 2005. URL
2259 <http://www.weizmann.ac.il/home/feyaron/microscope/scanningless.pdf>.
- [Otsu2008] [35] Y Otsu, V Bormuth, J Wong, B Mathieu, G P Dugue, A Feltz, and S Dieudonne. {O}ptical monitoring of neuronal activity at high frame rate with a digital random-access multiphoton ({R}{A}{M}{P}) microscope. *J. Neurosci. Methods*, 173:259–270, August 2008. URL
2262 http://cnp.igc.gulbenkian.pt/_media/research/mainen/ghyomm/otsu_2008.pdf.
- [Papagiakoumou2010] [36] E Papagiakoumou, F Anselmi, A Begue, V de Sars, J Gluckstad, E Y Isacoff, and V Emiliani. {S}canless two-photon excitation of channelrhodopsin-2. *Nat. Methods*, 7:848–854, October 2010.
- [Press1997] [37] William H. Press, Saul A. Teukolsky, William T. Vetterling, and Brian P. Flannery. *Numerical Recipes in C*. Cambridge University Press, Cambridge, second edition, 1997. ISBN 0521431085.

Bibliography

- [Reddy2008] [38] Duemani G Reddy, K Kelleher, R Fink, and P Saggau. Three-dimensional random access multiphoton microscopy for functional imaging of neuronal activity. *Nat. Neurosci.*, 11:713–720, June 2008. URL <http://www.ncbi.nlm.nih.gov/pmc/articles/PMC2747788/pdf/nihms129126.pdf>.
- [Robbins2003] [39] Mark Stanford Robbins, Senior Member, and Benjamin James Hadwen. The Noise Performance of Electron Multiplying Charge-Coupled Devices. *IEEE Transactions on Electron Devices*, 50(5):1227–1232, 2003.
- [Rodrigo2008] [40] Peter John Rodrigo, Darwin Palima, and Jesper Glückstad. Ac-
2280 curate quantitative phase imaging using generalized phase
2281 contrast. *Optics Express*, 16:2740–2751, 2008. URL
2282 <http://www.opticsinfobase.org/abstract.cfm?URI=oe-16-4-2740>.
- [1991Saleh] [41] B E A Saleh and M C Teich. *Fundamentals of photonics*. Wiley, 1991.
- [Santella2010] [42] Anthony Santella, Zhuo Du, Sonja Nowotschin, Anna-Katerina A.K. Had-
2285 jantonakis, and Zhirong Bao. A hybrid blob-slice model for accurate and
2286 efficient detection of fluorescence labeled nuclei in 3D. *BMC bioinformat-
2287 ics*, 11(1):580, 2010. ISSN 1471-2105. doi: 10.1186/1471-2105-11-580. URL
2288 <http://www.biomedcentral.com/1471-2105/11/580/abstract>
- [Santi2011] [43] Peter A Santi. Light Sheet Fluorescence Microscopy. *Journal of Histochemistry & Cytochemistry*, 59:129–138, 2011. doi: doi:10.1369/0022155410394857.
- [2009Santos] [44] Silvia Santos, Kengyeh K Chu, Daryl Lim, Nenad Bozinovic, Tim N Ford, Claire
2292 Houroule, Aaron C Bartoo, Satish K Singh, and Jerome Mertz. Optically sec-
2293 tioned fluorescence endomicroscopy with hybrid-illumination imaging through a
2294 flexible fiber bundle. *J Biomed Opt*, 14(3):30502, 2009.
- [Schwertner2008] [45] M Schwertner, M Booth, and T Wilson. Wavefront sensing based on ro-
2296 tated lateral shearing interferometry. *Optics Communications*, 281(2):210–216,
2297 January 2008. ISSN 00304018. doi: 10.1016/j.optcom.2007.09.025. URL
2298 <http://linkinghub.elsevier.com/retrieve/pii/S0030401807008930>.
- [Siedentopf1903] [46] H Siedentopf and R Zsigmondy. Über die Lichtbarmachung und
2300 die Größebestimmung ultramikroskopischer Teilchen, mit beson-
2301 derer Anwendung auf Goldrubingläser. *Annalen der Physik*,
2302 315:1–39, 1903. doi: DOI:10.1002/andp.19023150102. URL
2303 <http://onlinelibrary.wiley.com/doi/10.1002/andp.19023150102/abstract>.

Bibliography

- [Smith2000] [47] WJ Smith. *Modern optical engineering.* McGraw-Hill, 3 edition, 2000. ISBN 0071363602. URL <http://scholar.google.com/scholar?hl=en&btnG=Search&q=intitle:Modern+Optical>
- [Tokunaga2008] [48] Makio Tokunaga, Naoko Imamoto, and Kumiko Sakata-Sogawa. Highly inclined thin illumination enables clear single-molecule imaging in cells. *Nature Methods*, 5(2):159–161, February 2008. ISSN 1548-7091. doi: 10.1038/NMETH.1171. URL <http://www.ncbi.nlm.nih.gov/pubmed/18176568> <http://www.riken.jp/ExtremePhoton>
- [Verveer1998] [49] P J Verveer, Q S Hanley, P W Verbeek, L J V A N Vliet, and T M Jovin. Theory of confocal fluorescence imaging in the programmable array microscope (PAM). 189(December 1997):192–198, 1998.
- [Vogelsang2008] [50] Jan Vogelsang, Robert Kasper, Christian Steinhauer, Britta Person, Mike Heilemann, Markus Sauer, and Philip Tinnefeld. A Reducing and Oxidizing System Minimizes Photobleaching and Blinking of Fluorescent Dyes. *Angew. Chem. Int. Ed.*, 47, 2008. doi: 10.1002/anie.200801518.
- [Voie1993] [51] A H Voie, D H Burns, and F A Spelman. Orthogonal-plane fluorescence optical sectioning: three-dimensional imaging of macroscopic biological specimens. *Journal of Microscopy*, 1993.
- [Weisstein] [52] Eric W. Weisstein. Archimedes' Spiral.
- [Zahid2010] [53] Morad Zahid, Mateo Vélez-Fort, Eirini Papagiakoumou, Cathie Ventalon, Maria Cecilia Angulo, and Valentina Emiliani. Holographic Photolysis for Multiple Cell Stimulation in Mouse Hippocampal Slices. *PLoS ONE*, 5(2):e9431, 2010. doi: 10.1371/journal.pone.0009431. URL <http://dx.doi.org/10.1371/journal.pone.0009431>.
- [Zhang2009] [54] Zhengyun Zhang and M Levoy. Wigner distributions and how they relate to the light field. In *Computational Photography (ICCP), 2009 IEEE International Conference on*, pages 1–10, April 2009. doi: 10.1109/ICCPHOT.2009.5559007.